TECHNISCHE UNIVERSITÄT WIEN
Vienna University of Technology

DIPLOMARBEIT

Investigation and feasibility study of $SrTiO_3$ thin films in high temperature solid oxide solar cells

zur Erlangung des akademischen Grades

Diplom-Ingenieur

im Rahmen des Studiums

Physikalische Energie- und Messtechnik

eingereicht von

Philip Klein

Matrikelnummer 01526384

ausgeführt am Institut für Chemische Technologien und Analytik
der Fakultät für Technische Chemie der Technischen Universität Wien

Betreuung:
Univ.Prof. Dipl.-Phys. Dr.rer.nat. Jürgen Fleig
Senior Scientist Dipl.-Ing. Dr.in techn. Stefanie Taibl

Wien, 17.02.2023

(Philip Klein) (Jürgen Fleig)

Abstract

Providing and storing clean energy is getting more and more important, fighting global problems like climate change or air pollution. One way to do so is combining a high temperature solid oxide solar cell with a solid oxide electrolyser cell gaining a photoelectrochemical cell, which can be used for small-scale energy harvesting applications. Such micro-harvestorers could for example replace batteries in unwired minimised wireless sensor nodes (WSN), needed for the Internet of Things (IoT), which has been identified as one of the most important technologies in the near future. As small batteries also have a limited lifetime, the replacement would have environmental and economic benefits. Knowing that $SrTiO_3$ (STO) as a single crystal has the potential of being used in high temperature solar cell applications when combining it, e.g., with a LSCr top electrode, the question arose, if also STO thin films can be used as such, making the final product even smaller and thus more economic to produce. Therefore, high temperature STO thin film based solid oxide solar cell samples were prepared and investigated to generally observe, whether STO thin films can work in such micro-solar cell applications and further to get a better understanding of electrical and defect chemical processes under operation. The preparation was done with pulsed laser deposition (PLD). The solar cell is ablated onto a 10 x 10 mm^2 $SrTiO_3$ single crystal in three steps, growing layers of (La,Sr)CoO_3 (LSC) (counter electrode), $SrTiO_3$ (absorber layer) and (La,Sr)CrO_3 (LSCr) (working electrode). To analyse the samples, different methods are applied, such as electrochemical impedance spectroscopy (EIS), voltage and current measurements under UV light, transmission electron microscopy (TEM) and mass spectrometry (Online-LASIL-ICP-MS, LA-ICP-MS). Varying certain parameters like the thickness, the geometry of the STO layer as well as the laser fluence revealed that STO thin film solar cell samples are feasible and that the best results can be achieved with a STO7% (7% Sr excess in the target) layer with a thickness of about 840 nm using a fluence of around 1 J/cm^2. Open circuit voltages up to 830 mV and short circuit currents up to 0,193 mA/cm^2 were reached under ambient air conditions and 300°C set temperature. Open circuit voltages up to 870 mV and short circuit currents up 0,25 mA/cm^2 are gained under synthetic air conditions at 300°C. It was found that the deposition of a dense and at the same time stoichiometric STO thin film seems to be the key for photovoltaically-active cells. However, the feasibility of reproducing the samples during preparation still poses problems. This could be due to various reasons, including the Sr excess in the STO target, the interaction between the target and the laser pulse or laser fluence variations over longer deposition times.

Kurzfassung

Die Bereitstellung und Speicherung erneuerbarer Energie wird zunehmend wichtiger um globale Probleme wie den Klimawandel zu bekämpfen. Eine Möglichkeit, dies zu erreichen, ist die Kombination einer Hochtemperatur-Festoxid-Solarzelle mit einer Festoxid-Elektrolysezelle, die in einer photoelektrochemischen Zelle resultiert. Solch eine photoelektrochemische Zelle kann beispielsweise für kleine Energiegewinnungsanwendungen (Mikro-Harvestorer) eingesetzt werden. Mikro-Harvestorer könnten etwa Batterien in drahtlosen Sensoren ersetzen, die für das Internet der Dinge (IdD) benötigt werden. Da die benötigten kleinen Batterien eine begrenzte Lebensdauer haben, würde der Ersatz ökologische und wirtschaftliche Vorteile mit sich bringen. Die Funktion von Hochtemperatur-Solarzellen wurde bereits unter der Verwendung von $SrTiO_3$ (STO) Einkristallen in Kombination mit einer LSCr-Top-Elektrode gezeigt. Aus diesem Ergebnis heraus entstand die Frage, ob auch Hochtemperatur-Solarzellen auf Basis von STO-Dünnschichten hergestellt werden können, wodurch das Endprodukt noch kleiner und somit wirtschaftlicher zu produzieren wäre. Angesichts dessen wurden auf STO-Dünnschichten Basierte Hochtemperatur-Solarzellen hergestellt und untersucht. Die Dünnschichten der Solarzelle wurden auf einen 10 x 10 mm^2 großen $SrTiO_3$-Einkristall in drei Schritten abgeschieden. Als Gegenelectrode wurde Sr-dotiertes $LaCoO_3$ verwendet, als Absorber STO und als Arbeitselectrode Sr-dotiertes $LaCrO_3$. Die Herstellung erfolgte mittels gepulster Laserdeposition (PLD). Zur Analyse der Proben wurden verschiedene Methoden wie elektrochemische Impedanzspektroskopie (EIS), Spannungs- und Strommessungen unter UV-Licht, Transmissionselektronenmikroskopie (TEM) und Massenspektrometrie (Online-LASIL-ICP-MS, LA-ICP-MS) eingesetzt.

Durch Variation bestimmter Parameter wie Dicke, Geometrie der STO-Dünnschicht oder Laserfluenz wurde gezeigt, dass funktionierende STO-Dünnschichtsolarzellen hergestellt werden können. Die besten Ergebnisse konnten mit einer 840 nm dicken STO7% (7% Sr-Überschuss im Target) Schicht und einer Fluenz von etwa 1 J/cm^2 erzielt werden. Bei Umgebungsluft und einer Temperatur von 300°C wurden Leerlaufspannungen von bis zu 830 mV und Kurzschlussströme von bis zu 0,193 mA/cm^2 erreicht. Unter Verwendung von synthetischer Luft wurden Leerlaufspannungen von bis zu 870 mV und Kurzschlussströme von bis zu 0,25 mA/cm^2 erreicht. Die Reproduzierbarkeit der Proben während der Präparation bereitet jedoch noch Probleme. Mögliche Ursachen sind der Sr Überschuss im STO-Target, die Wechselwirkung zwischen dem Target und dem Laserpuls oder Schwankungen der Laserfluenz über längere Depositionszeiten. Die Abscheidung von dichten und stöchiometrischen STO-Dünnschicht scheint von entscheidender Bedeutung zu sein um photovoltaische Aktivität zu erreichen.

Contents

1 Introduction

Providing and storing clean energy is getting more and more important, as the energy demand is expected to keep growing until 2050 and the global emissions coming from fossil fuels are still far too high. Solar energy, as one renewable example, has the potential of providing abundant clean energy throughout a wide range of regions. Solar energy has the theoretical potential to meet the energy needs of the entire world if the technologies to harvest and deliver the energy were readily available. About four million exajoules (10^{18}) of solar energy reach the earth annually, $5 \cdot 10^4$ EJ of which could be harvested easily. Despite this massive potential and the growing awareness, the contribution of solar energy to the global energy supply is still improvable. Today, renewables account for around 30% of the global energy demand. In order to combat global warming, it is expected that renewable energy will cover over 80% of the energy demand by 2050. With the raise of renewable energy sources, the need for storage possibilities is also getting more and more important, as renewables are more dependent on present conditions [1, 2, 3, 4].

The increasing energy demand is surely connected with the fact that the world is getting technologically more advanced in a fairly quick way. To keep that advance more economic and ecologic, the trend is going in the direction of making processes more efficient and devices even smaller. One technology, which is expected to dominate the future is the Internet of Things (IoT). The IoT connects and will connect billions of sensors and devices, making processes more efficient and providing valuable data in many fields of interest [5]. To power such unwired minimised wireless sensor nodes, a sustainable way is needed, especially for sensors, which are placed in hardly accessible or hazardous places. A common small scale battery has a limited lifetime and would have to be changed repeatedly. Therefore, a device is needed that can harvest and store energy all in one and also work under harsh conditions.

The combination of generating and storing solar energy, for example, could be fulfilled by combining a solar cell with a solid oxide fuel (SOFC) or electrolysis cell (SOEC). As solid oxide fuel or electrolysis cells work best at elevated temperatures, also high temperature solar cells are needed. As the commonly used silicon based solar cells have a decreasing efficiency when temperatures rise, high temperature solar cells have to be found, which can be combined with such solid oxide fuel/electrolysis cells [6].

This leads us to solid oxide solar cells, which have attracted more interest over the past few years [7]. Solid oxide solar cells would be able to work at elevated temperatures and are thus a good candidate for a coupled device resulting in a solid oxide photoelectrochemical cell or "harvestorer". The operation of unwired minimised wireless sensor nodes for the Internet of Things would be a perfect field of application for so called micro-harvestorers (μ-HS). These μ-HS could power IoT nodes from ubiquitous heat and light, replacing small batteries. Such a replacement would have environmental and economic benefits like low installation and maintenance costs. They could also be placed in hazardous environments as a long term solution. Nowadays, micro-harvesters (micro photovoltaic cells) produce output powers of around 1-100 μW, which is well below a needed power of around 10 mW/cm^2. Therefore, improvements have to be made on the output power of micro-harvesters and on the power consumption of sensor nodes. A sketch of such a photoelectrochemical μ-HS is depicted in figure 1.1. The light is absorbed by the photovoltaic cell on top, generating electron hole pairs, which build a potential when separated due to a space charge, for example. The generated electrons can be used to power the SOEC cell, working in electrolysis mode, splitting water or pumping O_2. If water is splitted, also H_2 is produced. Now solar energy is stored. If energy is needed, the SOEC is operated in fuel cell mode, producing electricity to power e.g. WSN [8]. Alternatively, recently developed oxide ion batteries may replace the SOFC/SOEC cell in the harvestorer [9].

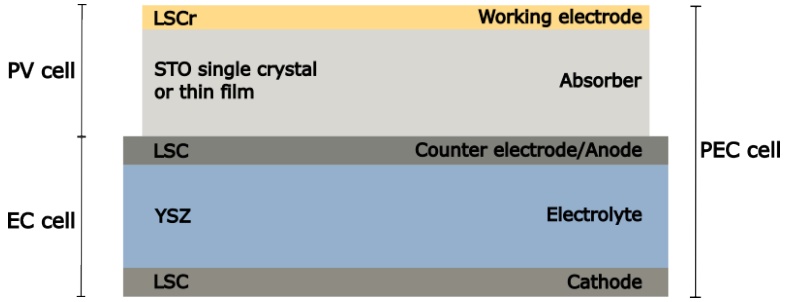

Figure 1.1: Sketch of the structure of a exemplary photoelectrochemical cell or "harvestore" application [8].

Knowing that $SrTiO_3$ (STO) as a single crystal has the potential of being used in high temperature solar cell applications when combining it e.g. with a $(La,Sr)CrO_3$ LSCr top electrode [10], the question arose, if also STO thin films can be used as such, making the harvestorer even smaller and thus more economic to produce. Therefore, high temperature STO thin film based solid oxide solar cell samples were prepared and investigated in order to determine, whether STO thin films can work in such micro solar cell applications, and further to get a better understanding of electrical and defect chemical processes in such cells under operation. The preparation was done with pulsed laser deposition (PLD). The solar cell is ablated onto a 10 x 10 mm^2 $SrTiO_3$ single crystal in three steps, growing layers of $(La,Sr)CoO_3$ (LSC) (counter electrode), $SrTiO_3$ (absorber layer) and LSCr (working electrode). To analyse the samples, different methods are applied, such as electrochemical impedance spectroscopy (EIS), voltage and current measurements under UV light, transmission electron microscopy (TEM) and mass spectrometry (Online-LASIL-ICP-MS, LA-ICP-MS).

2 Theoretical Background

2.1 Strontium titanate

Ceramic materials, like $SrTiO_3$ (STO), have become more and more important in the last couple of years due to their ability to transport electrons and ions, depending on the present temperature, condition, or composition. Many of these electroceramics are oxides in a perovskite structure. Strontium titanate as such a perovskite-type oxide has become a model material for electroceramic oxides, because of its pronounced chemical and thermal stability as well as its well-known defect chemistry [11]. Since STO thin films are the main topic of this work, a brief overview of the properties of STO single crystals is given. Furthermore, a brief overview of the observed behaviour of STO thin films is given.

2.1.1 Structure and defect chemistry

Strontium titanate is a perovskite material with a ABO_3 structure ($SrTiO_3$). It consists of an TiO_6 octahedra, surrounded by eight strontium atoms sitting in the corners, as depicted in figure 2.1. This cubic structure is present at temperatures above ≈ 105 K. Under this certain temperature, a phase transition occurs, changing the cubic to a tetragonal structure. This transition leads to tilted oxygen octahedra rotated around the titanium ions [12]. At room temperature, STO is transparent and has a lattice constant of 3.905 Å [13].

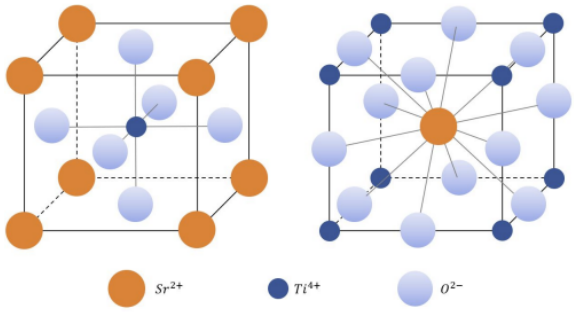

Figure 2.1: Structure of the $SrTiO_3$ perovskite. On the left, the Ti^{4+} is centred, on the right, Sr^{2+} [14].

Before treating the well-known defect chemistry of STO, a brief introduction of general defect chemistry is given. Defects play a key role in chemical and physical behaviour of solids, allowing the tailoring of material properties over a broad parameter range. This is the reason they are being highly investigated in modern science and technology, e.g. for the application in high temperature solar cells.
Defects, especially point defects, are always present in real crystals. This is due to the fact that for constant pressure and temperature the Gibbs energy (equation 2.1), which can quantify the energy of a system, always seeks a minimum. In equation 2.1, H is the enthalpy, S the entropy and T the temperature in Kelvin.

$$G = H - T\,S \tag{2.1}$$

The Gibbs energy as a function of the number of point defects in figure 2.2 shows that at the minimum of ΔG_V, which is the point of equilibrium, vacancies are present. Point defects thus can not be fully removed by thermal treatment, but are always present. Such defects are called intrinsic defects. Furthermore, knowing that the Gibbs energy of a crystal containing intrinsic defects is lower than the one from a perfect crystal, the defect population can be treated as a chemical equilibrium [15]. Consequently, defect formations can be considered as the migration of an atom within a crystal to the surface to increase the volume of the solid or to evaporate, leaving a vacancy in its place. To describe the vacancy generation, the law of mass action can be applied, assuming there is no interaction between the defects. The equilibrium constant for vacancy generation K_V is

given by:

$$K_V = \frac{n_V}{N} = exp\left(\frac{-\Delta G_V}{RT}\right) \tag{2.2}$$

where ΔG_V is the local change in Gibbs energy due to defect formation, n_V/N the concentration of defects per atom site, R the gas constant and T the temperature in Kelvin [15].

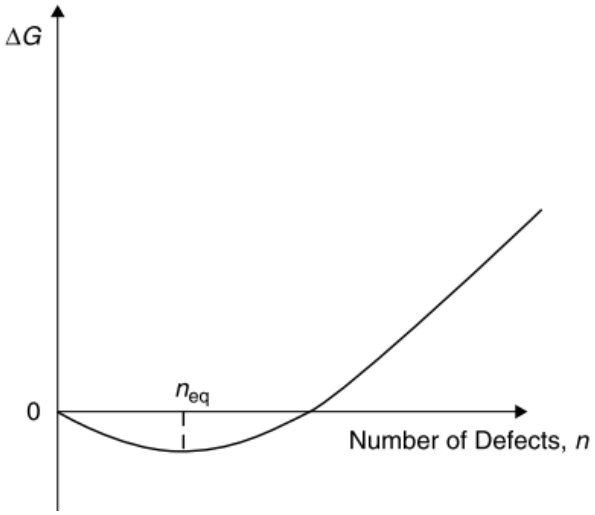

Figure 2.2: Schematic graph of the change in Gibbs energy ΔG as a function of number of point defects present. At equilibrium, n_{eq} defects are present in the crystal [15].

Knowing that the formation of defects is a reversible process in the sense of thermodynamic equilibrium, it is now possible to further describe them.
The defect chemistry of $SrTiO_3$ is giving important insights into the physical and chemical behaviour of the material. A variety of defects can occur in pure STO including point defects, long-range disorders like edge dislocations as well as planar defects. Point defects are the main contributors for mass and charge transport. Their concentration and mobility are highly dependent on the environment the sample is in [13, 16]. When working with point defects, it is necessary and useful to introduce the Kröger-Vink notation. Its basic scheme is shown in equation 2.3. The latter M corresponds to the species. This can be atoms of a certain element (e.g. Sr, Ti, O, ...), vacancies (V), electrons (e) or holes (h). S is referred to the lattice site that the certain species occupies, it may also be an interstitial site (i). C is related to the electronic charge of the species relative to the site it occupies. The charge is calculated by subtracting the charge of the current site from the charge of the original site. If the relative charge is zero (electroneutral), it is represented by x ($^{\times}$). Positive relative charges are represented by dots ($^{\bullet}$), negative relative charges by dashes ($'$). Equation 2.4 states an example of the notation, giving a negative oxygen vacancy in an oxide [17].

$$M_S^C \tag{2.3}$$

$$\mathrm{V}_{\mathrm{O}}^{\bullet\bullet} \tag{2.4}$$

In STO, point defects can occur either as interstitials or vacancies, although vacancies are energetically favoured. The fundamental intrinsic disorder reaction in STO is the partial Schottky reaction given in equation 2.5. This reaction is important at temperatures around 1200°C, where, for example, samples are prepared [11].

$$Sr_{Sr} + O_O^{\times} \rightleftharpoons V''_{Sr} + V_O^{\bullet\bullet} + SrO \tag{2.5}$$

At lower temperatures, Sr vacancies aren't mobile any more and freeze in. Therefore, it is always important to keep the thermal treatment in mind when working with STO, as it can strongly influence the behaviour of STO [11].
The generation of electrons and holes, see equation 2.6, as well as the reaction of oxygen vacancies with gaseous oxygen, where oxygen may be incorporated into the lattice as $O_O^{\times}$ annihilating an oxygen vacancy $V_O^{\bullet\bullet}$ or vice versa, depending on the oxygen partial pressure, are of importance for the samples' defect chemistry, also at lower temperatures [11]. The incorporation of oxygen into a twofold positively charged vacancy is shown in equation 2.7, creating two electron holes. It is also possible to write the reaction regarding conduction band electrons, leading to equation 2.8 [13, 18].

$$\text{nil} \rightleftharpoons e' + h^{\bullet} \tag{2.6}$$

$$\frac{1}{2}O_2 + V_O^{\bullet\bullet} \rightleftharpoons O_O^{\times} + 2h^{\bullet} \tag{2.7}$$

$$O_O^{\times} \rightleftharpoons \frac{1}{2}O_2 + V_O^{\bullet\bullet} + 2e' \tag{2.8}$$

Furthermore, oxygen vacancies can get single ionised at low temperature, trapping a free electron according to equation 2.9 [18].

$$V_O^{\bullet} \rightleftharpoons V_O^{\bullet\bullet} + e' \tag{2.9}$$

The electronic conductivity of STO thus can vary from n-type conduction in reducing conditions over intrinsic conductivity to p-type conduction in oxidising conditions [13]. In figure 2.3 a sketch of a Brouwer diagram of a metal oxide is shown, giving an idea of the dependencies between defect chemistry and oxygen partial pressure. In addition to these defect equilibria, cation vacancies or impurities can significantly change the defect concentrations in STO. They can be brought in while growing the crystal or while other preparation steps. Depending on their valence state, they can act as donor or acceptor dopants or be charge neutral [13]. The substitution of aliovalent cations for Sr^{2+} or Ti^{4+} is accompanied by the formation of ionic and electronic defects to maintain overall electroneutrality, the relative amount of which depends on the oxygen partial pressure. Donor dopants, e.g. M^{3+} on a Sr^{2+} site or M^{5+} on a Ti^{4+} site are compensated by V''_{Sr} or e'. Acceptor dopants, e.g. M^{2+} or M^{3+} on a Ti^{4+} site, are compensated by forming $V_O^{\bullet\bullet}$ or $h^{\bullet}$. Moreover, acceptors can trap electron holes like in the aforementioned interaction of electrons with oxygen vacancies [11, 18].
It is important to keep in mind that due to the large influence of point defects, even single crystals produced under different conditions can have different properties [18]. Also, defects can be responsible for changing electronic energy levels in the band structure, leading to different mechanisms when being irradiated [13].

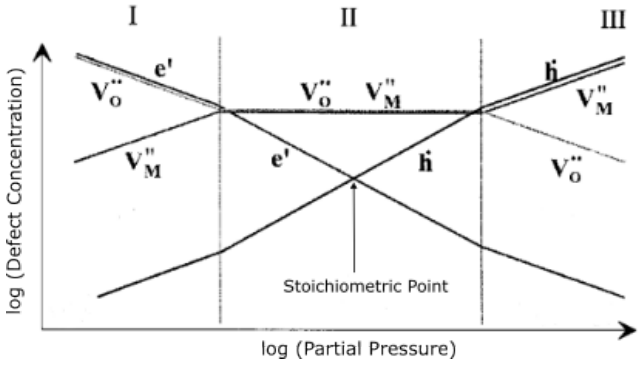

Figure 2.3: Sketch of a Brouwer diagram giving the relation of defect concentration and oxygen partial pressure of an undoped metal oxide ($MO_{1-\delta}$) from [17]. Sector II marks intrinsic conductivity. In sector I $\delta > 0$, the metal oxide is n-type conducting. In sector III $\delta < 0$, resulting in a p-type conductivity.

2.1.2 STO thin films

The defect chemistry of STO thin films is not yet as well investigated as the one of STO single crystals. Strong deviations in electrochemical behaviour have been reported due to e.g. cation non-stoichiometry, leading to a highly reduced conductivity [19, 20, 21]. Also, for doped and undoped STO thin films, a different behaviour of the oxygen partial pressure dependent conductivity was observed, if compared to the one of bulk STO. Furthermore, a n-type conductivity increase and p-type conductivity decrease with decreasing film thickness is reported. This is attributed to the charge carrier redistribution in the surface space charge layers. Space charges seem to play an important role in thin films, owing to the high surface to volume ratio [22, 23, 24].

Morgenbesser et al. [20] investigated different STO thin films prepared by pulsed laser deposition, unrevealing ultra-low conductivity. Besides undoped STO thin films, also different dopants (Fe, Al, Ni) were investigated. Electrochemical impedance spectroscopy (EIS) revealed a pseudo-intrinsic behaviour of the conductivity for high dopant concentrations up to several percentages. Additionally, inductively coupled plasma optical emission spectroscopy (ICP-OES) and reciprocal space mapping (RSM) were used to show a severe Sr deficiency in the thin films. Positron annihilation lifetime spectroscopy (PALS) revealed Sr vacancies as predominant point defects, contrary to oxygen vacancies in STO single crystals. Furthermore, a change in site occupation (Ti on Sr site) is observed for Fe-doped STO thin films by synchrotron-based X-ray standing wave (XSW) and X-ray absorption spectroscopy (XAS).
Morgenbesser et al. [20] introduced a model deduced from their measured data, trying to explain the pseudo-intrinsic behaviour of STO thin films. The effect occurred for all used dopants (Fe, Ni, Al) as well as undoped STO. Furthermore, p_{O_2} variations between 10^{-5} and 1 bar did not change the conductivities, leading to a what seems like mid-gap Fermi level pinning. Such a pinned Fermi level can emerge, if mid-gap acceptor states and a donor dopant are present. A sketch of the band scheme is depicted in figure 2.4.
In the specific case of STO, the determined Sr vacancies act as acceptors, leading to electron holes. A counterbalancing by oxygen vacancies is neglected. The energy of this first hole trapping is assumed to be mid-gap.

$$V'_{Sr} \rightleftharpoons V''_{Sr} + h^{\bullet} \tag{2.10}$$

The second hole trap is considered shallow.

$$V^{\times}_{Sr} \rightleftharpoons V'_{Sr} + h^{\bullet} \tag{2.11}$$

The formation of V'_{Sr} by a hole trapping in equation 2.10 can pin the Fermi level mid-gap. Equation 2.11 adds more holes to those created by other acceptor dopants like Fe [20]. Additionally, reduced electron and hole mobilities in defect rich thin films can play a role for the pseudo-intrinsic behaviour. This means that the Fermi level doesn't have to be exactly mid-gap. E.g. a pinned state deviation of 30 meV combined with a three times lower mobility also ends in pseudo-intrinsic behaviour [20].
Moreover, donor states have to be considered, where partial occupations of the A-site cations (Sr) by B-site cations (Ti) are a realistic possibility. In Fe doped STO, this was observed, changing the acceptor dopant to a donor dopant, when Fe^{3+} is positioned on the A-site.

$$Fe^{\times}_{Sr} \rightleftharpoons Fe^{\bullet}_{Sr} + e' \tag{2.12}$$

Due to the larger ionic radius of Fe^{2+} ($Fe^{\bullet}_{Sr}$) compared to Fe^{3+}, Fe^{2+} fits better on the A-site. The trapping energy of equation 2.12 thus might be quite high, leading to a corresponding energy level far below the conduction band. As long as the energy level is above mid-gap, the site change would lower the Sr vacancies as well as introduce donor states which activate the Fermi level pinning in mid-gap. XAS measurements indicated that one third of the Fe is at the A-site. All Fe^{2+} was attributed to the A-site, the rest would be Fe^{3+}, leading to a mixture of oxidation states at the A-site occupations. According to their measurements, Fe donor states then are just above the Fermi level.
So, the existence of Fe^{2+} excludes that $Fe^{\bullet}_{Sr}$ is far above mid-gap, meaning that Fe is not the donor matching the model [20]. It also wouldn't have explained the behaviour in undoped STO.
Morgenbesser et al. [20] thus suggested Ti on A-sites as donors present in thin films. This was already observed experimentally and predicted theoretically in literature [25, 26, 27, 28]. They act as donors according to equation 2.13.

$$Ti^{\bullet}_{Sr} \rightleftharpoons Ti^{\bullet\bullet}_{Sr} + e' \tag{2.13}$$

The energy of this reaction is supposed to be far above mid-gap. This means, that just Ti ions on A-sites as well as A-site vacancies lead to the pseudo-intrinsic behaviour. The Fermi level is pinned or close to mid-gap positions, not even changing when additional dopants are in the crystal.
The neglect of oxygen vacancies as donors in STO thin films also seems justified, as the oxygen vacancy concentration in electronically intrinsic thin films (low $[h^{\bullet}]$) is very low, due to the mass action law of the oxygen incorporation reaction [20, 29].
The found Sr deficiency (cation non-stoichiometry) in STO thin films can be compensated by PLD-targets with Sr excess. It was shown for Fe-doped STO, that 7% overcompensation, resulted in nearly stoichiometric thin films (a Sr/Ti ratio of 1), that consequently showed bulk like properties [19].

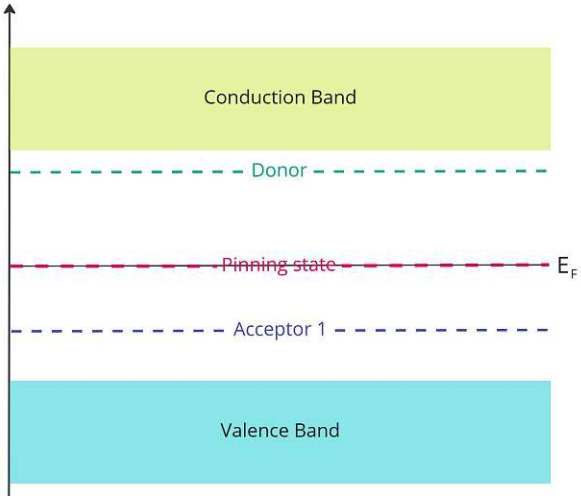

Figure 2.4: Sketch of the Fermi level pinning due to a donor and two acceptor states. Acceptor 2 would be at the same energy level as the pinned state in mid-gap.

2.2 Photovoltage

As STO thin film based solar cells are the key issue of this thesis, also the light interaction with STO single crystals as well as STO thin films is dealt with. As STO is a semiconductor, a brief introduction of the general process of the formation of photovoltage in semiconductors is given.
Photovoltage in semiconductors generally occurs, when light with an energy above the semiconductors band gap energy is absorbed and electron-hole pairs are formed. Further important is a space charge zone, which guides the generated electrons and holes in a certain direction, building an inner potential difference. When, for example, one n-doped and one p-doped semiconductor is put together, space charge zones arise. Due to the different Fermi levels, the two gathered semiconductors start exchanging their majority charge carriers until an electrochemical equilibrium of the Fermi level is found. The holes from the p-doped semiconductor diffuse to the n-doped side, and vice versa. The charge carriers recombine with the respective other charge carrier type. The driving force is the electrochemical potential, seeking equilibrium. When this equilibrium state is reached, an inner electric field is present, the space charge zone. The electric field of the space charge zone points towards the p-doped side, as the electron concentration there is bigger. The electric field generates a small drift current in the opposite direction. An equilibrium is formed, in which diffusion current and drift current of charge carriers keep the equilibrium, as shown on the left in figure 2.5. The space charge zone is depleted as a result of recombination of the mobile charge carriers [13, 16].
The photo-generated electron-hole pairs diffuse to the p-n junction and separate at the space charge zone, building a forward photovoltage, depicted on the right in figure 2.5. Forward, because the electric field of the generated carriers is opposite to the build in field of the p-n junction. As a consequence, the space charge zone shrinks or even disappears [13, 16].

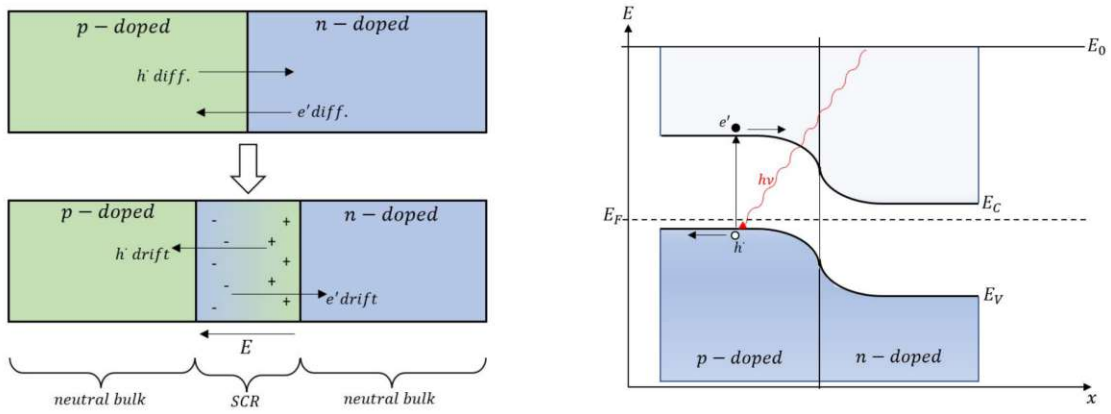

Figure 2.5: Left side: Sketch of the formation of a space charge region when combining a p-doped and an n-doped semiconductor. Right: Formation of an electron-hole pair due to the absorption of a photon ($\hbar\omega$) at an p-n-junction [14].

Similar effects can also occur at heterojunctions, surface-interface transitions or p-i-n junctions. At p-i-n junctions an intrinsic semiconductor is positioned between the p- and n-doped part. When a metal and a semiconductor is brought together, a so called Schottky junction is formed. At Schottky junctions, the space charge zone usually forms just in the semiconductor band [16].

2.2.1 Basic interaction of STO with light

STO is a semiconductor with a wide direct band gap of around 3.25 eV [30]. When temperatures are rising, the band gap is declining significantly to values of around 2.6 eV at around 1000°C, meaning, the number of mobile electric charge carriers increases [13]. Due to the large band gap, the versatility of pure STO is limited, considering absorption properties. It can be tailored into certain ways or characteristics through doping, though. A slight Fe doping on the B-site (Ti) is lowering the band gap for instance. A-site donor doping with La, for example, can turn STO into an n-type semiconductor. Furthermore, photochromism and photocatalysis are achievable effects [13].
When pure STO is irradiated with light that has sufficient energy to excite electrons from the valence band to the conduction band, a variety of effects can occur, including photoconductivity, photoluminescence, photovoltage, photochromism and photocatalysis as well as stoichiometry changes in the bulk [13]. Figure 2.6, made by Siebenhofer et al., shows the basic concepts in terms of band structure. The effect of photovoltage at elevated temperatures, as the main interest in this work, will be discussed in more detail in the next subsection.

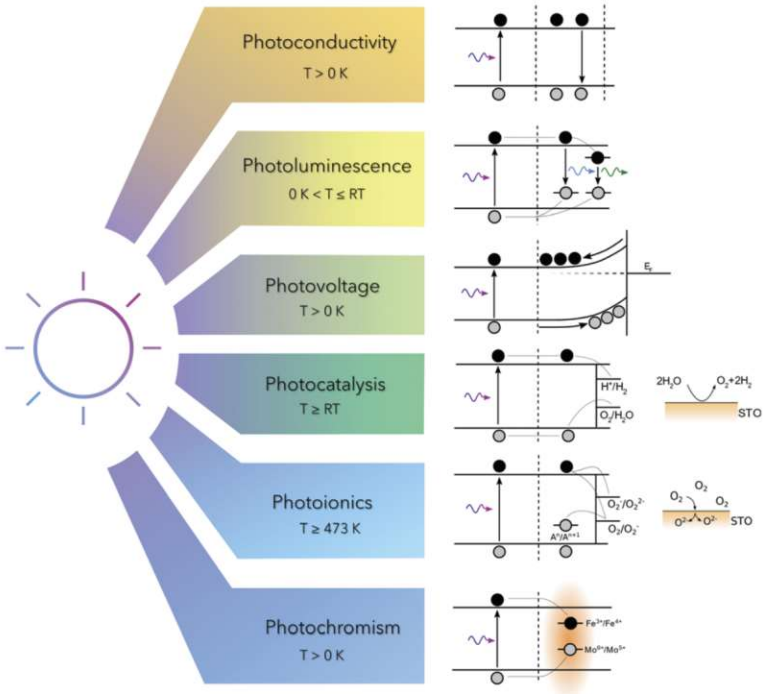

Figure 2.6: Sketch of basic mechanisms occurring in STO while illuminated with ultraviolet (UV) light at different temperatures [13].

2.2.2 Voltage generation in STO single crystals under UV light at elevated temperatures

Since STO is a semiconductor, it can develop a photovoltage on an interface with a current collector. As declared in subsection 2.2, at such an interface, an electrostatic potential is expected, e.g. a space charge potential. The generation of photovoltage has mainly been attributed to the generation of this resistive space charge zone at an STO/electrode interface, which collapses under the irradiation of UV light. Thus, the illumination of the STO single crystal with UV light, together with the diffusion of the photo-generated charge carriers along this interface, modifies the space charge zone. The result is a kind of Schottky solar cell.
An exact understanding of the origin of the photovoltage has yet not been achieved, as the space charge region at the current collector/STO interface is most likely affected by oxygen vacancies and their chemical potential differences between the interface and the bulk. These oxygen vacancies in STO single crystals are the major

charge carriers compared to electrons, thus, holes may just follow the space charge profile of the oxygen vacancy depletion [31]. Also, the general change of the defect chemistry because of oxygen incorporation under UV light with time in such surface areas makes the situation even more complex.
It has though been demonstrated by Walch et al. [31], that STO is suitable as a photo-active absorber in solid oxide solar cell applications or solid oxide photoelectrochemical cells (SOPEC) at temperatures between 400 °C and 500 °C. They also observed a time-dependent decline of photovoltage, which they connected with the lowering of the oxygen vacancy concentration by UV light, reducing the corresponding space charge potential at the interface. This enhanced oxygen uptake under UV light at elevated temperatures was already observed for iron doped STO by Merkle et al. [32]. Additionally, a battery type voltage was observed after switching off the UV light. After the photovoltage went down to zero, the changed oxygen stoichiometry persists and is no longer in equilibrium with the gas phase. The battery voltage results due to the different oxygen potentials present. The incorporated oxygen then is slowly released, decreasing the battery voltage, until an equilibrium is found again. To measure that battery voltage, an electrochemical cell with an oxide ion electrolyte (YSZ) and a counter electrode (Pt paste) was built. The highest voltages of around 300 mV were found using Au as current collectors on top of the STO.
Brunauer et al. [10] showed increased photovoltage for different top electrode materials on STO single crystals. $(La_{0.8}Sr_{0.2})CrO_3$ (LSCr) was identified as the best option, reaching voltages of up to 1 V. Similar results were found by Morgenbesser et al. in [33].
Morgenbesser et al. [33] also observed a time dependent open circuit voltage (OCV) at the LSCr/STO interface like [10]. As this behaviour was also measured in this work, it is explained in a bit more detail. When the UV light is turned on, the voltage first increases until a maximum is found. When the UV light is turned off, a voltage remains. Since the space charge should immediately relax after the UV light irradiation, the photovoltage should immediately go to zero. A time dependent decrease was though observed. Morgenbesser et al. [33] explained it as follows: The chemical potential of oxygen given in equation 2.14 is composed of the difference between the chemical potentials of ionic and electronic species.

$$\mu_O = \mu_{O^{2-}} - 2\mu_e = -\mu_{V_O} + 2\mu_h \tag{2.14}$$

In contrast to the above described battery voltage observed by [31], where no LSCr layer was on top of the STO and a positive signed battery voltage was detected, here the UV light does not directly accelerate the oxygen incorporation but splits the chemical potential μ_e into two quasi Fermi levels, one for the electrons and one for the holes. Thus, two quasi chemical potentials of formally neutral oxygen are build. Those two quasi chemical potentials show gradients because of a varying absorbance (UV light absorbance of around 2-3 μm [33]), causing oxygen diffusion within the STO. Depending on the local concentrations of holes and electrons, the irradiated STO region enriches or depletes of oxygen vacancies. Oxygen gets pumped from irradiated locations into dark locations by chemical diffusion. This results in two different defect chemical states (and quasi Fermi levels) of the irradiated parts and the dark parts, which does not react as fast as the space charge region to a turned off UV light, thus sustain a chemical potential difference over a longer period of time. This explains the change in OCV during UV light irradiation, as the oxygen relocations have to happen.
Therefore, if the UV light is switched off, all photoelectric effects are gone. Just the irradiated 2-3 μm are enriched with oxygen vacancies and have a lower chemical potential of oxygen compared to the dark STO. This causes a battery voltage, which has a switched polarity than described above and observed by Merkle et al. [32]. With time, the oxygen chemical potential relaxes by diffusion inside the dark STO and oxygen incorporation via the top layer [34].
Furthermore, a time dependent current was observed by Morgenbesser et al. [33] for the same sample. They attributed this to a stoichiometry polarisation. When current flows, the voltage drops external but also inside the cell. When measuring in short circuit mode, the whole voltage is consumed by the sample. As STO is a mixed conducting material, ions are blocked at the electrodes. When voltage is applied, an oxygen stoichiometry polarisation builds. Meaning an oxygen vacancy depletion on the positive charged electrode and their accumu-

lation at the negative one. This can also lead to a drop in resistance, as also an electron and hole rearrangement takes place due to charge neutrality [35, 36]. Through that, higher conductive regions can form as the resistivity decreases, growing over time. This then leads to a growing current. The applied voltage mentioned is in this case the one of the solar cell. As this resistivity decreases over time, Morgenbesser et al. called this effect "self-enhancement" effect [33].
Brunauer et al. [10] also stacked the photovoltaic cell (based on a $(La_{0.8}Sr_{0.2})CrO_3/SrTiO_3$ junction) onto a solid-state electrochemical cell (with a zirconia solid electrolyte and a shared $(La,Sr)FeO_3$ electrode). Photo powered oxygen pumping from low to high oxygen partial pressures was achieved. This proofs, that the concept of solar to fuel conversion by high temperature solid oxide electrochemical cells is possible. Moderate improvements could lead to voltages and currents that allow water splitting in a steam based high temperature photoelectrochemical cell [10]. The European Unions (EU) "Harvestore" project has comparable goals. A device that can harvest solar energy and store it as chemical energy for powering small applications is desired.

2.3 Harvestore project

2.3.1 Aim of the project

The Harvestore project is a EU funded project with the objective of a breakthrough in micro-energy harvesting and storage technology ("μ-harvestorers", μ-HS) for powering autonomous wireless sensor nodes (WSN) for the future Internet of Things (IoT). The IoT is considered one of the five technologies that will change the world by connecting 27 billion devices and generating 2 trillion euro market by 2025. The main goal of the Harvestore project is the powering of these IoT nodes from ubiquitous heat and light sources by using nano-enabled micro-energy systems with a footprint below one cm^3. One of the intermediate products needed for such μ-energy application is a high temperature photovoltaic cell, which can operate at temperatures between 200-600°C, producing power up to 10 mV/cm^2 at 1.2 V having a footprint of 1 cm^2/1 mm [8]. This proposed goal closes the circle to this work, where a $SrTiO_3$ thin film based high temperature solid oxide solar cell with a small footprint is investigated and checked for feasibility.

2.3.2 From single crystals to thin films

Coming from STO single crystal samples and their reported results, the question arose if a similar photo-activity could be found for STO thin films. Thin films would probably have the advantage of a potential power increase due to an expected lower resistance. A smaller size would also be relevant for micro energy harvesting applications like desired in the Harvestore project. The known differences between STO single crystals and STO thin films per se are a challenging starting point, due to for example the changed surface/volume ratio [24, 19]. Added to this, the preparation also states a lot of known difficulties like the thin film stoichiometry, when trying to produce a bulk like STO thin film [37, 38, 39, 40].

Morgenbesser et al. [22] conducted investigations on STO thin films in solar cell applications, trying different superstructures including STO thin films on STO single crystals with a $(La_{0.9}Sr_{0.1})CrO_3$ (LSCr10) thin film as working electrode as well as STO thin films on $(La_{0.6}Sr_{0.4})CoO_3$ (LSC) thin films as counter electrode and a LSCr10 top electrode, all deposited on a sapphire single crystal. On top of the samples, Pt current collectors were used.
Samples with undoped STO thin films being deposited on a single crystal showed similar results as single crystal samples with LSCr top electrodes. For doped thin films, a decrease in photovoltage was found. Stoichiometric thin films (prepared with 7% Sr excess in the target) yielded more than double the amount of photovoltage (around -1 V) than Sr deficient thin films, leading to a clear influence of cation stoichiometry to the photovoltage. Surprisingly, for thin films prepared with an undoped and uncompensated target, which should be Sr deficient, the same voltage was obtained as with stoichiometric films. This could be because of the mentioned Fermi level pinning in STO thin films. The Fermi level of the thin film (pinned in mid-gap) is higher than the Fermi level of the single crystal (slightly p-doped), coming close to the Fermi level of LSCr, leading to a gap between STO thin film and STO single crystal, resulting in a similar photovoltage than just LSCr thin films on STO single crystals. A sketch of the supposed band scheme is shown in figure 2.7.
Since STO thin films deposited on STO single crystals gave significant photovoltage, also thin film solar cells were investigated. The results were low photovoltages for all investigated geometries including LSCr10 thin film/STO thin film/Nb:STO single crystal, LSCr10 thin film/STO thin film/YSZ single crystal superstructures, using Pt paste as counter electrode and a Pt grid as current collectors on the LSCr top electrodes as well as a LSCr10 thin film/STO thin film/LSC thin film/sapphire single crystal superstructure using the LSC thin film as counter electrode and again a Pt grid on the top LSCr10 electrode.
One can see, that undoped STO as substrate brings better results than other substrates, leading to further investigations in that area in this work. Max Morgenbesser [22] concluded, that the LSCr/STO thin film interface alone seems to fail in leading to a photovoltage. Just when combining it with a STO single crystal, it seems to result in reasonably high enough photovoltages.

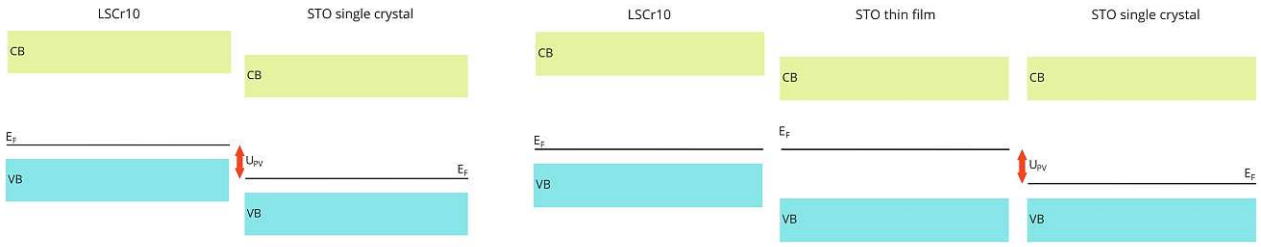

Figure 2.7: Sketch of the band structure of the LSCr/STO single crystal heterojunction (left) and of the LSCr/STO thin film/STO single crystal heterojunction (right), both leading to similar photovoltages.

This conclusion was disproved in this work, as it was shown that thin film based solar cells can be successfully prepared, though with many uncertainties in the understanding of the origin of the photovoltage, and the key parameters while preparation.

2.4 Pulsed Laser Deposition (PLD)

Pulsed laser deposition was used to produce all samples in this thesis. In figure 2.8, a sketch of the PLD setup used for this work can be seen. It consists of a vacuum chamber, where the whole setup is placed and the laser, which is directed into the chamber through a window.
Pulsed laser deposition is a rather easy and common method in research to produce thin films. Pulsed laser deposition is a form of physical vapour deposition (PVD). Physical vapour deposition processes are atomistic deposition processes in which material is vaporised from a liquid or solid target. The vaporised atoms or molecules then move through a low pressure or vacuum environment onto a substrate, where it condenses [41]. For the growth of crystalline oxides, pulsed laser deposition turns out to be one of the most effective methods [42].
In pulsed laser deposition, the ablation is achieved with a pulsed laser, which is focused onto a target of the chosen material to be deposited. The pulsed laser beam hits the target, gets absorbed and subsequently vaporises the material. At high laser fluences, a non-equilibrium state is reached, leading to an independence of the evaporation from the vapour pressure of the ionic species, allowing stoichiometric ablation onto the substrate. A plasma plume is generated due to the absorption of high energy densities by a small volume. The growth of complex oxides presupposes a growth flux with correct stoichiometry in an oxidising ambient that is favourable for the desired phase formation [42]. It was though found that a stoichiometric deposition of oxide thin films is much more complex than assumed [37, 43].
The growth rate of the ablated layer depends on multiple factors such as target-substrate distance, background gas pressure, laser spot size and laser energy densities [42]. Also, the temperature of the substrate has a certain effect on the morphology and growth [44]. This is why the sample holder is often placed on a heater. As the laser pulses ablate a good amount of material from the target, it is beneficial to rotate the target whilst ablation, focusing the laser spot slightly off centre to get an evenly distributed ablation.
Derived from this, every target material requires specific parameters for the deposition process. Those parameters can vary on every PLD and are very sensitive to small changes that might appear. This can make it quite hard to get reproducible thin films in terms of stoichiometry. Two important parameters when depositing oxide thin films are the laser energy density as well as the laser spot size [43]. Varying results have been published for the stoichiometric deposition of STO thin films, reaching from fluences of 1.3 J/cm^2 to 0.3 J/cm^2 [37, 38]. At this point it is again stated, that stoichiometry variations of STO thin films are known and that a Sr deficiency has also been observed when depositing STO thin films. [37, 38, 39, 40].

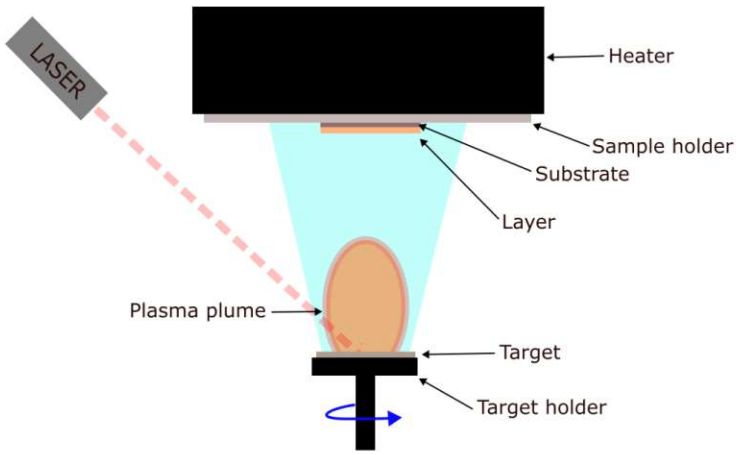

Figure 2.8: Sketch of the "new" PLD setup at TU Vienna used for this work.

2.5 Electrochemical Impedance Spectroscopy (EIS)

Impedance spectroscopy is a powerful technique to analyse and characterise properties in electrochemistry and solid state ionics. EIS has a rather simple experimental setup as well as a non-destructive use, which makes the technique popular in many fields of research. In comparison to a conventional two-point direct current measurement, which gives an average resistance value, EIS has the ability to also give information regarding different contributions to the resistance. The only downside is the complex and challenging interpretation of the gained data.

2.5.1 Working concept of EIS

In impedance spectroscopy, the resistance response of alternating current or potential in a direct current or potential circuit is measured. EIS is used to analyse the volume and surface properties of a system by fitting with circuit elements. This method differentiates the responses of the various processes in our system based on the time constant of their response to an analysed interference [45].
When talking about alternating potential or current, sinusoidal waves have to be consequently introduced. Sinusoidal waves are time dependent. If now an alternating sinusoidal potential $E(t)$ (equation 2.15) with E_0 as the amplitude, ω the angular frequency and t the time, is applied to an electrochemical system, the response will be a sinusoidal current wave (equation 2.16) with an amplitude I_0 and a potential phase shift ϕ. Putting equations 2.15 and 2.16 in relation, one gets the impedance Z shown in equation 2.17 [45].

$$E(t) = E_0 \, sin(\omega t) \tag{2.15}$$

$$I(t) = I_0 \, sin(\omega t + \varphi) \tag{2.16}$$

$$Z = \frac{E(t)}{I(t)} = \frac{E_0 \, sin(\omega t)}{I_0 \, sin(\omega t + \varphi)} = Z_0 \frac{sin(\omega t)}{sin(\omega t + \varphi)} \tag{2.17}$$

To simplify expressions and calculations, the quantities are expressed with the complex notation using the imaginary unit $j = \sqrt{-1}$. The potential $E(t)$ and the current $I(t)$ are now written as in equation 2.18. The impedance as a complex number follows in equation 2.19. It is the ratio of potential amplitude and current amplitude and a phase factor. A phase angle of 0° represents a purely ohmic behaviour. A phase angle of -90° is contributed to a capacitive behaviour and an angle of 90° to an inductive one [45].

$$E(t) = E_0 \, exp(j\omega t), I(t) = I_0 \, exp(j\omega t - \varphi) \tag{2.18}$$

$$Z(\omega) = Z_0 \, exp(j\varphi) = Z_0 \, (cos(\varphi) + j \, sin(\varphi)) \tag{2.19}$$

Kirchhoff's laws are applied, when working with more than one impedance. In equation 2.20 the calculation rule for two serial impedances is demonstrated, equation 2.21 shows two parallel impedances. The impedance of a resistor, an inductor and a capacitor is given in equations 2.22, 2.23 and 2.24.

$$Z_{1-2} = Z_1 + Z_2 \tag{2.20}$$

$$Z_{1||2} = \frac{Z_1 Z_2}{Z_1 + Z_2} \tag{2.21}$$

$$Z_R = R \tag{2.22}$$

$$Z_I = j\omega L \tag{2.23}$$

$$Z_C = \frac{1}{j\omega C} \tag{2.24}$$

2.5.2 Analysis and visualisation of EIS

There are two main ways to visualise gained data from impedance spectroscopy measurements.

- **Nyquist plot** - where the imaginary impedance is on the y-axis and the real part on the x-axis.
- **Bode diagrams** - the absolute impedance $|Z|$ or the phase shift ϕ on the y-axis is plotted against the frequency ω on the x-axis.

The Bode diagrams are not from importance in this work, so they will not be discussed in more detail.

The Nyquist plot compares the imaginary impedance with the real part of it. It plots the data according equation 2.19. On the y-axis, the negative imaginary part of the impedance is plotted (Z_{Im} or Z'') and on the x-axis the real part of it (Z_{Re} or Z'). The frequency is changed from high (MHz) to low (mHz) ranges, to gain a frequency dependent spectrum. As physical phenomena happen at different time scales/frequencies, the data can bring valuable information about processes and location. Everything that slows down electrons in a certain frequency range will be measured. An example of two Nyqusit plots is given in figure 2.9 [45] [46].

To analyse the measured spectrum, equivalent circuits are used to fit the data in the Nyquist plot. The different impedance responses can be assigned to certain electric elements like resistors or capacities. An ideal resistor for example gives a line on the real (Z_{Re}) axis (see equation 2.22), an ideal capacitor gives a line on the imaginary (Z_{Im}) axis. Thus, an ideal RC-feature brings a perfect semicircle.
As the capacitance often don't behave perfectly, it is common to use a constant phase element (CPE) instead of a capacitance when fitting the data. The impedance of a CPE is given in equation 2.25. Q is the CPE parameter, n expresses the imperfection. If n = 1 it corresponds to a ideal capacitance (Q $\rightarrow$ C). In equation 2.26 the calculation of the capacitance of a CPE is shown.

$$Z_{CPE} = \frac{1}{(i\omega)^n Q} \tag{2.25}$$

$$C = (R^{1-n} \cdot Q)^{\frac{1}{n}} \tag{2.26}$$

Dependent on the measured impedance spectrum, it is easy or hard to gain knowledge out of the fitted data [45] [46].

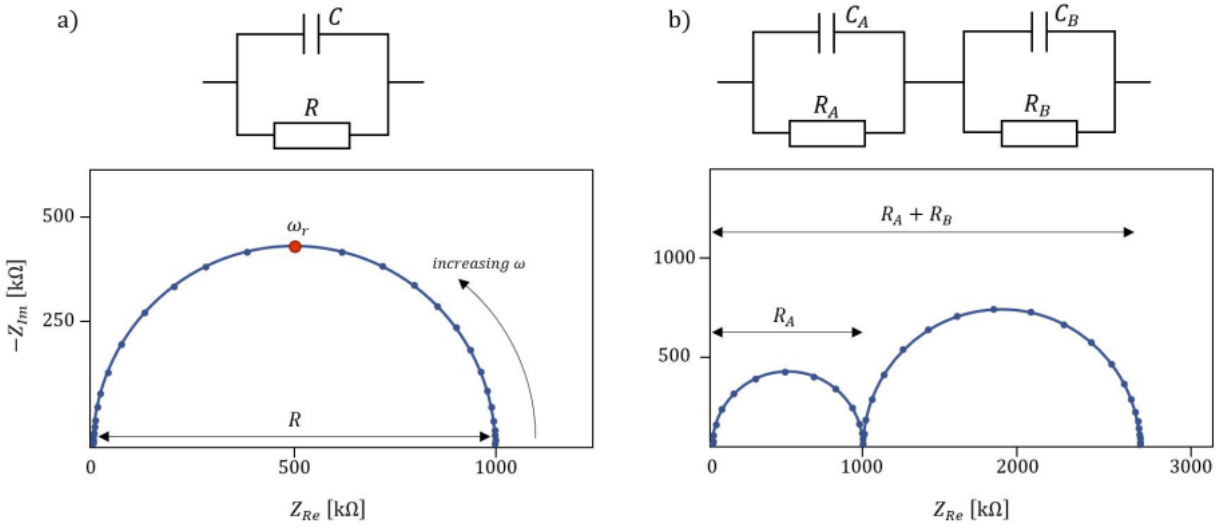

Figure 2.9: Example of two Nyquist plots and the corresponding equivalent circuit for a) a RC feature and b) two RC features in series connection [17].

3 Experimental

In this thesis, the preparation and investigation of STO based thin film high temperature solar cells was the main focus. In sum, 31 samples were prepared by pulsed laser deposition. They are named “PK001 - PK031”. The samples PK001-PK018, PK021-PK023, PK026-PK028 and PK031 are all STO thin film based solar cell samples (depicted in figure 3.6 on the left). Samples PK019, PK020, PK024 and PK025 are STO single crystal based solar cell samples (depicted in figure 3.6 on the right). Samples PK029 and PK030 were prepared for mass spectrometry (LASIL-ICP-MS) measurements. In this chapter, the preparation method, parameters or parameter changes, respectively, as well as the specifications of the different samples are explained. A list of the prepared samples as well as the preparation date, the used fluence, the thin film thicknesses and the deposition rate is given in table 4. The used laser energy, set on the laser terminal and in the chamber as well as the laser voltage are given in table 5. Furthermore, the measurement setup for EIS, voltage and current measurements is described. Also, externally conducted analysis methods and their used parameter sets are described.

3.1 Sample preparation

All samples were prepared by pulsed laser deposition. The setup used was the "new PLD" at the Institute of Chemical Technologies and Analytics, Faculty of Technical Chemistry, TU Vienna. It uses a Kr/F excimer laser Lambda COMPex Pro 201F with a wavelength of 248 nm. The laser path (3) can be changed by a mirror, leading one time to the "new PLD" setup or to the "old PLD" setup. Then, the laser is deflected another time, leading into the vacuum chamber (7). At the entry into the chamber, an aperture is mounted (1), to control the incoming laser pulse. To evacuate the vacuum chamber, first the coarse pump (12) is activated, followed by opening the bypass valve (5). After reaching a pressure of 10^{-2} mbar, the bypass valve can be shut again and the main vacuum valve (11) as well as the N_2 valve (16) can be opened. If the turbo pump (15) is activated and ready, the slide valve (14) can be opened. In the following, the turbo pump evacuates the vacuum chamber down to 10^{-5} mbar. To break the vacuum, the ventilation valve (4) can be opened, here it is important to close all other valves upfront. Pictures of the setup with description are depicted in figure 3.1 and figure 3.2.
A predefined parameter set was specified, leading to the used “standard” parameters for the PLD process. The parameters are summed up in table 1 for the different target materials. The repetition rate was changed for different targets between 5 Hz and 10 Hz (see table 1). The distance between the target and the sample inside the chamber is around 6 cm. Variations by a few mm, for the LSC and the LSCr targets couldn’t be avoided, as they were already thin and therefore couldn’t be installed plane into the target holder. For the STO targets though, the distance was always around 6 cm.

Table 1: Standard parameters used for the PLD process. The term STO includes every uncompensated as well as any Sr overcompensated STO target. The parameters used, are empirical values obtained during former experiments with this specific deposition setup [19, 22, 33].

Material	Heating Power [%]	Oxygen partial pressure [$mbar_{O_2}$]	Frequency [Hz]	Distance target - sample [cm]
LSC	35 ($\sim 360°C$)	4×10^{-2}	5	~ 6
STO	65 ($\sim 590°C$)	1.5×10^{-1}	10	6
LSCr	65 ($\sim 635°C$)	1.5×10^{-2}	5	~ 6

Before starting the preparation of a sample, the laser energy was always measured, to keep track of possible energy losses due to changed laser gas pressure, possible mirror displacements or contaminations in the beam path of the laser. Additionally, the laser energy is necessary for calculating the laser fluence on the target, which is determined by measuring the laser spot area of one laser pulse (figure 3.3 left) on the target and the laser energy inside the vacuum chamber. The fluence is a rather important reference value, as the ablation of

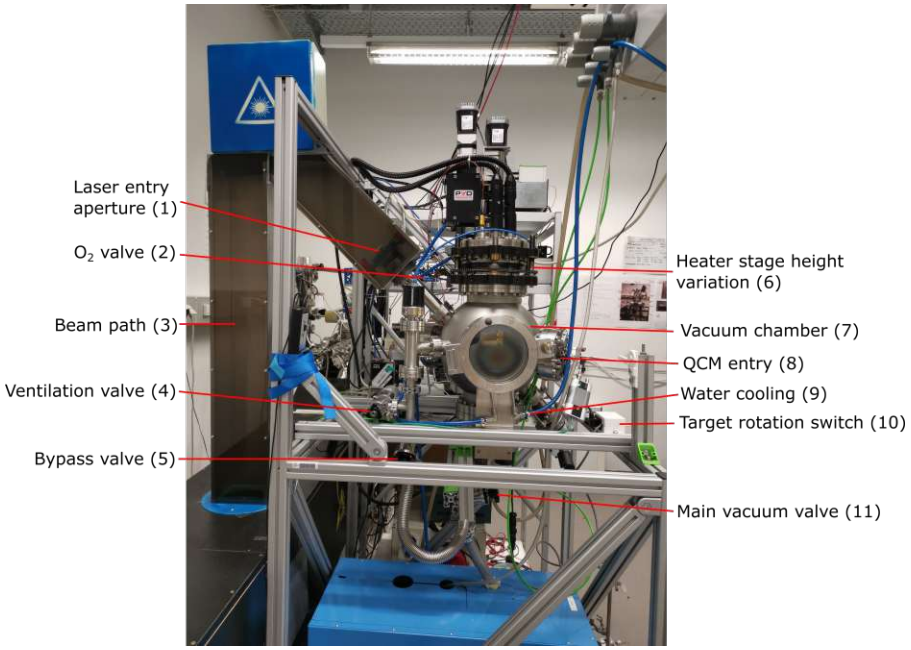

Figure 3.1: Front view of the PLD setup used for this work. On the left, the beam path (3) of the laser can be seen, which is deflected two times leading into the vacuum chamber (7). The ventilation valve (4) is used to break the vacuum inside the chamber, the bypass valve (5) and the main vacuum valve (11) are used to create vacuum. The quartz crystal micro-balance (QCM) can be entered through the QCM entry (8). The water cooling (9) is used to cool the window and the turbo pump (15). The heater stage, where also the sample holder is installed, can be moved upwards to use for example the QCM.

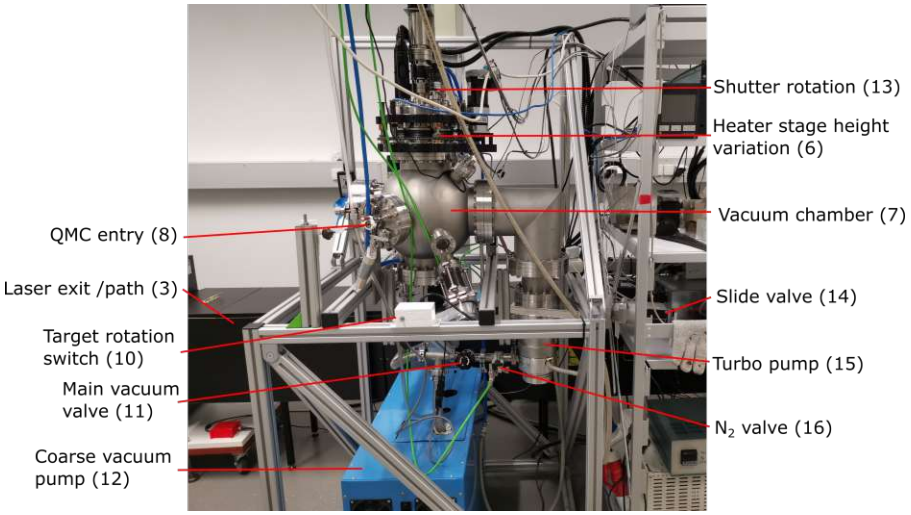

Figure 3.2: Side view of the PLD setup used for this work. At the back, the laser exit or path (3), respectively, can be seen. Down front, the coarse vacuum pump (12) is visible, which is used to pre-evacuate the chamber. At the top, the shutter rotator (13) can be spotted.

the target material strongly depends on it. The measured laser energies are listed in table 5. The fluence values used for the different depositions are listed in table 4.
The target used for measuring the spot size is a STO target with 10% Sr excess. It is used because of its white color, giving a good contrast for the area measurement. An example is depicted in figure 3.3 on the left. The area of the laser spot is measured by enlarging it with a microscope and using a program which allows you to

mark the edge of the visible spot and then calculates the area. An image of a measured spotsize is shown in figure 3.3 on the right.

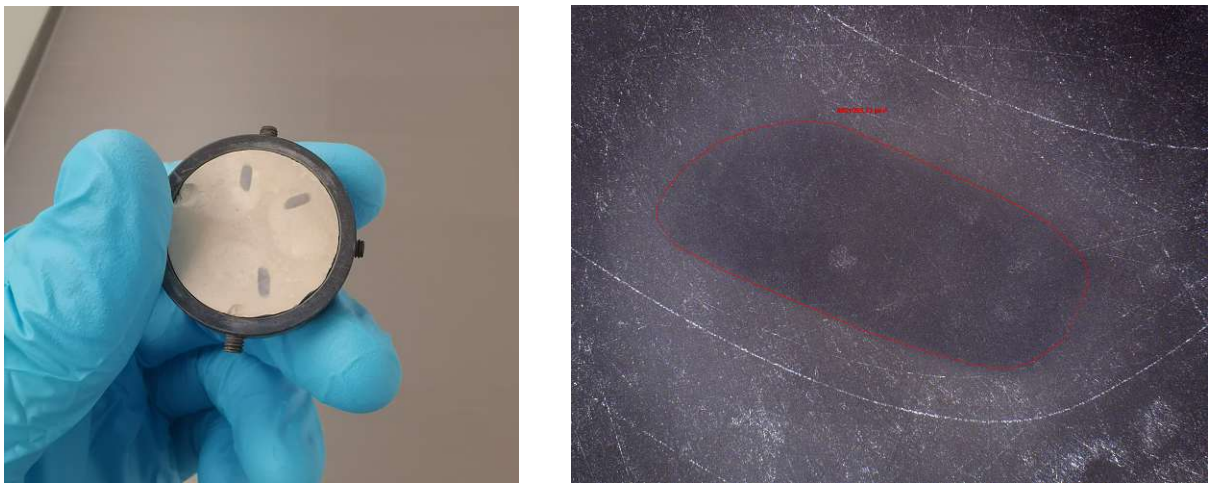

Figure 3.3: Left: Picture of the 10% Sr excess target with three laser spots on it. Right: Microscope image of the measured spot area.

After measuring the fluence, a STO single crystal [1 0 0], acting as the substrate for the thin films, is put into the sample holder and then placed in the PLD. Subsequently, the chamber is evacuated down to a pressure of $9{\cdot}10^{-5}$ mbar. After the evacuation, a certain oxygen partial pressure, depending on the target material used, is set by regulating the pressure with an O_2 inlet flow (2).
Before the deposition process, the single crystal was always annealed for about 45 min to 60 min at a heating power of 80% and a pressure of $4{\cdot}10^{-2}$ mbar. The annealing process is intended to release surface tension in the substrate material. After the annealing process, the temperature as well as the O_2-partial pressure is set to the respective values for the target material given in table 1.
Prior to the deposition and heating process, the deposition rate is determined with a quartz balance scale or quartz crystal micro-balance (QCM). The quartz balance scale is positioned at the same spot as the substrate/sample during the deposition process. One can calculate the deposition rate by using a certain amount of laser pulses (n_p) to deposit material onto the quartz crystal. There, the ablated material changes the vibration frequency of the quartz. From the change of the frequency the deposition rate can be calculated, leading to a value in nm film per laser pulse. The respective equation for calculating the change of the mass Δm (in [g]) is given in equation 3.1 and is called the Sauerbrey equation [47]. A is the piezoelectric active crystal area [cm^2], N_q is the frequency constant for AT-cut quartz crystal [$1.668{\cdot}10^{13}$ Hz Å], f_q is the start frequency [Hz], f_c is the stop frequency [Hz], Δf is the frequency change $f_c - f_q$ [Hz] and ρ_q is the density of the quartz [g/cm^3].

$$\frac{\Delta m}{A} = -\frac{N_q \rho_q}{f_q f_c} \Delta f \tag{3.1}$$

If the density of the deposited material ρ_m is known, the deposited thickness d can be calculated. The deposition rate can then be calculated by dividing the deposition thickness by the number of pulses used, shown in equation 3.2. The material densities of LSC, STO and LSCr are listed in table 2.

$$\frac{d}{n_p} = \frac{\Delta m}{A \rho_m} \tag{3.2}$$

Table 2: List of densities used for the calculation of the deposition rate.

	Density [g/cm^3]
ρ_{LSC}	6.50587488
ρ_{STO}	4.98448159
ρ_{LSCr}	6.49999764

A picture of the quartz scale measurement setup is depicted in figure 3.4. In this case, the deposition rate of LSC was determined before the annealing process to save time as the QCM measurement can't be carried out at elevated temperatures. The shutter is placed between the quartz scale and the sample to prevent an unwanted deposition onto the substrate/sample holder during the quartz scale measurement.

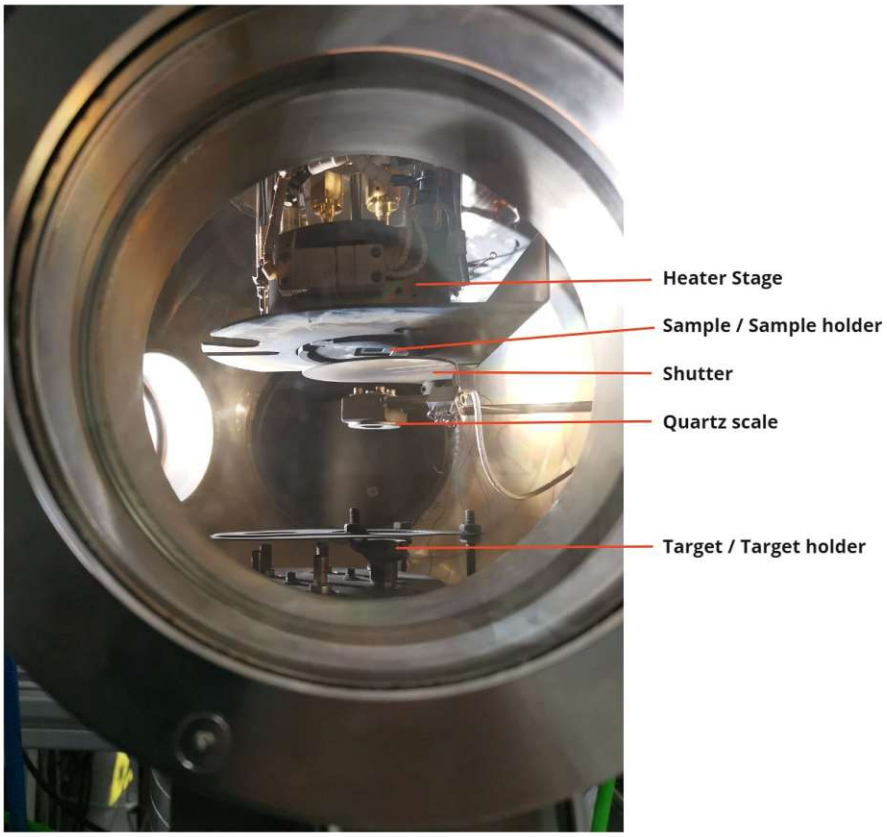

Figure 3.4: View inside the vacuum chamber of the PLD. The heater stage with the sample inside of it, covered with a shutter, is moved upwards, to bring the quartz scale to the actual position of the sample during deposition.

After measuring the deposition rate, the sample is heated to the corresponding deposition temperatures listed in table 1. After a constant temperature is reached, the target rotation is switched on. The target rotation is used to accomplish a homogeneous material ablation. Then, the deposition process is started, using the defined pulse rate (table 1) as well as the needed pulse count for the aimed thickness.
After the deposition process of each film, the sample is cooled down, using a 15 °C / 1 min cool down rate to reduce thermal stress. Then the sample is fetched from the vacuum chamber and, depending on the sample and the deposited film, either the sample is placed onto a shadow mask, the shadow mask is changed, or the sample is done. A picture of the sample holder and two shadow masks is given in figure 3.5 (a), c) and d)). For scale, one of the square holes of shadow mask c) in figure 3.5 is $3.3 \times 3.3\,\text{mm}^2$.

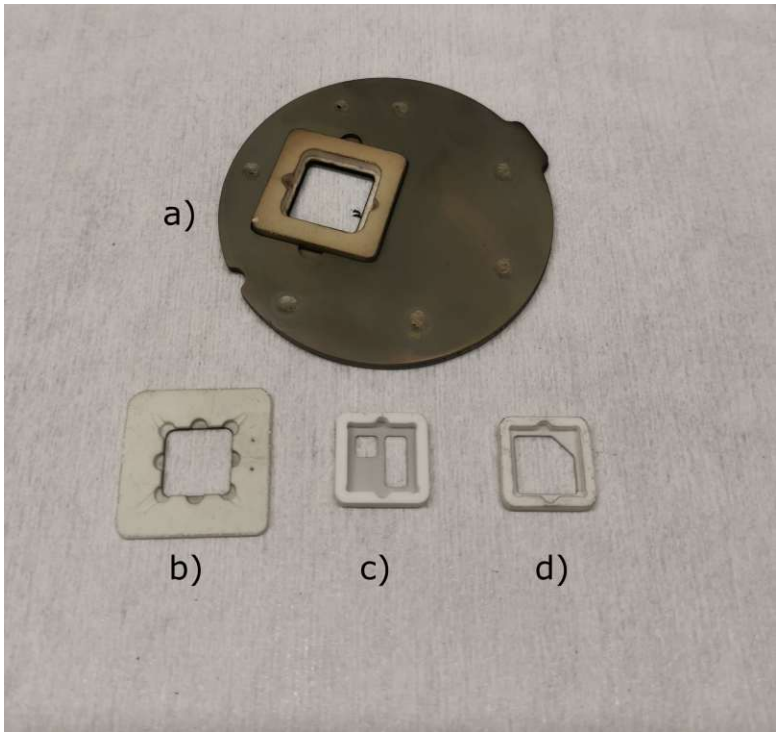

Figure 3.5: Picture of the a) sample holder, b) plane substrate holder used for annealing and deposition without shadow mask, c) shadow mask for a LSCr top electrode, d) shadow mask for STO thin films used for thin film solar cell samples. The shadow masks are made out of Al_2O_3.

Basically, two kinds of samples were prepared. The first and main kind of samples were the thin film solar cell samples, consisting of an undoped STO single crystal substrate, a deposited LSC thin film counter electrode, a deposited STO thin film, acting as an absorber layer and a deposited LSCr working electrode. The goal was to find a parameter set, which leads to reproducible samples, with high photovoltages. For the second kind of samples, STO thin films were deposited on an undoped STO single crystal, with a LSCr top electrode. Such samples were already prepared by Morgenbesser et al. [22], who investigated the effect of mainly Fe-doped STO thin films on top of a STO single crystal, to confirm the proposed defect chemical model described in his thesis. In the following subsections, the two kinds of samples will be discussed in more detail.
As substrates, mostly one side polished STO single crystals with a [1 0 0] orientation were used. The single crystals were produced by different companies. A list of the used STO single crystals and the corresponding samples is given in table 3.

Table 3: Used substrates with their corresponding supplier, orientation, surface texture, size and the sample code.

Substrate	Supplier	Orientation	Surface	Size [mm^3]	Sample code
STO	Crystal GmbH, Ger	[1 0 0]	one side polished	10 x 10 x 0.5	PK001-PK018
STO	CrysTec GmbH, Ger	[1 0 0]	one side polished	10 x 10 x 0.5	PK019-PK022
STO	MaTeck GmbH, Ger	[1 0 0]	one side polished	10 x 10 x 0.5	PK023-PK028
Sapphire	CrysTec GmbH	[0 0 0 1]	one side polished	5 x 5 x 0.5	PK029, PK030
STO	Crystal GmbH, Ger	[1 0 0]	both sides polished	10 x 10 x 0.5	PK031

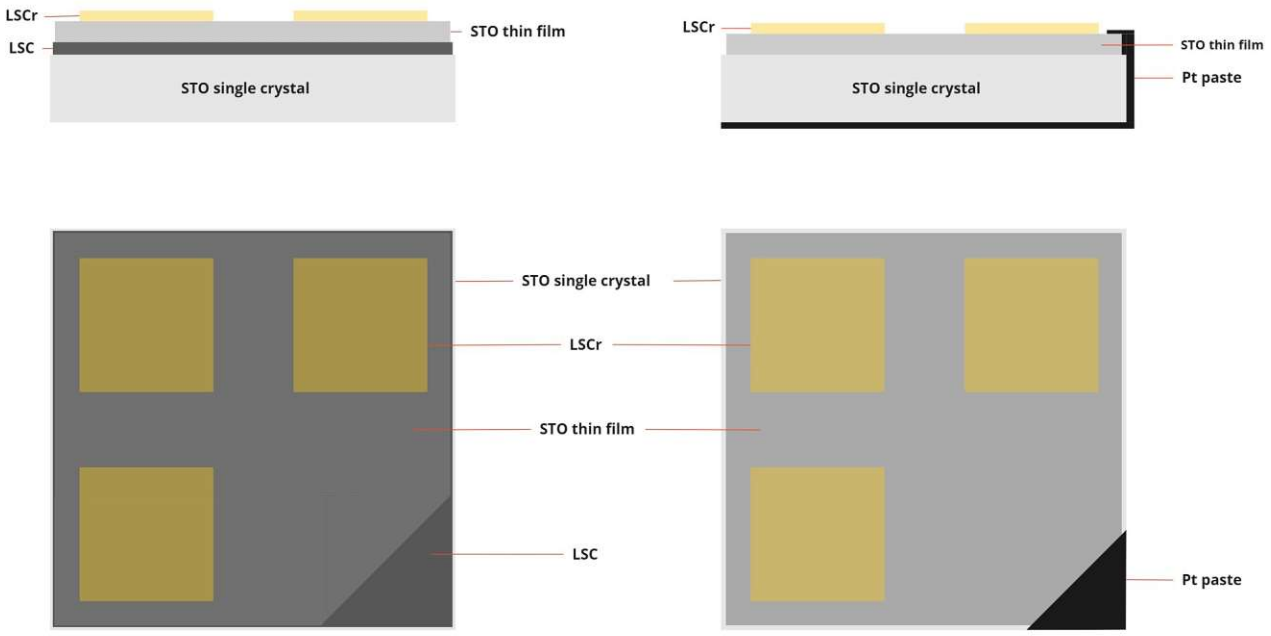

Figure 3.6: Scheme of the two sample types. The left sample represents the thin film solar cell structure, with three thin films deposited onto a STO single crystal. The right sample represents the STO single crystal based solar cell, where the STO thin film is deposited directly onto the substrate.

3.1.1 STO thin film solar cells

For the STO thin film solar cells, a "standard" set of parameters regarding the thickness, the geometry as well as the fluence were chosen. The basic structure includes a STO single crystal (table 3), a $(La_{0.6}Sr_{0.4})CoO_3$ (LSC) counter electrode, a $SrTiO_3$ (STO) thin film and a $(La_{0.9}Sr_{0.1})CrO_3$ (LSCr) working or top electrode. The geometry is depicted in figure 3.6 on the left, the standard parameters are listed in table 6. A sketch of the deposition procedure is depicted in figure 3.7. LSC for the counter electrode was chosen because of its high in-plane conductivity, which should lead to a negligible feature in the impedance spectrum. LSCr for the top electrode is chosen because of reported high photovoltages gained at hetero-junctions with STO single crystals [10] as well as its transparency and good absorbance properties when used as thin films, as a maximal amount of radiation should reach the STO film acting as the photo-absorber [33]. Also a nice growth on STO is reported [10]. Additional to standard parameter samples, changes regarding the geometry, the thin film thickness, the fluence, the deposition temperature as well as the amount of Sr overcompensation in the target were investigated. The geometry of the sample is changed by switching the Al_2O_3 shadow masks. Once, a "tower" shape was tried, i.e. using a shadow mask with three square holes (like usually used for the LSCr top electrodes) for the STO thin film deposition. The LSCr top electrodes were then deposited using a shadow mask with three smaller square holes on top of the STO "towers". This tower shape was done for sample PK006. For PK001, the tower shape was etched by ion beam etching after its initial characterisation. Additionally, the top electrodes were changed from three similar squares to one square and one bigger rectangle (see figure 3.5 c)). This change was done for the samples PK012, PK021, PK022, PK026-28, PK031. Most of the later produced samples were prepared with that electrode geometry, as the other shadow mask broke.

The thin film thickness was mainly varied for the STO thin film. Modified from the "standard" thickness, a significantly thicker and a significantly thinner film was deposited. Sample PK002 had a thicker film of about 1125 nm, sample PK003 a thinner film of about 450 nm. Here one has to say, that the thicknesses can always vary, as the determination of the deposition rate by QCM can differ from the actual deposition rate. All given

Table 4: List of the samples with their corresponding deposition date, fluence, film thicknesses and deposition rate, if measured. The layer sequence is specified in relation to the used target material. For all samples with given film thicknesses but no given deposition rate, the deposition rate was presumed from previous deposition processes (PK001-PK010, PK012-PK014).

Sample code	Date	Layer sequence	Fluence [J/cm^2]	Film thickness [nm]			Deposition rate [nm/pulse]		
				STO	LSC	LSCr	STO	LSC	LSCr
PK001	21.04.22	LSC, STO 7%, LSCr	1.10	843	247	168	0.0187	0.0275	0.0187
PK002	25.04.22	LSC, STO 7%, LSCr	1.10	1125	247	168	-	-	-
PK003	02.05.22	LSC, STO 7%, LSCr	1.04	450	247	168	-	-	-
PK004	05.05.22	LSC, STO 7%, LSCr	1.01	843	247	168	-	-	-
PK005	16.05.22	LSC, STO 7%, LSCr	1.01	843	247	168	-	-	-
PK006	17.05.22	LSC, STO 7%, LSCr	1.01	843	247	168	-	-	-
PK007	30.05.22	LSC, STO 7%, LSCr	1.01	843	247	50	-	-	-
PK008	31.05.22	LSC, STO 10%, LSCr	1.01	843	247	168	-	-	-
PK009	01.06.22	LSC, STO 0%, LSCr	1.01	843	247	168	-	-	-
PK010	20.06.22	LSC, STO 7%, LSCr	0.99	843	247	168	-	-	-
PK011	21.06.22	LSC, STO 7%, LSCr	0.8	843	166	126	0.0155	0.0184	0.0140
PK012	30.06.22	LSC, STO 7%, LSCr	1.01	843	247	168	-	-	-
PK013	05.07.22	LSC, STO 7%, LSCr	1.00	843	247	168	-	-	-
PK014	07.07.22	LSC, STO 7%, LSCr	1.00	843	247	168	-	-	-
PK015	20.07.22	LSC, STO 7%, LSCr	1.20	843	247	168	0.0122	0.0142	0.0109
PK016	01.08.22	LSC, STO 7%, LSCr	1.00	843	247	168	0.0171	0.0199	0.0151
PK017	23.08.22	LSC, STO 7%, LSCr	1.10	843	247	168	0.0207	0.0256	0.0181
PK018	24.08.22	LSC, STO 7%, LSCr	1.00	840	247	150	0.0171	0.0262	0.0166
PK019	25.08.22	STO 0%, LSCr	1.00	300		150	0.0338		-
PK020	26.08.22	STO 0%, LSCr	1.01	843		150	0.0282		0.0205
PK021	14.10.22	LSC, STO 7%, LSCr	1.13	840	217	151	0.0260	0.0241	0.0168
PK022	25.10.22	LSC, STO 15%, LSCr	0.99	711	247	105	0.0129	0.0199	0.0117
PK023	27.10.22	LSC, STO 7%, LSCr	1.06	730	200	137	0.0163	0.0223	0.0153
PK024	14.11.22	STO 7%, LSCr	1.01	355		110	0.0187		-
PK025	16.11.22	STO 15%, LSCr	1.03	350		110	0.0194		0.0115
PK026	17.11.22	LSC, STO 15%, LSCr	1.01	773	100	95	0.0172	0.0149	0.0107
PK027	18.11.22	LSC, STO 15%, LSCr	1.13	840	140	122	0.0199	0.0156	0.0136
PK028	22.11.22	LSC, STO 15%, LSCr	1.03	843	170	110	0.0197	0.0190	0.0122
PK029	14.11.22	STO 15%	1.01	340			0.0149		
PK030	14.11.22	STO 7%	1.01	355			0.0187		
PK031	23.11.22	LSC, STO 15%, LSCr	1.03	843	170	122	0.0196	0.0190	0.0136

values are therefore just estimated by the QCM measurement.
The fluence was deliberately changed for sample PK011 to a value of about 0.8 J/cm^2, and for sample PK015 to 1.2 J/cm^2. Sample PK001, PK002, PK021 and PK027 were deposited with about 1.1 J/cm^2. Here also one has to say, that there can be changes to the actual fluence, as the determination of the fluence is quite hard. Also the laser energy is not perfectly constant over time, which needs to be kept in mind, especially for thicker films. The deposition temperature for the STO thin film was once changed to a heating power of 80 %. The Sr overcompensation was changed from the standard 7 % to a stoichiometric target (STO 0 %) for PK009, to a 10 % overcompensation for PK008 and to 15 % Sr excess in the target for the samples PK022, PK026-PK028, and PK031. In table 4 all samples with their corresponding parameters are listed.

Table 5: List of the samples with their corresponding set laser energies, as well as measured energies inside the vacuum chamber at 400 mJ and with regarding set deposition laser energies.

Sample code	Date	Laser Energy [mJ]			Laser voltage [kV]
		in chamber at 400 mJ set	set for deposition	in chamber for deposition	
PK001	21.04.2022	101.4	260	72	18.5
PK002	25.04.2022	-	260	70	18.6
PK003	02.05.2022	93.3	260	65	20.3
PK004	05.05.2022	100.6	260	72.2	18.5
PK005	16.05.2022	90.4	270	65.2	19.2
PK006	17.05.2022	-	270	-	19.9
PK007	30.05.2022	90.9	260	67.3	18.6
PK008	31.05.2022	-	260	-	18.6
PK009	01.06.2022	-	260	-	18.9
PK010	20.06.2022	83.6	340	70.9	22.2
PK011	21.06.2022	81.5	260	56.2	20.0
PK012	30.06.2022	80.0	350	72.3	20.4
PK013	05.07.2022	-	320	-	20.4
PK014	07.07.2022	82.2	260	61.1	20.4
PK015	20.07.2022	66.9	260	46.2	19
PK016	01.08.2022	66.4	440	70.5	23.3
PK017	23.08.2022	120.0	260	87.3	18.7
PK018	24.08.2022	116.0	260	84.4	18.8
PK019	25.08.2022	111.4	280	84.4	18.8
PK020	26.08.2022	113.2	300	88.8	20.5
PK021	14.10.2022	97.3	340	88.4	20.5
PK022	25.10.2022	98.6	300	77	21.7
PK023	27.10.2022	109.6	300	90.2	19.4
PK024	14.11.2022	95.6	340	84.9	20.5
PK025	16.11.2022	92.0	370	86.4	21.8
PK026	17.11.2022	93.1	370	85.9	22.2
PK027	18.11.2022	94.4	370	87.1	23.1
PK028	22.11.2022	97.8	320	84.1	19.8
PK029	14.11.2022	95.6	340	84.9	20.5
PK030	14.11.2022	95.6	340	84.9	20.5
PK031	23.11.2022	97.7	340	87.8	20.4

Table 6: Standard values used for thin film solar cells.

Material	approx. film thickness [nm]	corresponding laser pulses	Fluence [J/cm^2]
LSC	$\sim$ 250	$\sim$ 9000	$\sim$ 1
STO	$\sim$ 840	$\sim$ 45000	$\sim$ 1
LSCr	$\sim$ 170	$\sim$ 9000	$\sim$ 1

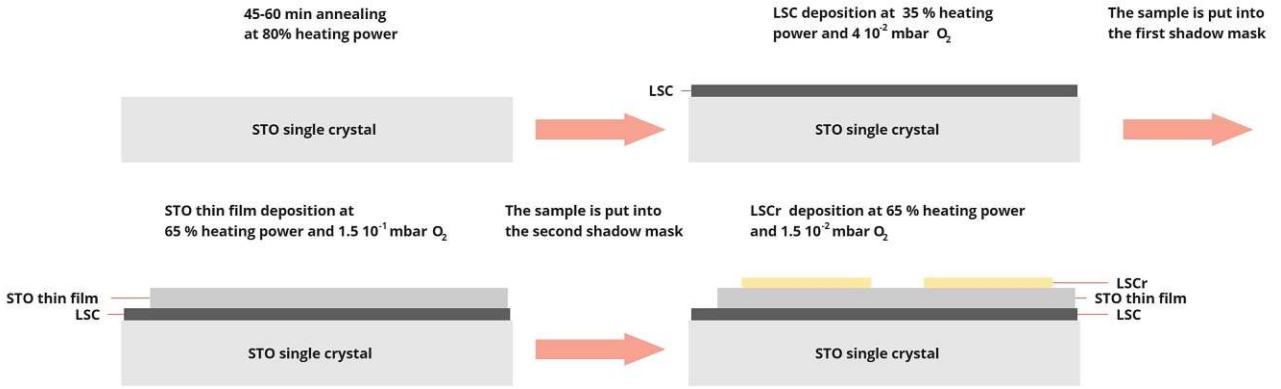

Figure 3.7: Deposition procedure of a standard STO thin film based solar cell sample.

3.1.2 STO single crystal based solar cells

For the STO single crystal based solar cell measurements, the same PLD parameters as for the STO thin film based solar cells (see table 1) were used. These samples consisted of a STO single crystal acting as the substrate, a STO thin film and a LSCr top electrode. Pt paste was used as a counter electrode. It was brushed onto the bottom area of the STO single crystal and around the corner, as sketched in figure 3.6 on the right. This had to be done due to the contact requirements of the measuring setup. For the STO film, no shadow mask was used, for the LSCr film, either the shadow mask with three squares or the one depicted in figure 3.5 was used.
In sum, four STO single crystal based solar cell samples were prepared. The STO thin film thickness as well as the Sr overcompensation of the STO target was changed. Sample PK019 and PK020 were both prepared with a stoichiometric STO target (STO 0 %) but differ in their STO thin film thickness. PK019 has a STO thin film thickness of about 300 nm, PK020 a STO thin film thickness of around 840 nm. Sample PK029 is deposited with a 15 % overcompensated STO target, PK030 with a 7 % overcompensated STO target.

3.2 Target preparation

During the experimental work, a non-stoichiometric STO target with a 15% Sr overcompensation had to be prepared. The target was prepared by a mixed oxide route. First, the two powders $SrCO_3$ (99.995 %, Sigma Aldrich, Germany) and TiO_2 (99.995 %, Alfa Aesar, USA) were weighted into the right non-stoichiometric sub parts. Then they were mixed and crushed in an agate mortar and calcinated at 1000 °C for two hours under ambient air conditions. After the calcination, the powder was crushed again. The powder was then pressed into the target form in a cold isostatic press for about 10 min and sintered at 1500 °C for ten hours. After the sintering process, the target was brought into the appropriate shape for the target holder by sanding. A XRD measurement of some leftover powder was conducted to get information on the composition and structure of the material.

3.3 Measurement setup

For the impedance, voltage and current measurements a micro-contact setup with asymmetric heating was used. The whole setup is placed onto a vibration damping table. A picture of the setup is depicted in figure 3.8 and a sketch of the inside of the vacuum chamber is shown in figure 3.9. The samples were placed onto a hot stage inside the vacuum chamber. Between the sample and the heater, an electrical grounded Pt shielding plate is placed to prevent influences of the hot stage during EIS measurements. This leads to a minimisation of stray fields, but also to heating temperature decreases compared to the set temperature [48].
The samples were contacted with two Pt/Ir needles. Both needles are mounted onto a gold coated steel tip of an moveable micro manipulator (piezo actuators, Agilis Newport, USA). The contacting was performed with the use of a microscope (Mitutoyo, Japan) and micro-manipulators, which can be precisely operated by a software. All measurements were generally carried out under ambient air. For some samples, synthetic air conditions (20 % O_2, 80 % N_2) were generated. The synthetic air was mixed from O_2 and N_2 via two mass flow controllers (see figure 3.8). The air displacement method was used for calibration.
For all samples, every deposited top electrode was contacted and will be furthermore indicated as down left (dl), up left (ul) and up right (ur), as depicted in figure 3.9. If a different top electrode geometry is used, e.g. the one with just two electrodes, they are distinguished in the same manner. If the bigger electrode is contacted at different spots, it is also referred to as (dl) and (ul).
The UV light source used for photovoltage and photocurrent measurements had a wavelength of 365 nm and an intensity of 0.24 W/cm^2 and was placed in the window above the sample (see figures 3.8 and 3.9). The light source can be switched on and off with the control port. Because of the encapsuled construction of the light source, it creates a dark situation when the UV lamp is turned off.

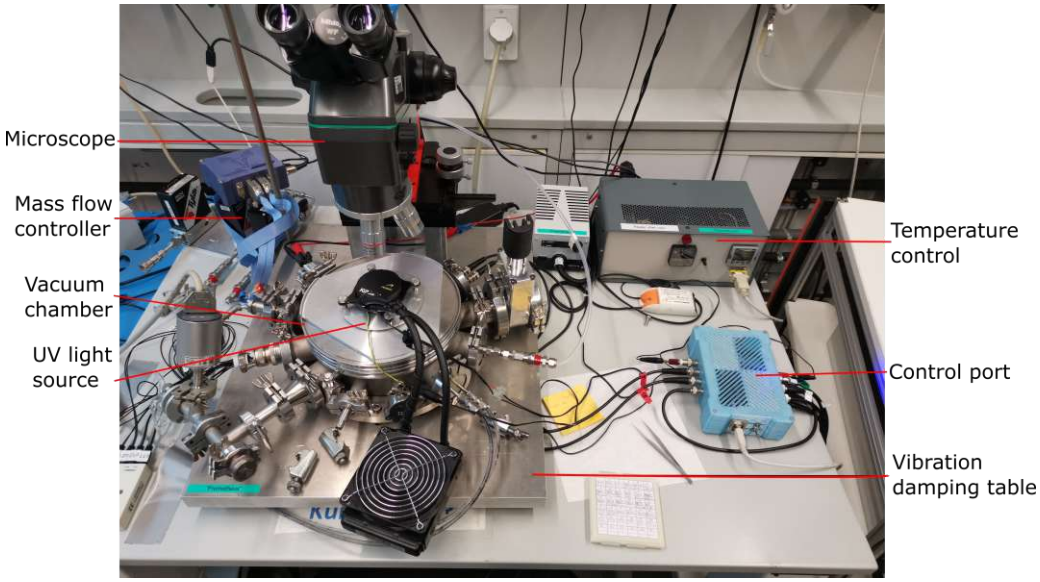

Figure 3.8: Picture of the measurement setup used for impedance, voltage and current measurements.

3.3.1 Impedance measurements

All electrochemical impedance measurements were carried out with the above described micro-contact setup. The impedance measurements themselves are carried out with a Alpha-A High Performance Frequency Analyser (Novocontrol Technologies GmbH & Co. KG, Germany). For every sample, five temperatures were measured. The set temperatures were 250 °C, 300 °C, 350 °C, 400 °C, 450 °C. The actual sample temperature is ca. 50 - 70 °C cooler than the set temperature because of the shielding plate and the fact that an inhomoge-

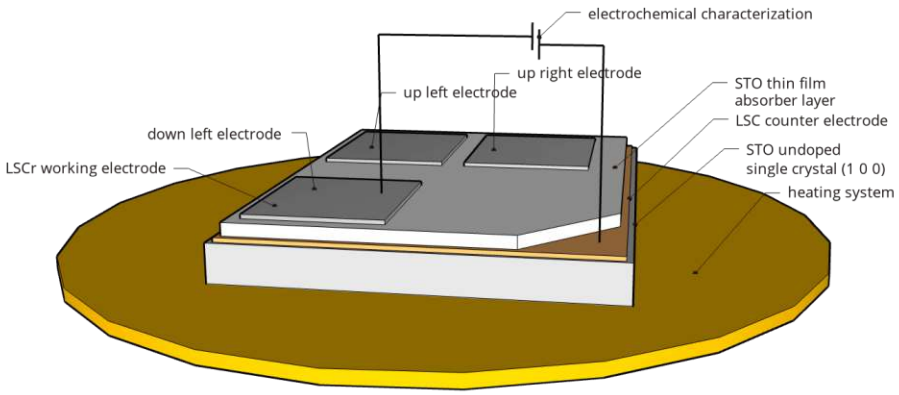

Figure 3.9: Sketch of the measurement setup inside the vacuum chamber. The sample is contacted on two points with Pt/Ir needles.

neous heating system is used. The applied AC rms amplitude for measurements was 100 mV. For single crystal based thin film samples, the applied AC rms amplitude was sometimes changed to 200 mV. The frequency ranged used for every impedance measurement was between 10^6 Hz and 10^{-1} Hz, with ten points per decade. For every set temperature three impedance spectra were measured, to verify if thermal drifts and/or equilibrium adjustments need to be considered. The measurements were carried out in darkness and under UV light illumination.
For some samples that generated photo-voltages under UV light, additional impedance measurements with applied bias voltages were measured. The maximal applied bias voltage corresponded to the generated photovoltage under UV light irradiation and is thus different for each sample and in a range from 0 to max. 1 V. The bias voltage is applied by a Alpha-A High Performance Frequency Analyser with an Electrochemical Test Station POT/GAL 30 V / 2 A (Novocontrol Technologies GmbH & Co. KG, Germany), and was measured in cycles, starting from the maximum applied bias voltage, using 50 mV steps. Through these DC measurements, the power of the sample cell can be calculated and plotted, gaining power-voltage or power-current curves.
Besides the standard measurements under ambient air conditions, also impedance measurements under synthetic air conditions were performed. This change of atmosphere was investigated to exclude possible negative effects on the cell performance.

3.3.2 Voltage measurements under UV light

The photovoltage measurements carried out at the described micro-contact setup (figure 3.8) were performed with a Keithley Dmm2000 (Keithley Instruments, USA) under ambient air condition. The generated voltage was measured in open circuit mode, thus giving open circuit voltage values (OCV). The photovoltage measurements were mainly performed at 300°C set.
The voltage measurement as well as the on and off switching of the UV light source were controlled via trigger control ports based on an Aduino. The standard procedure for the voltage measurements was started by switching on the UV light and measuring the impedance while illuminating the sample. Subsequently, the UV-on-off cycles were performed. These cycles were short for testing the samples general photo-response or longer for more detailed investigations on long-term stability and possible degradation processes. The short measurement was most of the time structured as followed: 20 min illumination, 20 minutes dark, 20 min illumination, 10 min dark. The long-term measurements were most of the time carried out overnight, or even over weekends,

leading to illumination times of up to four hours or more. For some samples, OCV measurements were also performed in synthetic air conditions, with the same procedures as described above.

3.3.3 Current measurements under UV light

Photo-current measurements carried out at the described micro-contact setup (figure 3.8) were performed with a Keithley Dmm2000 (Keithley Instruments, USA) under ambient air conditions. The current was measured in short circuit mode, generally at temperatures of 300 °C set. The current measurements were also controlled by the trigger ports, as it was already described for the voltage measurements. Additionally, synthetic air was sometimes used as measuring environment. Both the short and long UV light cycles were performed identically to the OCV measurements. Also, longer continuous illuminations were performed, especially for single crystal based solar cell samples, to check and reproduce results regarding the self-enhancement effect described by Morgenbesser et al. [33].
Current measurements were only performed for samples with a previously measured significant amount of photovoltage, for obvious reasons.

3.4 Transmission electron microscopy / Scanning electron microscopy

To investigate the growth and nanostructure of a sample, an electron transparent lamella of a few μm was prepared via a standard lift-out technique using a focused ion beam/scanning electron microscopy (FIB/SEM) system (Scios 2 DualBeam, Thermo Fisher Scientific, Germany). The system operates with a Ga-ion beam at 30 kV acceleration voltage. The final low voltage cleaning of the lamella was conducted at 5 and 2 kV. The bright field transmission electron microscopy (BF-TEM) was performed on a 200 kV FEI TECNAI F20. Before the FIB/SEM preparation of the lamella, a thin platin film was sputtered onto the sample for stability reasons. Then, the lamella is cut out of the sample, put onto a lamella holder and further prepared for the BF-TEM by thinning it out (cleaning). The two pictures in figure 3.10 show the two process parts of the preparation. The lamella at this point is about 30 μm long and 10 μm high. After the cleaning process, the lamella, which is placed onto the lamella holder, can be put into the BF-TEM.

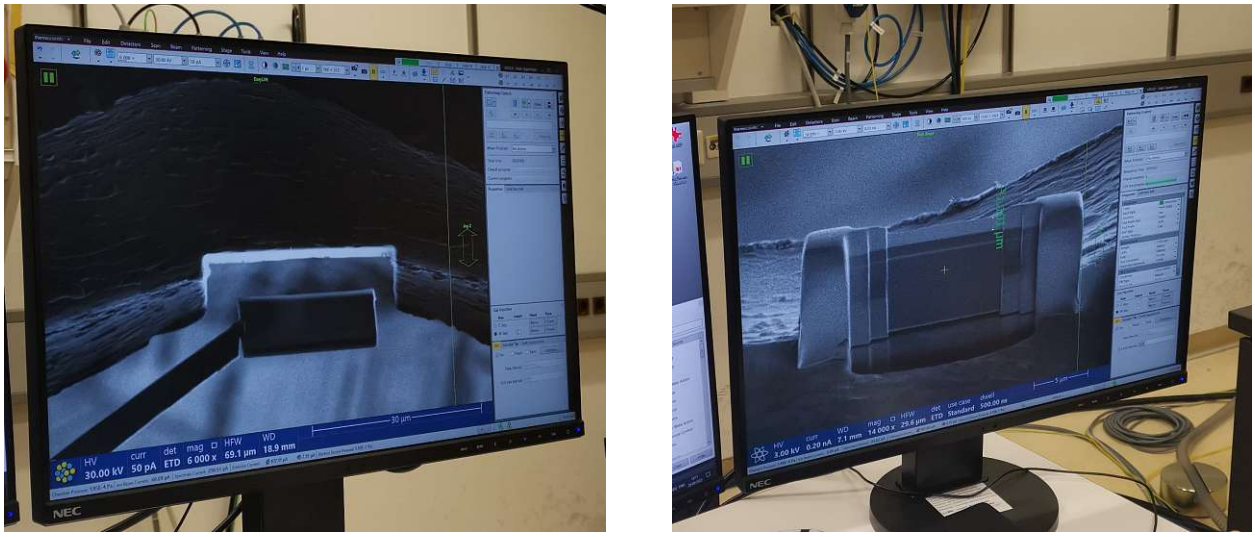

Figure 3.10: Pictures made during the preparation process of the lamella with a FIB/SEM system. The left picture shows the process, where the cut out lamella is placed onto a lamella holder, which is afterwards used for TEM. The right picture shows the process, where the lamella is cut thinner (cleaned) for the subsequent TEM measurement. Here, the layers of the sample can already be seen.

Additionally, TEM and SEM analysis were done for samples PK004 and PK013 at the Forschungszentrum Jülich, Institute for Energy and Climate Research, Materials Synthesis and Processing (IEK-1) as well as the Ernst Ruska-Centre for Microscopy and Spectroscopy with Electrons, Materials Science and Technology (ER-C-2) by Dylan Jennings. The TEM used was a FEI Tecnai G2 F20, the SEM used a FEI Helios NanoLab 460F1 FIB-SEM. Further information about the two used setups can be found in [49, 50]. To further investigate the results, high-angle annular dark-field (HAADF) STEM Energy-Dispersive X-Ray Spectroscopy (EDS) was done.

3.5 Online-LASIL-ICP-MS, LA-ICP-MS

Online Laser Ablation of Solids in Liquids-Inductively Coupled Plasma-Mass Spectrometry (Online-LASIL-ICP-MS) is used to characterise the elemental composition of the deposited thin films structure. Element depending stoichiometry measurements were carried out with this method.
The basic measurement of online-LASIL-ICP-MS works as followed: First, a sample is ablated by a pulsed laser (266 nm). The generated nanoparticles are then transported into an ICP-MS (iCAP Q ICP-MS, Thermo Scientific) by a carrier solution. The carrier solution used is water. The flow used for the water is $\sim$0.3 ml/min. The make up solution consists of 6% HNO_3 / 0.6% HF, with a flow of $\sim$0.1 ml/min.
The laser parameters used for the different samples are listed in table 7. Sketches of the setup and function principle for better understanding are depicted in figure 3.11. For PK029 and PK030 the ratio between Ti and Sr was measured to see whether the thin films deposited are stoichiometric or off stoichiometric.

The depth profiles for samples PK004, PK009 and PK0012 were done with Laser Ablation-Inductively Coupled Plasma-Mass Spectrometry (LA-ICP-MS). LA-ICP-MS is based on a focused pulsed laser hitting a sample surface. The laser pulse removes material from the sample and forms an aerosol of particles. The generated particles are then washed out and transported by a stream of He gas to an ICP-MS instrument. In the ICP, the ablated particles are vaporised, atomised and then ionised. The generated ions are fed into a high vacuum system and the ion beam is focused. The ions are separated according to their mass-to-charge ratio and then detected by a mass analyser. The used parameters are listed in table 7. The carrier solution was He with a used flow of 800 ml/min.
Both, Online-LASIL-ICP-MS and LA-ICP-MS, were done by the research group "Inorganic Trace Analysis" at the TU Vienna (E164-01-2).

Table 7: Laser parameters used for the online-LASIL- and LA-ICP-MS analysis.

Sample code	Laser Parameter			
	Fluence [J/cm^2]	Spot size [μm^2]	Repetition rate [Hz]	Scan speed [mm/s]
online-LASIL-ICP-MS				
PK004, PK009, PK012	0.6	100	10	0.2
PK029, PK030	3.8	100	10	0.2
LA-ICP-MS				
PK004, PK009, PK012	1.8	400	20	0.8

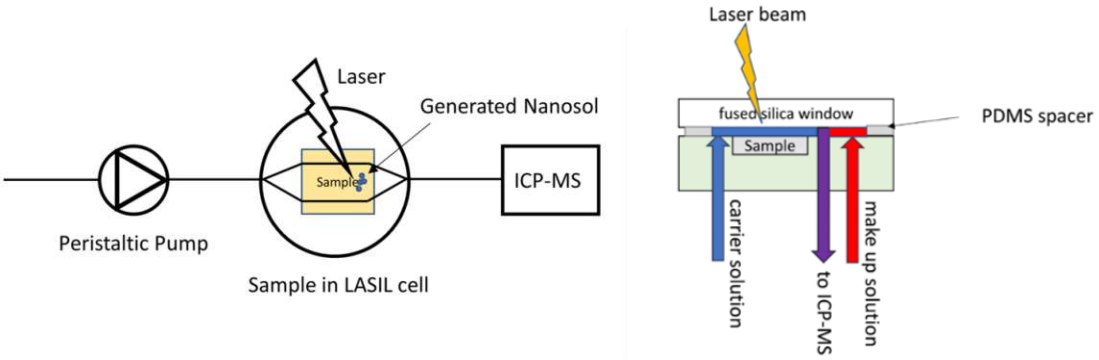

Figure 3.11: On the left: Sketch of the online-LASIL-ICP-MS setup. On the right: Sketch of the LASIL cell, with shown carrier solution flow and make up solution flow.

4 Results and Discussion of STO thin film based solar cells

First, some information on the colour and sign code of the shown impedance data is given. All temperatures shown in the figures are set temperatures and given in [°C]. The colours are regarded to the used temperature (e.g. yellow). The electrode measured on is marked with a certain sign, namely a circle for the up left (ul) electrode (●), a triangle for the up right (ur) electrode (▲) and a square for the down left (dl) electrode (■). For measurements, where for example the impedance is measured at the same electrode and at the same set temperature, but with UV light on or off, a dark version of the colour code is used for the UV light off version (e.g. dark yellow) and a brighter one for the UV light on version (e.g. bright yellow).
For the shown voltage and current measurement, the same sign code is used, though a different colour code is employed, as the signs can not be seen too well because of the amount of measured points. Therefore, additionally, the up left electrode is marked with the colour light blue, the up right electrode with the colour light red and the down left electrode with light green. Measurements with synthetic air have a lighter form of the corresponding colour.

Coming from achievements regarding STO single crystal solar cell applications, the question arose, if similar accomplishments could be made with STO thin films instead of single crystals as absorbing layer. As there was not much information about the exact function and behaviour of STO thin film based solid oxide solar cells and whether they can provide sufficient photovoltage at all, we started with a defined “standard” geometry. The geometry had an open LSC face, which was contacted as the counter electrode and three LSCr top electrodes, which were contacted as the working electrode. Between those two electrodes, a STO thin film - as the light absorber - is deposited (see figure 3.6). The STO target we started with had a 7% Sr overcompensation. This is due to the aforementioned (see subsection 2.1.2) known Sr deficiency in deposited STO thin films found by Morgenbesser et al. [20] and the desired stoichiometric thin film. At the beginning of this work, the 7% target was assumed to result in stoichiometric thin films, as similar results were achieved by Morgenbesser et al. [19] for Fe doped STO 7% targets. Additionally, the mentioned standard parameters listed in table 6 were used at the beginning.

4.1 First sample series with little photovoltage response

First, we examined whether the standard parameters, which were based on experience values, yielded a satisfying result and whether certain changes could improve it.
Starting from the mentioned structure, geometry and parameter set, the STO thin film thickness is varied.
PK001 is deposited with an assumed thickness of ~ 840 nm, PK002 with a thickness of ~ 1100 nm and PK003 with a thickness of ~ 450 nm. For sample PK002, a different geometry was used by accident. The geometry used was a kind of "tower" shape, which is described in subsection 3.1. Here, it was assumed, that the different geometry isn’t changing the properties significantly. The geometry of the samples was dealt with again later. The thickness was determined by QCM measurements. They were performed before depositing the first sample PK001. For the preparation of the following samples, the same deposition rate was assumed, as the fluence was always set to ~ 1 J/cm^2. A visual observation of the first three samples showed nice looking STO thin films for all three samples. The only difference could be observed for the LSCr thin film for sample PK003. It seemed, that the LSCr thin film was not growing well on the thinner STO thin film. Pictures taken with a microscope are shown in figure 4.1.
Impedance measurements were carried out as described in subsection 3.3.1. For PK001, with a ~ 840 nm thin film, a few things were observed while looking at the impedance spectra. Firstly, the impedance gets smaller with increasing temperature, see figure 4.2 a), which is expected due to thermally activated processes. Secondly, the impedance spectra showed a high-frequency feature and a low frequency feature. Fitting the spectra with equivalent circuits brought no useful information, as no feature could be assigned to a certain layer or part of the sample’s structure. A change of the low frequency feature upon UV irradiation can be seen in figure 4.2

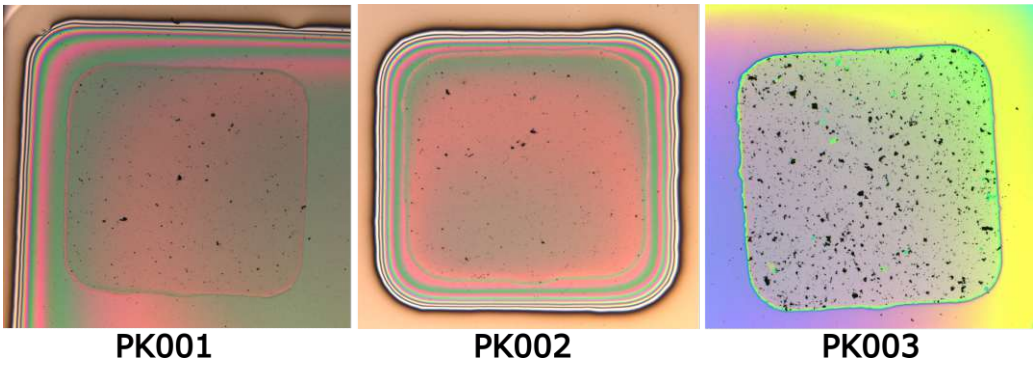

Figure 4.1: Optical observation of the first three deposited samples with varying STO thin film thicknesses. PK001 with a $\sim$ 840 nm thin film, PK002 with a $\sim$ 1100 nm thin film and PK003 with a $\sim$ 450 nm thin film.

c) and d). The impedance of the irradiated up right electrode interestingly grows noticeable, while it shrinks very little for the up left electrode. That could be an indication of a space charge zone. The high-frequency feature is without evidence assumed to be the counter electrode (LSC).
Additionally, an electrode dependence is observed, as depicted in figure 4.2 b). Both spectra were measured at 300°C but show a clear difference. Also, the reaction to UV light irradiation differs significantly.
For the sample PK002, with a $\sim$ 1100 nm thin film, no specific features were observed in the impedance measurements. In figure 4.3 an exemplary impedance spectrum for the up left electrode with UV light on and off is shown. No big difference can be observed. Other spectra for PK002 are not shown, and no further investigations were made.
PK003 showed equally little features. An exemplary impedance spectrum is shown in figure 4.4, measured at the up left and down left electrode at 300°C. Here, one can again observe different spectra for the two different electrodes. The impedance spectra for PK002 and PK003 were not further investigated because no clear semicircles or similar features were observed. The only notable correlation between PK001, PK002 and PK003 is a similar order of magnitude regarding the impedance.
A photovoltage was observed for sample PK001, while irradiating it with UV light. In figure 4.5, two measured irradiation cycles are shown for the up left and up right electrode. Notably, both electrodes show different photovoltages. For the up left electrode, voltages of around -93 mV were reached, for the up right one around -66 mV. In figure 4.6 two current measurement cycles are depicted, both measured on the up right electrode. On the left, a short irradiation cycle is shown (20 min UV on - 10 min UV off - 10 min UV on) reaching a short circuit current of around -2.44 $\cdot 10^{-6}$ A. On the right, a longer measurement cycle of around 50 hours is shown, with one UV off phase after one hour. The longer measurement showed a current decrease over time, reaching a steady state short circuit current of around -1.88 $\cdot 10^{-6}$ A after approximately 22 hours. Measurements on the up left electrode reached a current up to -2.16 $\cdot 10^{-6}$ A.
For samples PK002 and PK003, only a very small photo response was observed, depicted in figure 4.7. On the left, the photovoltage of PK002 is shown, where around 2 mV were obtained. On the right, for PK003, around -2 mV were measured.
No current measurements were performed for samples PK002 and PK003 due to the low voltage measurements. Notable is the throughout negative sign of photovoltage, except for PK002, where a very small positive voltage was measured. The polarity change indicates a changed mechanism behind the voltage.

Discussion – next steps

After looking at the first three prepared samples, the only one showing a notable photovoltage was PK001, i.e. the sample with a thin film thickness of around 840 nm. As the origin of the photovoltage was not quite sure, we decided to prepare another sample with the same parameters set and see if PK001 is reproducible in terms of photovoltage.

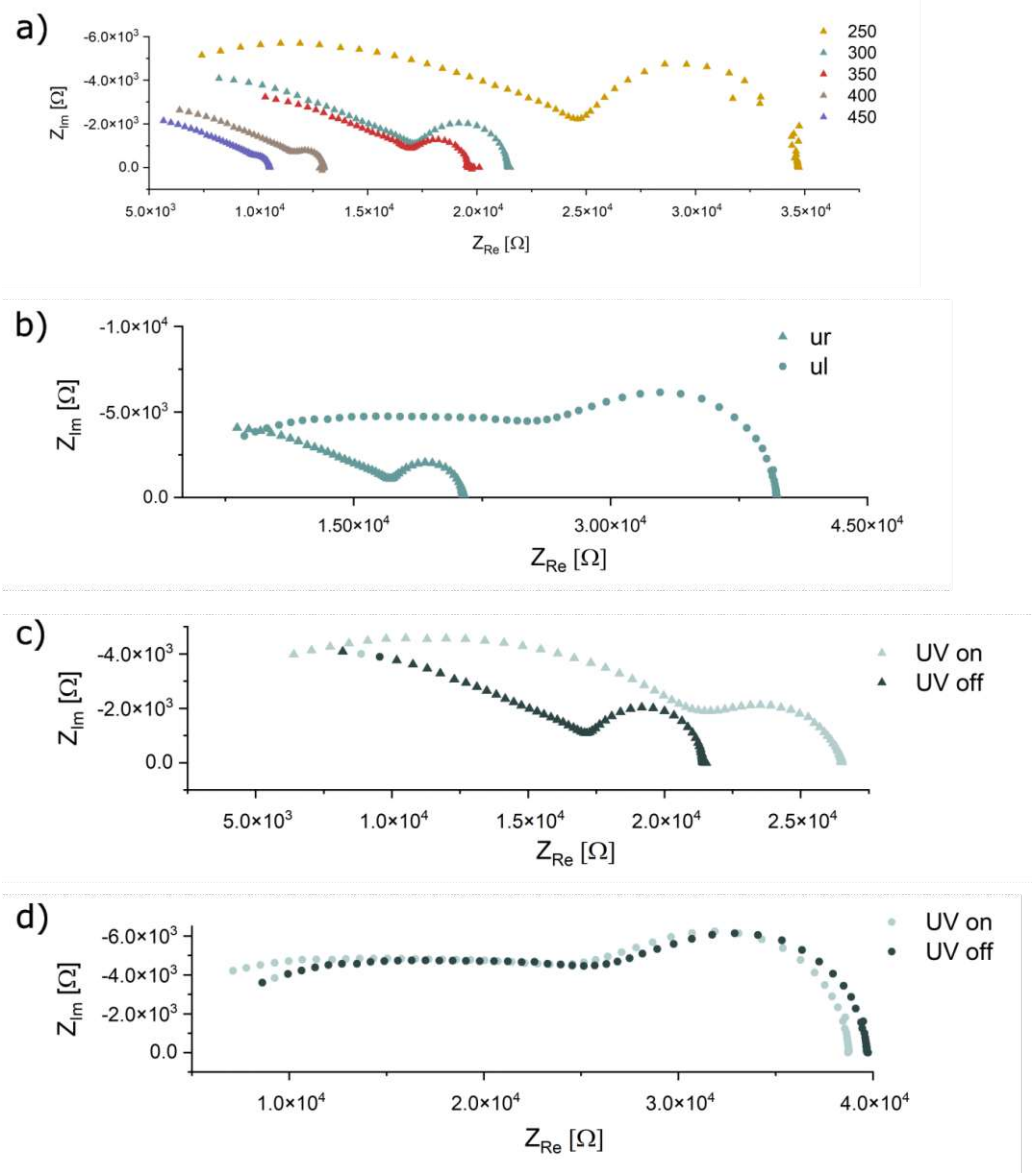

Figure 4.2: Impedance spectra measured for PK001: a) Temperature dependence on the up right electrode. b) Comparison of up left and up right electrode at 300°C. c) Up right electrode under UV irradiation and in the dark. d) Up left electrode under UV irradiation and in the dark.

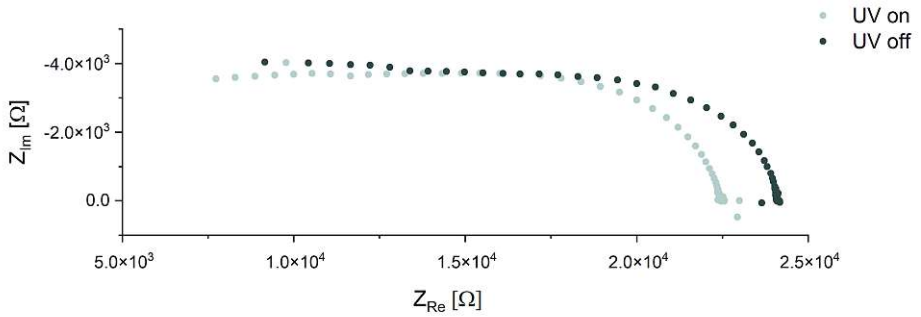

Figure 4.3: Impedance spectrum of PK002, measured with UV light on and off at the up left electrode at 300°C.

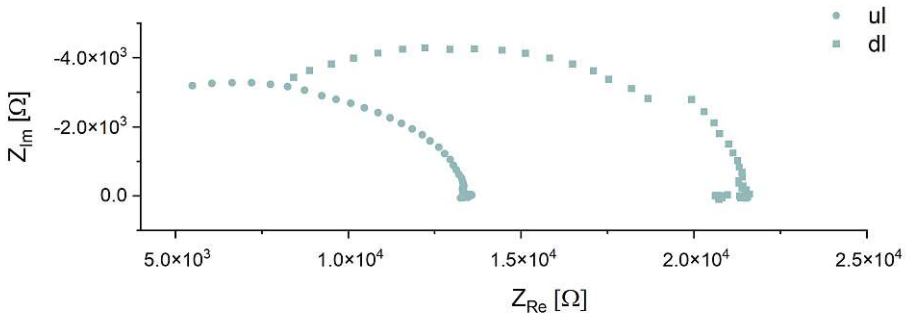

Figure 4.4: Impedance spectrum of PK003, measured at the up left and down left electrodes at 300°C.

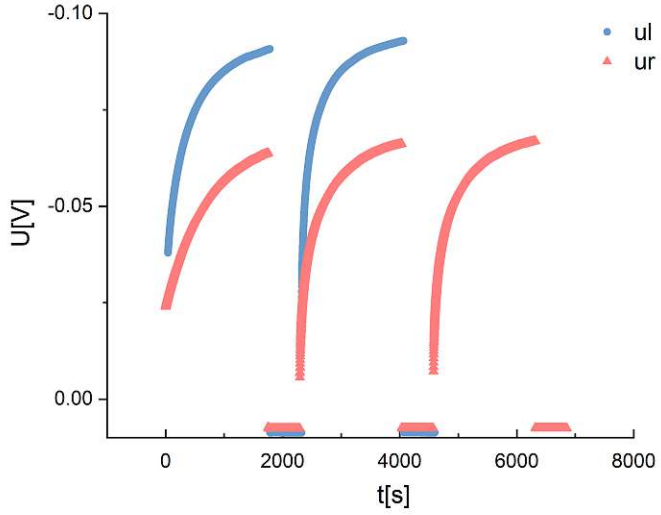

Figure 4.5: Voltage measurement cycles of PK001, measured at the up left and up right electrodes at 300°C.

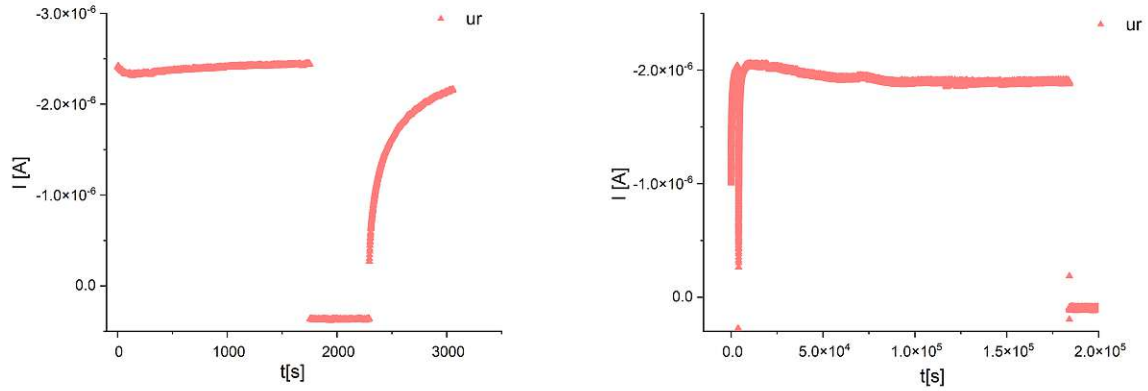

Figure 4.6: Current measurement cycles of PK001, measured at the up right electrode at 300°C. Left: Short cycle with 20 min UV irradiation, 10 min dark, 10 min irradiation. Right: Long measurement of about 50 hours, after one hour a short UV off – UV on switch was made.

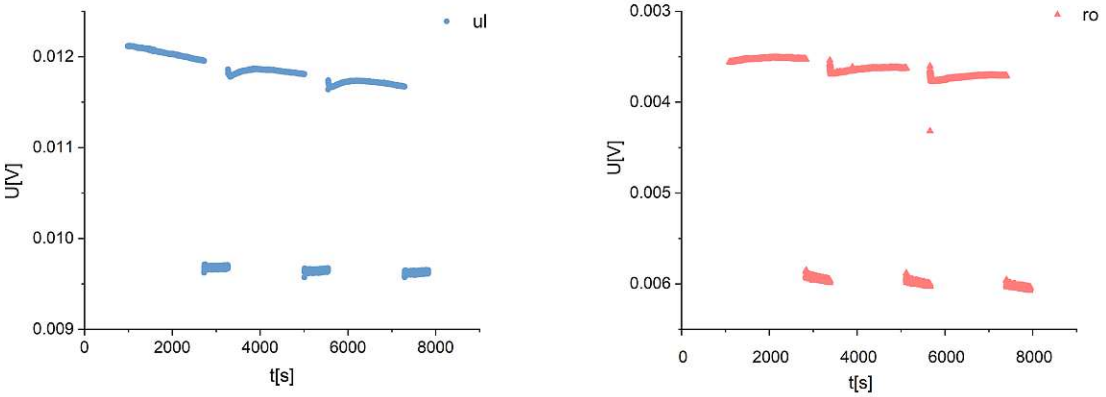

Figure 4.7: Voltage measurements. Left: PK002. Right: PK003. For both measurements, three 30 min UV on - 10 min UV off cycles were made. Both samples showed a very small photo-response. For PK002 the measured voltage was around 2 mV, for PK003 around -2 mV.

4.2 Sample with pronounced photovoltaic response

Sample PK004 was prepared the exact same way as PK001 in terms of set parameters. It turned out to be the best performing STO thin film based solar cell sample prepared. Voltages over -800 mV and currents over -2.11 $\cdot 10^{-5}$ A were achieved under ambient air conditions at 300°C.
For this sample, a lot of measurements were done to see how it behaves under different conditions and over longer time scales. Besides the temperature dependent impedance measurements, also temperature dependent voltage and current measurements were carried out. Furthermore, long-lasting voltage and current cycles were performed to investigate the long-term behaviour and stability. Additionally, measurements under synthetic air condition were performed.

Impedance spectroscopy

The impedance measurements for this sample are rather interesting and show a similar behaviour as the previous ones measured for PK001. The temperature dependence is the same, showing an impedance decline for rising temperatures. The temperature dependent impedance measurements are shown in figure 4.8. What we again observe are different impedance spectra for the three different contacted electrodes. The down left and up right electrode show just one low frequency feature. The up left electrode shows an interesting second semicircle in the mid to low frequency range, which fuses with the low frequency feature. In figure 4.9 the answer of the impedance spectra to UV irradiation is shown. For all three electrodes, a strong reduction of the mid to low frequency features is observed. The low frequency feature's behaviour under UV irradiation again leads us to believe that it comes from the space charge region build between LSCr and STO thin film. In subsection 3.3.1 a closer investigation of the low frequency feature is described and done.

Voltage and current measurements

The photovoltage measurements resulted in desired high voltages, though had a fairly large variation regarding the electrodes, as expected from the different impedance spectra. The up left electrode reached the highest value of about -830 mV followed by the down left electrode with around -680 mV and the up right electrode with -430 mV. The electrode dependent measurements are shown in figure 4.10 on the left. On the right, temperature dependent measurements are shown. The highest voltage of almost -1 V was reached at 250°C set.
The voltage also appears to be constant over shorter time scales (20 min), also when switching between dark mode and UV irradiation mode. A slight increase and also decrease can be observed at the start of the voltage measurements, ending in a kind of steady state after around 5 min. This time dependent behaviour is further discussed at the end of this subsection (subsection 4.8). When looking at the long-time measurement for the up left electrode at 300°C depicted in figure 4.12 on the left, a slight continuous increase can be observed. At the start of the illumination, the voltage seems to start at higher voltages, then drops about 30-40 mV over around 15 min and increases again slowly over time. After around 90 hours of illumination, the voltage seems to still increase.
The short circuit current measurements show the same trend as to the voltage measurements. For a set temperature of 300°C the up left electrode reached the highest amount of about -2.11 $\cdot 10^{-5}$ A. The down left electrode brought around -1.84 $\cdot 10^{-5}$ A, the up right one -1.11 $\cdot 10^{-5}$ A, depicted in figure 4.11 on the left. When comparing all three types of measurements (impedance, voltage, current) it becomes clear that the electrode with the smallest low frequency feature shows the least relative impedance change under UV irradiation, the smallest voltage and the smallest current. The first measurement series also fits to this observation, indicating some realtion between presence of a pronounced low frequency feature and a pronounced photovoltaic response.
Additionally, the current density was calculated by using the electrode area of (0.1089 cm^2). The current density is calculated to a value of -1.68 $\cdot 10^{-1}$ mA/cm^2 for the down left electrode, to -1.93 $\cdot 10^{-1}$ mA/cm^2 for the up left electrode and -1.02 $\cdot 10^{-1}$ mA/cm^2 for the up right electrode. The temperature dependent measurements, depicted in figure 4.11 on the right, show a maximum current at a set temperature of 350°C, reaching a slightly higher value than for 300°C of -2.25 $\cdot 10^{-5}$ A. At 250°C, where the highest voltage was measured, the current seems to decrease due to the increasing resistance. This observation affirms the temperature of 300°C used for

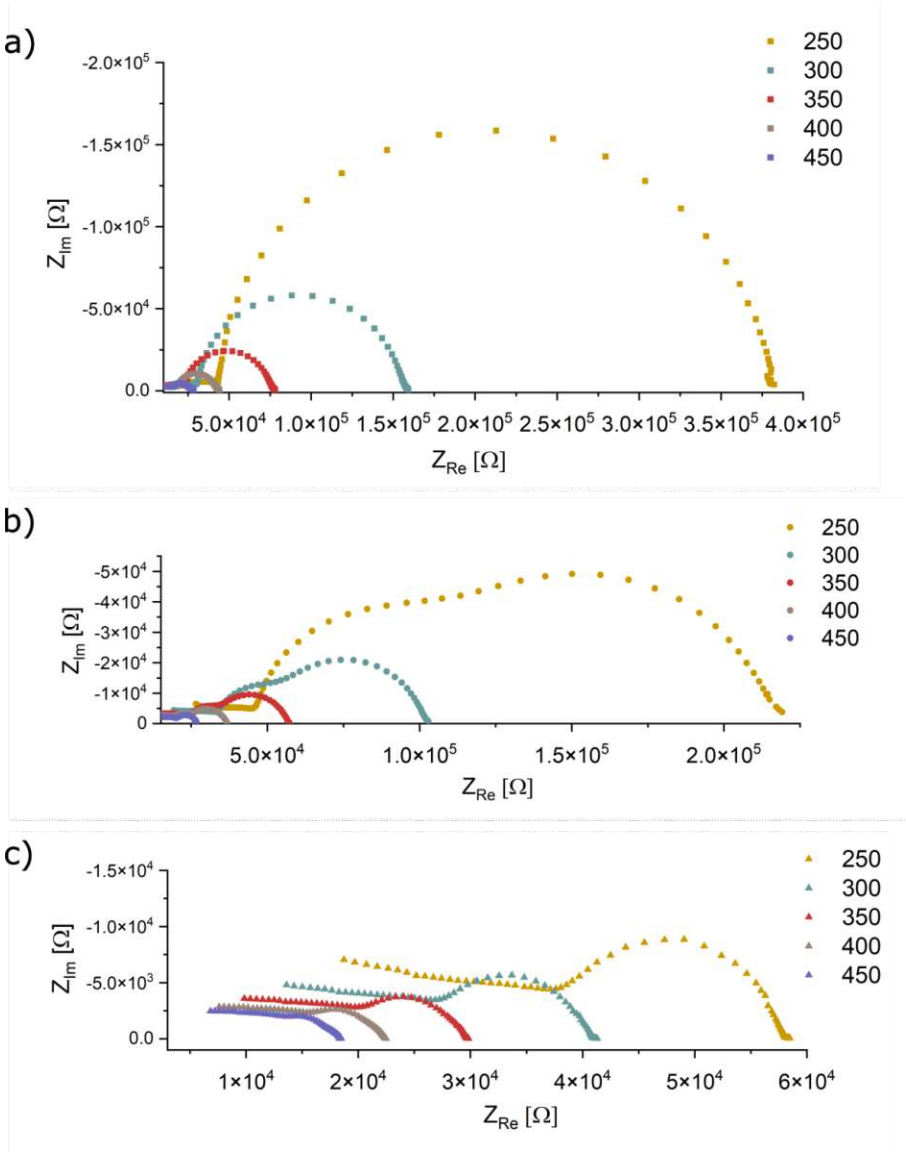

Figure 4.8: Temperature dependent impedance spectra of PK004: a) down left, b) up left, c) up right electrode.

the most measurements. The long-term behaviour of current measurements is rather constant, also reaching a steady state value after a few minutes, shown in figure 4.11 on the left.

Measurements under synthetic air conditions

As PK004 showed this promising results, further investigations were done using synthetic air as measurement environment. No significant changes regarding voltage or current values could be observed. The impedance measurements depicted in figure 4.13, figure 4.14 and figure 4.15 show smaller low frequency semicircles under synthetic air conditions, depicted in all three figures on the left. On the right, the behaviour upon UV light illumination is shown. The low frequency features seems to collapse like under ambient air conditions.
The voltage measurements show slightly higher voltages of -870 mV for the up left electrode and -750 mV for the down left electrode. The up right electrode yielded -330 mV, slightly less than under ambient air.
The short circuit current measured under synthetic air has a similar behaviour than the voltage, showing slightly higher currents for the up left ($-2.73 \cdot 10^{-5}$ A) and down left ($-2.29 \cdot 10^{-5}$ A) electrodes and a slightly lower current for the up right electrode ($-1.02 \cdot 10^{-5}$ A). The electrode dependent measurements are depicted in figure

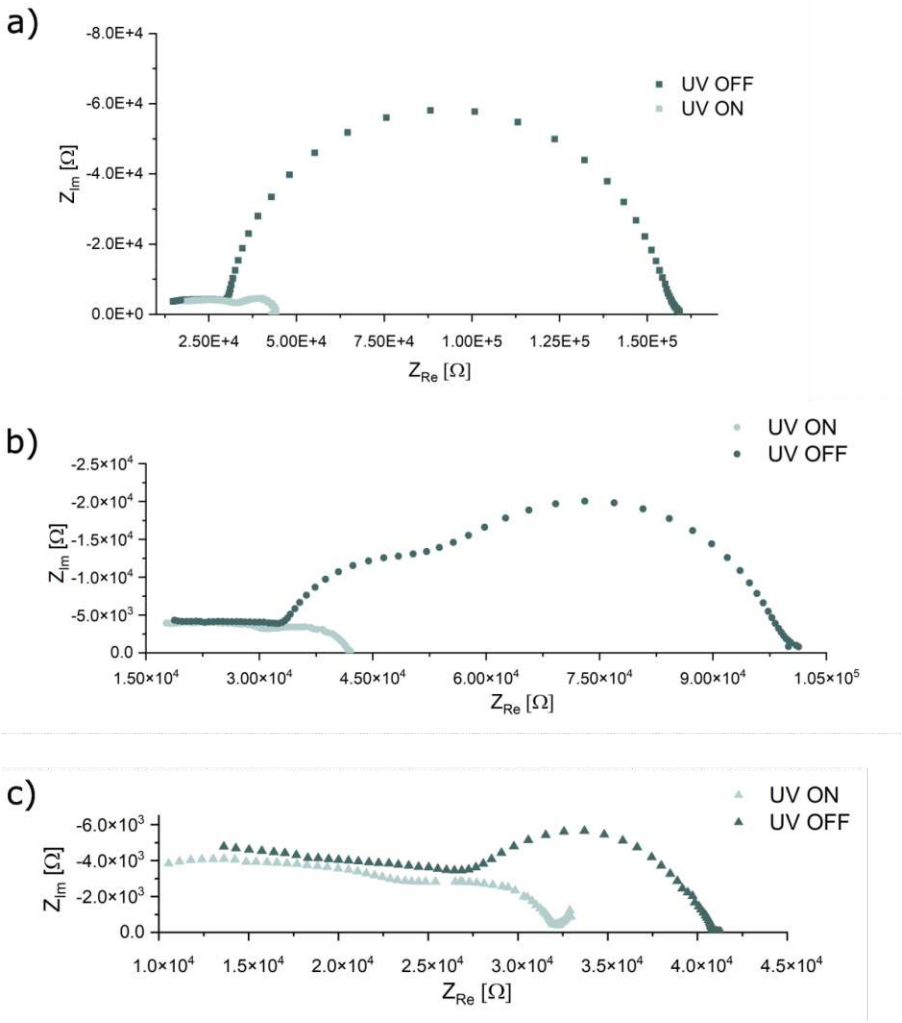

Figure 4.9: Impedance spectra of PK004 measured in the dark and under UV light irradiation contacted on the: a) down left, b) up left, c) up right electrode.

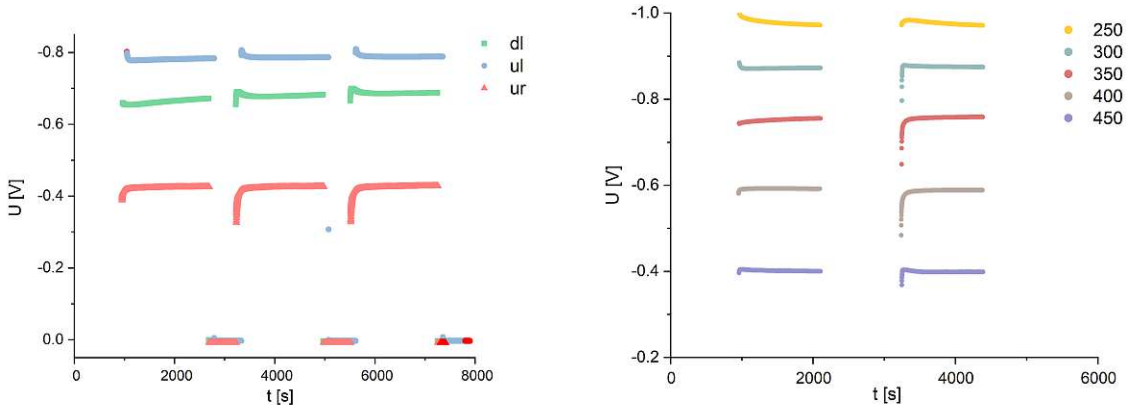

Figure 4.10: Voltage measurements of PK004. Left: Voltage measured for the three different electrodes. Right: Voltage measured at the up left electrode for different temperatures.

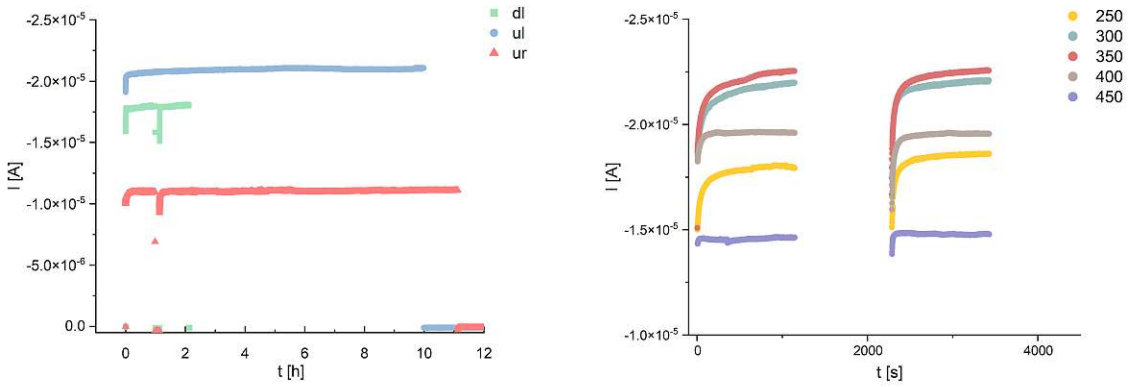

Figure 4.11: Current measurements of PK004. Left: Current measured for the three different electrodes. Right: Current measured at the up left electrode for different temperatures.

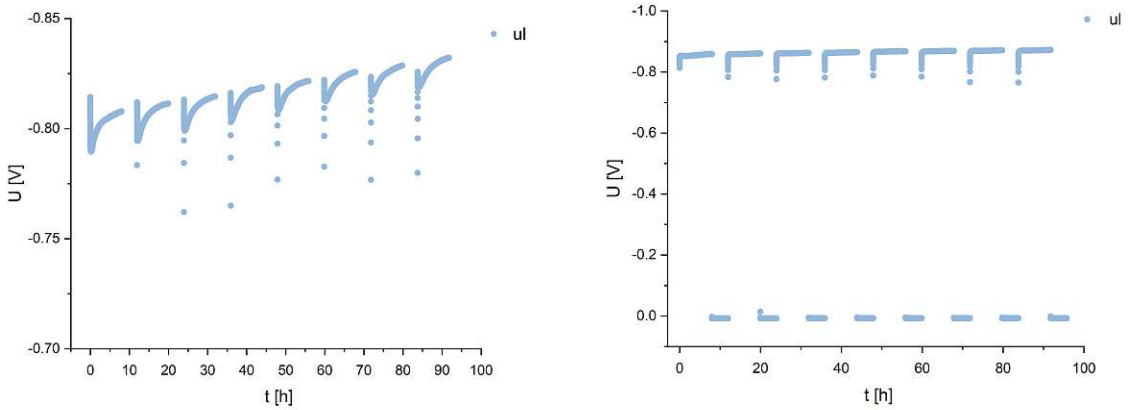

Figure 4.12: Long voltage measurement of PK004 contacted at the up left electrode. Left: Ambient air conditions. Right: Synthetic air conditions.

4.17 on the left. The current densities calculated under synthetic air conditions are -2.10 $\cdot 10^{-1}$ mA/cm^2 for the down left electrode, -2.51 $\cdot 10^{-1}$ mA/cm^2 for the up left electrode and -9.37 $\cdot 10^{-2}$ mA/cm^2 for the up right electrode. The temperature dependent current density is depicted in figure 4.17 on the right. The temperature dependence under synthetic air is similar to the one in ambient air. A 16-hour measurement of the current density is shown in figure 4.18. After every UV cycle, the current needs about one hour to get back to a steady state, not changing much over time.

Discussion

After PK004 turned out that well, we decided to further try to reproduce such samples. For every following change of parameters, also a reference sample is prepared with the same set of parameters for every step in preparation. Those defined standard parameters are mentioned in subsection 3.1.

Moreover, it is investigated whether the observation of the low frequency feature and its collapse during UV irradiation indeed is an indicator of whether a substantial photovoltage can be measured or not.

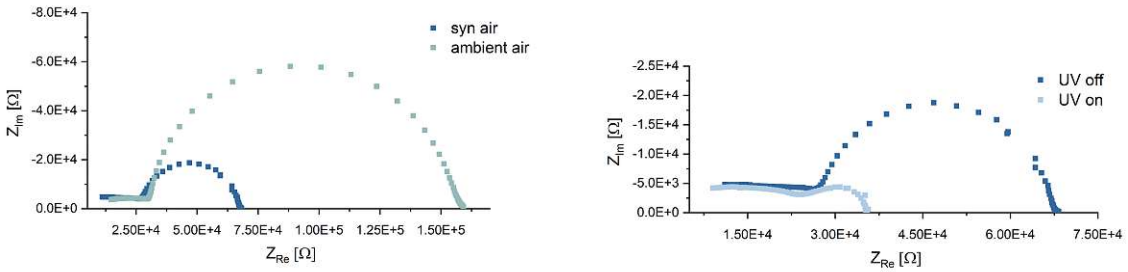

Figure 4.13: Impedance measurements of PK004 at the down left electrode under synthetic air conditions. Left: Difference between synthetic air and ambient air. Right: In the dark and under UV light irradiation.

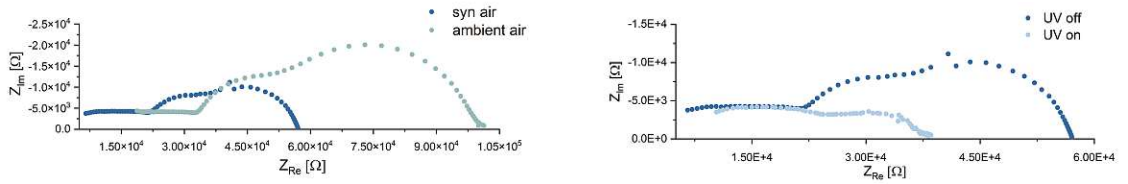

Figure 4.14: Impedance measurements of PK004 at the up left electrode under synthetic air conditions. Left: Difference between synthetic air and ambient air. Right: In the dark and under UV light irradiation.

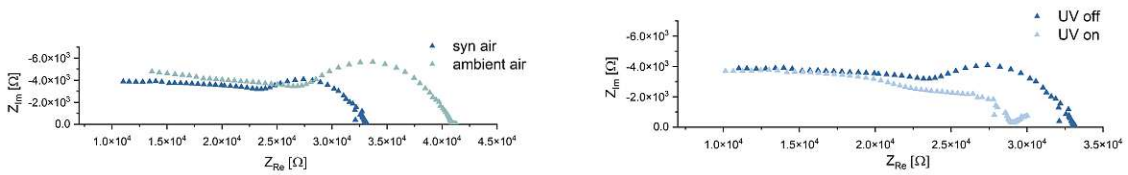

Figure 4.15: Impedance measurements of PK004 at the up right electrode under synthetic air conditions. Left: Difference between synthetic air and ambient air. Right: In the dark and under UV light irradiation.

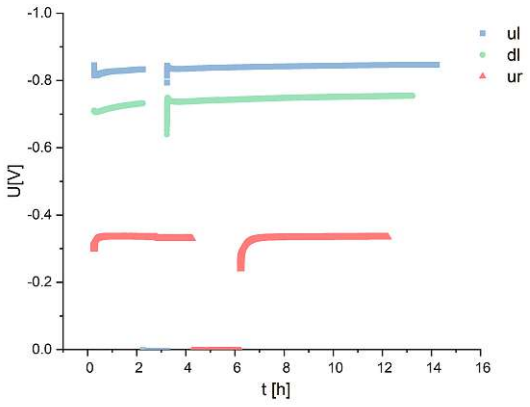

Figure 4.16: Voltage measurements of PK004 under synthetic air measured for the three different electrodes.

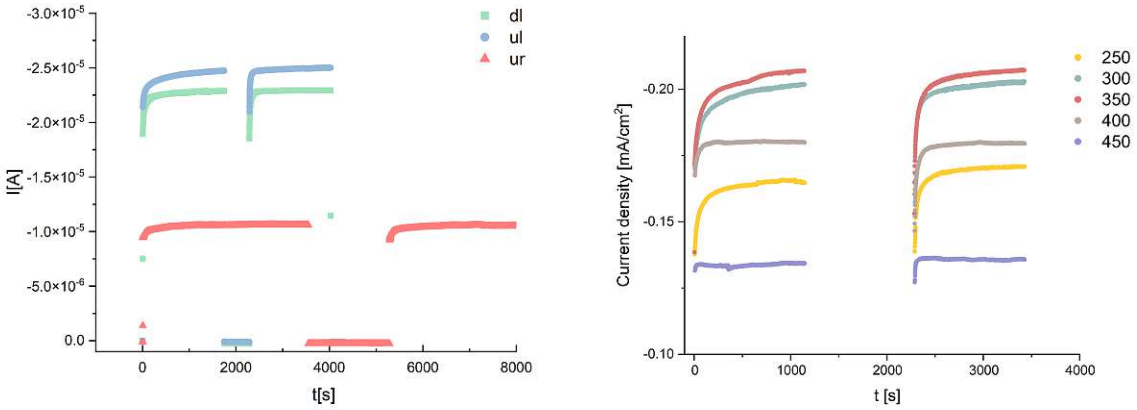

Figure 4.17: Current measurements of PK004 under synthetic air conditions. Left: Current measured for the three different electrodes. Right: Current density measured at the up left electrode for different temperatures.

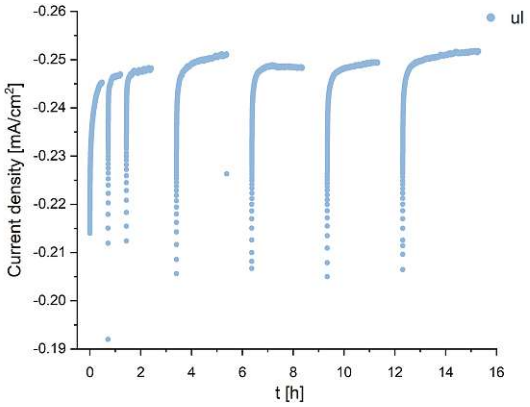

Figure 4.18: Long current density measurement of PK004 contacted on the up left electrode, measured under synthetic air conditions.

4.3 Samples with changed geometry

Subsequently, the STO thin film geometry was changed as described in subsection 3.1. The background for this change was a possible saving in material, as well as the possibility to try different thicknesses and shapes on one substrate. Sample PK006 was prepared with a "tower" shape. The thin film thicknesses stayed the same. A different approach to realise a "tower" shape was by etching the shape out of an already prepared sample. PK001 was taken, as we made use of already collected impedance, voltage and current data. Furthermore, the LSCr thickness was reduced to around 50 nm for sample PK007.

PK006 showed no interesting results. In figure 4.19 on the left, exemplary impedance spectra are shown and in figure 4.20 on the left a voltage measurement is shown. The impedance seems to decline during UV irradiation, but no low frequency feature can be observed. Also, a voltage reaction due to UV irradiation seems to appear but only in the range of a -0.1 mV step. Also sample PK007 showed no interesting results. In figure 4.19 on the right impedance spectra in the dark and under UV light irradiation are shown. Again, a slight decline under UV irradiation can be observed. In figure 4.20 on the right, the corresponding voltage measurement is depicted. A clear voltage jump due to the irradiation can be observed, but just in the range of 3 mV.

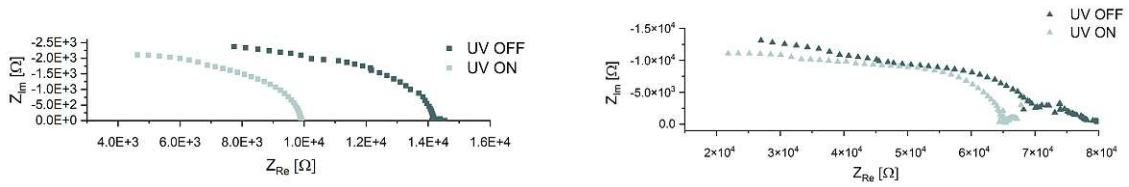

Figure 4.19: Exemplary impedance measurements of PK006 and PK007 at 300°C in the dark and under UV light irradiation. Left: PK006 contacted at the down left electrode. Right: PK007 contacted at the up right electrode.

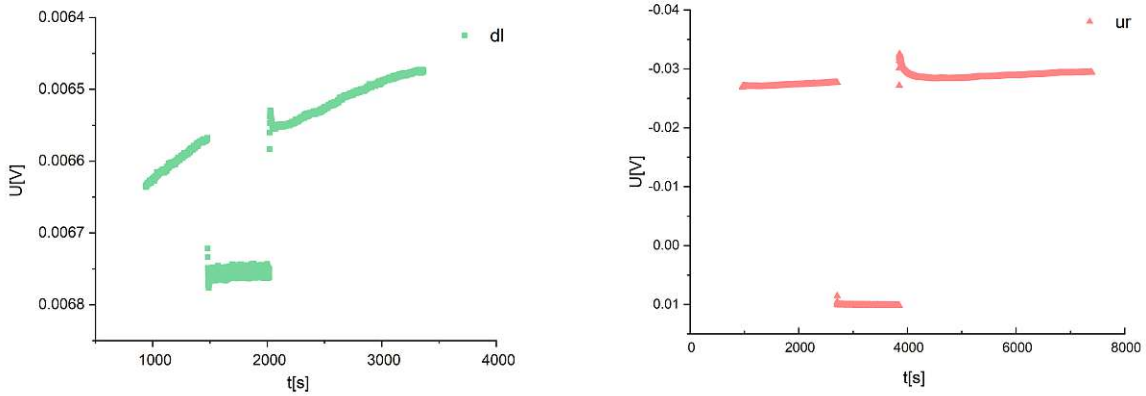

Figure 4.20: Exemplary voltage measurements of PK006 and PK007 at 300°C. Left: PK006 contacted at the down left electrode. Right: PK007 contacted at the up right electrode.

For PK001, the impedance changed after the etching process. In figure 4.21 and figure 4.22 the impedance data of the corresponding electrode is compared before (left) and after (right) the etching process. The low frequency feature in the dark grew for both cases. Also, the answer to the UV light irradiation changes, showing a clearer decrease of the low frequency feature. Furthermore, the measured photovoltage yielded a higher value. For the up left electrode, a photovoltage of around -188 mV was measured (compared to -100 mV before) and for the

up right electrode, a photovoltage of around -100 mV was measured (compared to around -66 mV before). The voltage measurements are depicted in figure 4.23.
This supports our hypothetical correlation between low frequency feature and photovoltaic response, though we do not attribute the changes to the geometry of the STO thin film, as we have no confirmation that the etching process fully removed the STO thin film, resulting in the wanted tower shape.

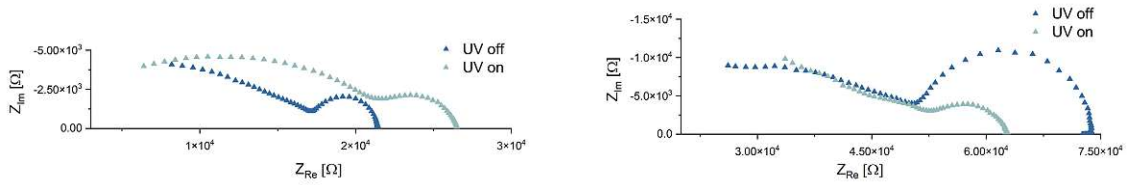

Figure 4.21: Comparison of measured impedance data before (left) and after etching (right) contacted at the up right electrode of sample PK001.

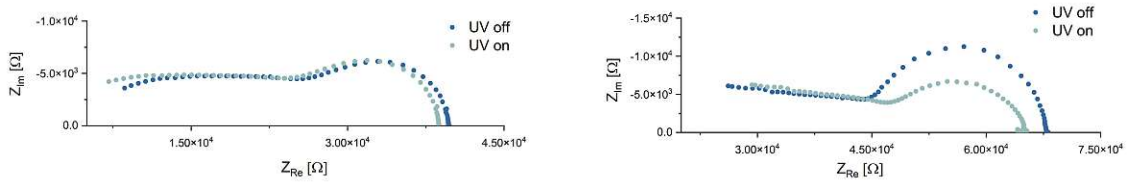

Figure 4.22: Comparison of measured impedance data before (left) and after etching (right) contacted at the up left electrode of sample PK001.

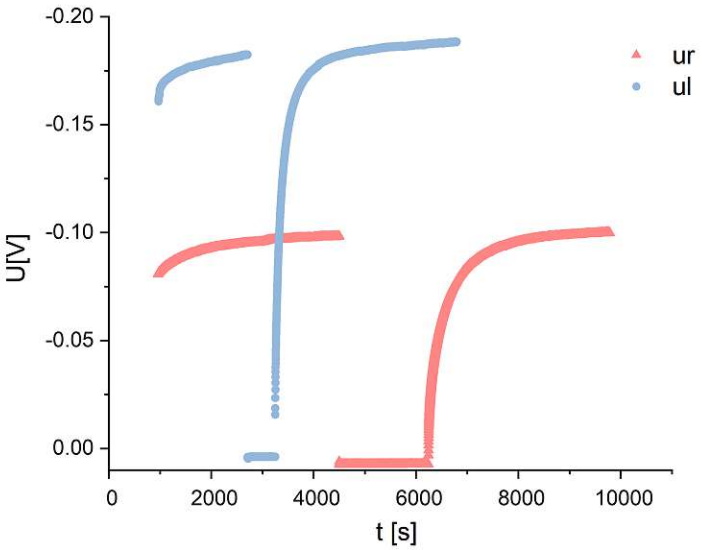

Figure 4.23: Voltage measurements after etching contacted at the up left and up right electrode of sample PK001.

Reference sample PK005

The prepared reference sample PK005 showed similar behaviour as PK001. Though, just the up left and up right electrode achieved voltage. For the up left electrode -64 mV were measured, for the up right electrode -120 mV. The voltage measurement contacted on the up right electrode is shown in figure 4.25 on the left. On the right the current measurement is shown, reaching up to -3.04 $\cdot 10^{-6}$ A. Both voltage and current measurements were performed at 300°C set. The time behaviour is not further investigated but looks similar as the ones observed for the other reference samples.
The impedance spectra shown in figure 4.24 were measured also on the up right electrode at 300°C in the dark and under UV light irradiation. At low frequencies, two features seem to be merged, but hard to keep separated as well as investigated. The low frequency feature under UV irradiation shows a clearer semicircle. Due to the measured photovoltage, the feature is again attributed to the space charge.

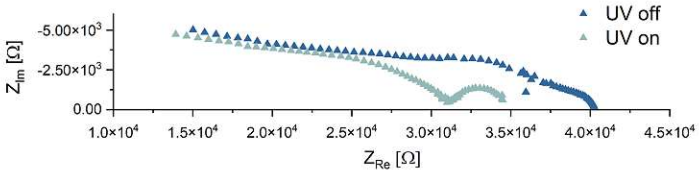

Figure 4.24: Impedance measurements of PK005 contacted at the up right electrode at 300°C in the dark and under UV light irradiation.

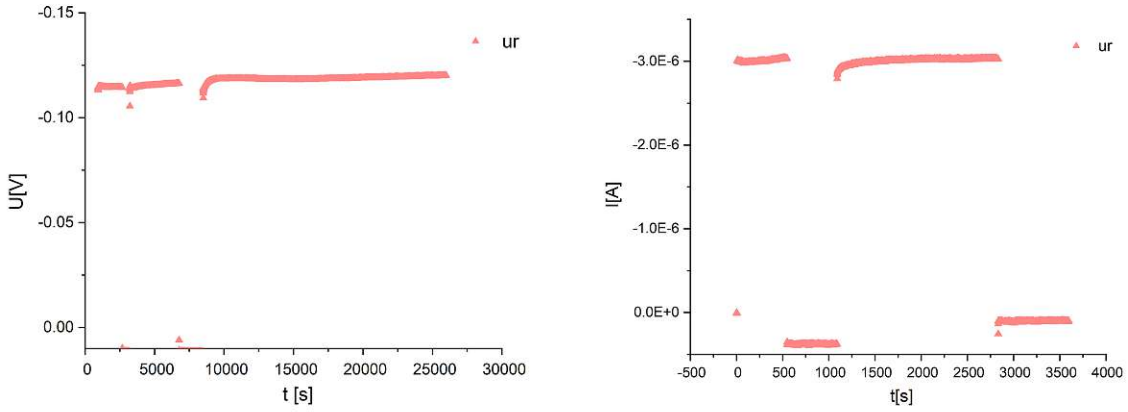

Figure 4.25: Voltage (left) and current (right) measurements of sample PK005 contacted at the up right electrode at 300°C.

4.4 Variation of the Sr overcompensation

Another varied parameter was the Sr overcompensation in the PLD target. As already mentioned, the Sr overcompensation is done because of a Sr deficiency in deposited thin films. In previous works, e.g. [19], a 7% overcompensated Fe doped STO target yielded stoichiometric Fe:STO thin films. For the 7% overcompensated undoped STO target used here, a similar behaviour is assumed. Since good sample reproducibility has not yet been achieved, it was assumed that stoichiometry changes in the PLD still cause non-stoichiometric thin films with possibly shifted or pinned Fermi levels that prevent the formation of a space charge zone.
For the variation, a 10% Sr overcompensated STO target as well as a stoichiometric STO target (0%) were used. The 10% Sr overcompensated target was used for the STO thin film of sample PK008. The stoichiometric STO target was used for sample PK009. All other parameters stayed the same (see table 6 and table 1).
Both samples showed the already familiar low frequency feature. For sample PK008, all three electrodes had semicircles in a similar order of magnitude, two are depicted in figure 4.26 on the left. The answer to UV light is also comparable. In figure 4.26 on the right, the measured voltages of the regarding electrodes can be seen. The highest voltage of almost -200 mV was measured at the up right electrode. In figure 4.27 on the left, a 12 h voltage measurement is depicted, showing a fast increase at the start of illumination for about 45 min, then continuing with a slight increase over time. On the right, a 8 h current measurement is depicted. The current appears to be constant after a 45 min increase, like the photovoltage. A current of -5.68 $\cdot 10^{-6}$ A is reached.
PK009 showed similar impedance, voltage and current measurements for the up left and down left electrodes. The impedance is similar to the ones of PK008, the low frequency feature also collapses when irradiated with UV light (see figure 4.28 on the left). A voltage of above -100 mV and a current of -3.51 $\cdot 10^{-6}$ A was reached (depicted in figure 4.29 left and 4.30 left). For the up right electrode, a big low frequency feature was observed, which also collapsed under UV irradiation (4.28 right). The feature is of the same order of magnitude as the one observed in sample PK004 (dl). A photovoltage of just over -300 mV was measured (4.29 right) which is only half of the amount measured for the corresponding electrode in sample PK004. However, it is still much more than for PK008 and qualitatively in line with our supposed correlation of impedance feature and photovoltaic answer. For the up right electrode, a current of -5.2 $\cdot 10^{-6}$ A was measured.

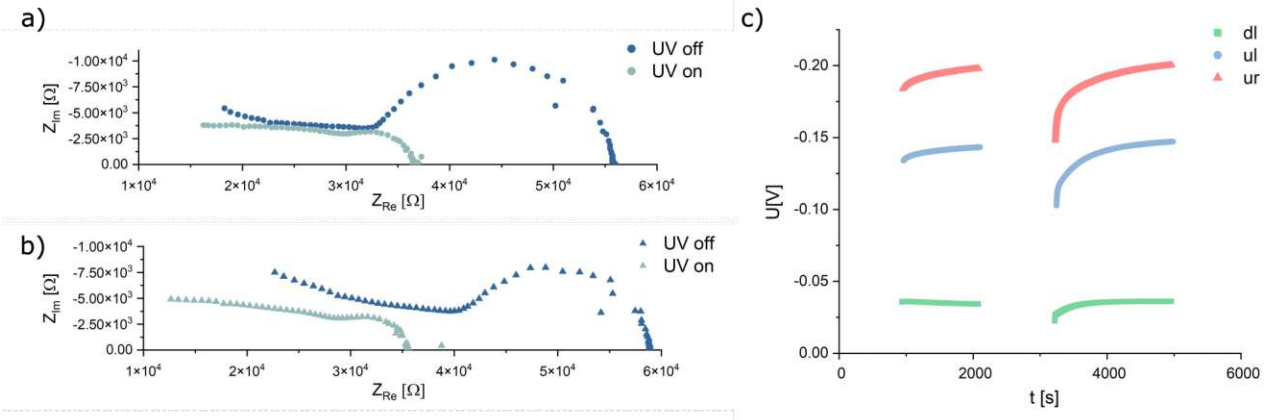

Figure 4.26: Impedance and voltage measurements of PK008. a) Impedance spectra in the dark and under UV light irradiation, contacted on the up left electrode. b) Impedance spectra in the dark and under UV light irradiation, contacted on the up right electrode. c) Voltage measurements contacted on the three corresponding electrodes.

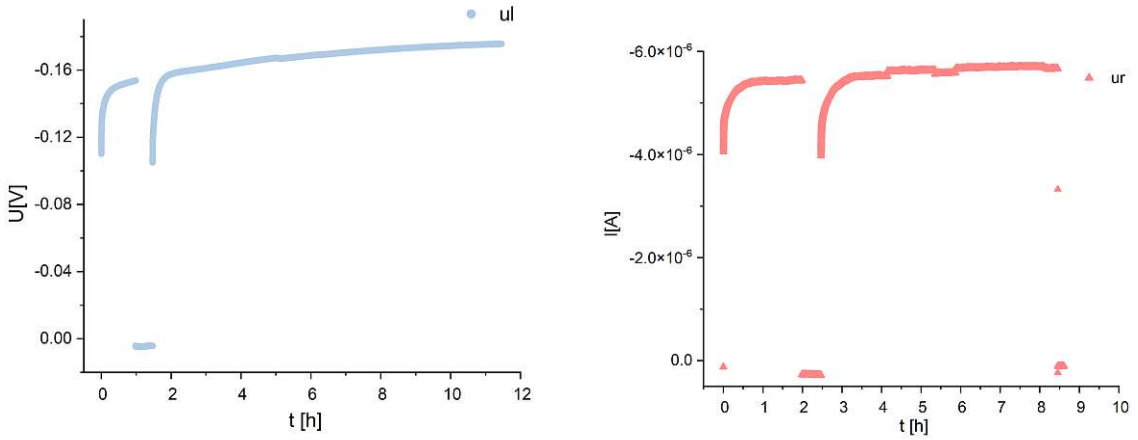

Figure 4.27: Voltage and current measurements of sample PK008. Left: Voltage measurement contacted on the up left electrode. Right: Current measurements contacted at the up right electrode.

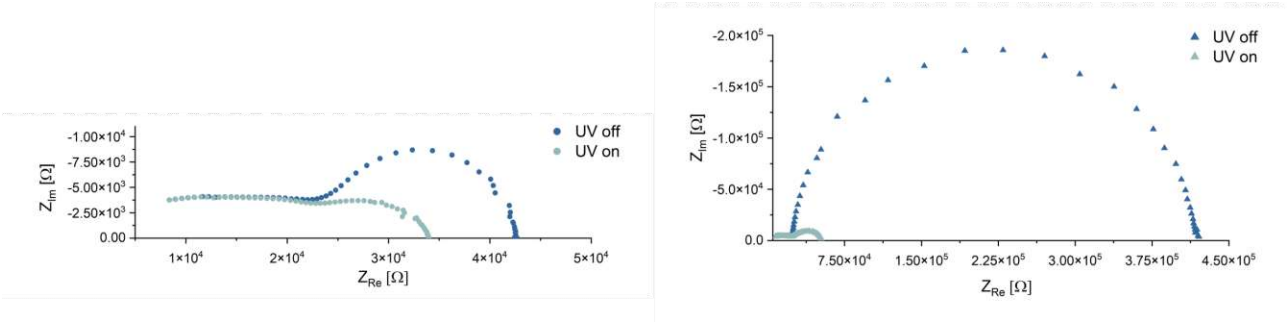

Figure 4.28: Impedance measurements of sample PK009 in dark and under UV light irradiation. Left: Contacted on the up left electrode. Right: Contacted on the up left electrode.

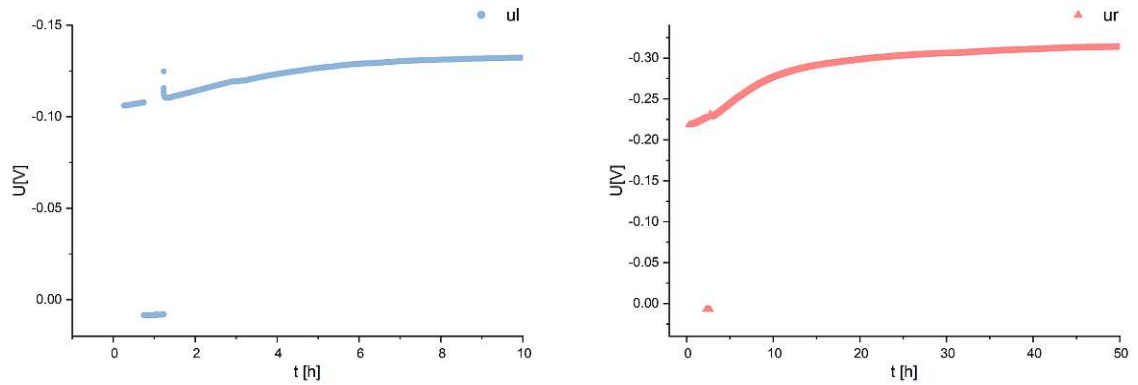

Figure 4.29: Voltage measurements of sample PK009. Left: Contacted on the up left electrode. Right: Contacted at the up right electrode.

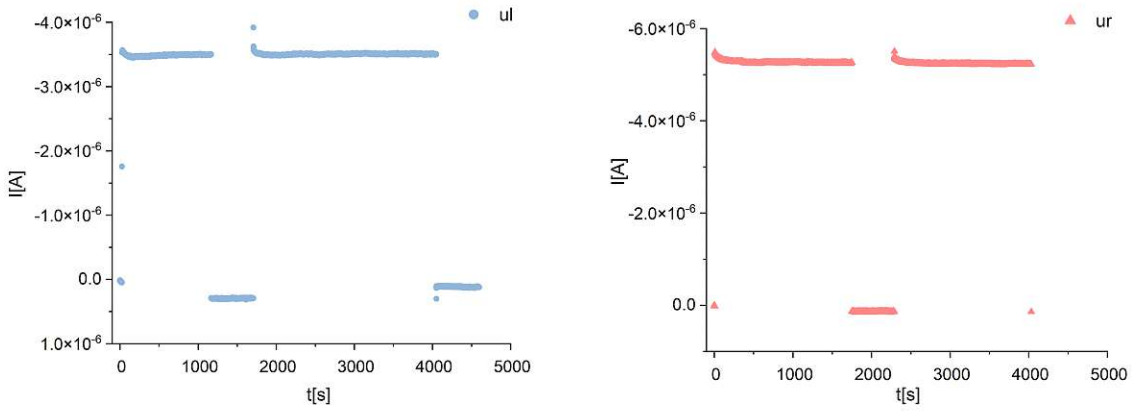

Figure 4.30: Current measurements of sample PK009. Left: Contacted on the up left electrode. Right: Contacted at the up right electrode.

Reference sample PK0010

Reference sample PK010, interestingly, showed no meaningful results, highlighting the observed reproduction problem. The way of preparation appears to be hard to fully control. The only noticed difference for this sample is a higher laser power used to keep the fluence at around 1 J/cm^2. This is kept in mind for further preparations, though it seems unlikely to be the main reason. It could though be that the fluence measurement is prone to errors. In figure 4.31 exemplary impedance and voltage measurements are shown. The voltage measurement does show a reaction to UV light, but just in a range of -0.1 mV.

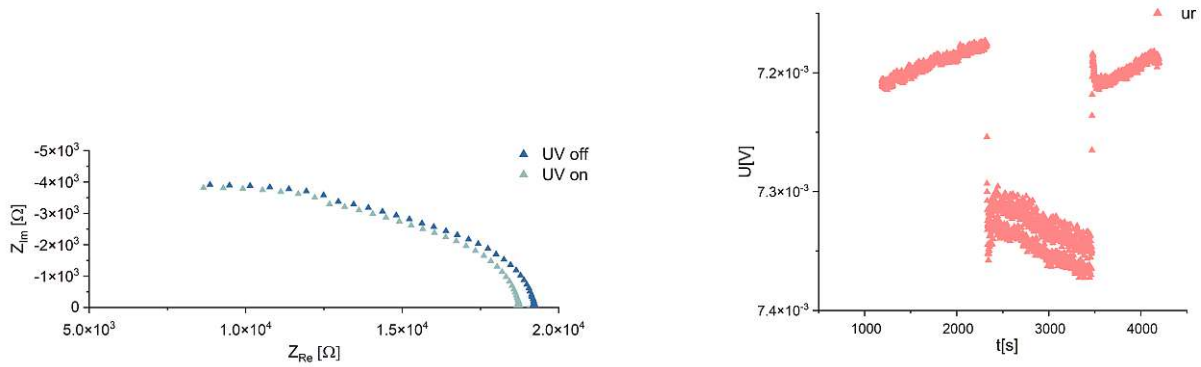

Figure 4.31: Exemplary impedance and voltage measurements of sample PK010. Left: Impedance in the dark and under UV light irradiation, contacted on the up right electrode. Right: Voltage measurement contacted at the up right electrode.

4.5 Fluence variation

The fluence is varied in two ways. Once higher and once lower than the used standard fluence of around 1 J/cm^2. The fluence is determined by measuring the spot size as well as the laser energy in the vacuum chamber. A more precise description can be found in subsection 3.1. For sample PK011, the fluence was set to around 0.8 J/cm^2. Also, the deposition rate was measured with QCM, resulting in a lower deposition rate than normal (see table 4).
For PK011, no photovoltage was measured, in accordance with the impedance spectra which revealed no clear space charge feature. Only a very small answer to UV light irradiation can be observed. Exemplary measurements of sample PK011 are shown in figure 4.32.

For sample PK015, the fluence was set to about 1.2 J/cm^2. The QCM measurement showed much lower deposition rates though, indicating a wrong fluence measurement, which could be even smaller than 0.8 J/cm^2. The measurements for PK015 revealed similar results as for sample PK011. Exemplary impedance and voltage measurements are shown in figure 4.33. These two samples show that a low fluence or deposition rate is not useful for STO thin films. Another point learned was, that the spot size measurements can bring wrong results. For further preparations, the deposition rate was always measured. Furthermore, higher fluences of around 1.1 J/cm^2 were used for samples PK017, PK021 and PK027, though not showing significant improvements.

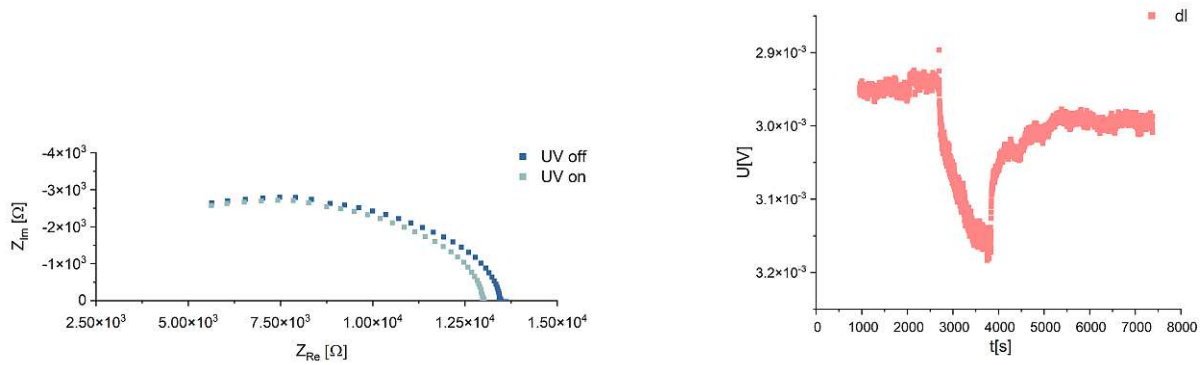

Figure 4.32: Exemplary impedance and voltage measurements of sample PK011. Left: Impedance in the dark and under UV light irradiation, contacted on the down left electrode. Right: Voltage measurement contacted at the down left electrode.

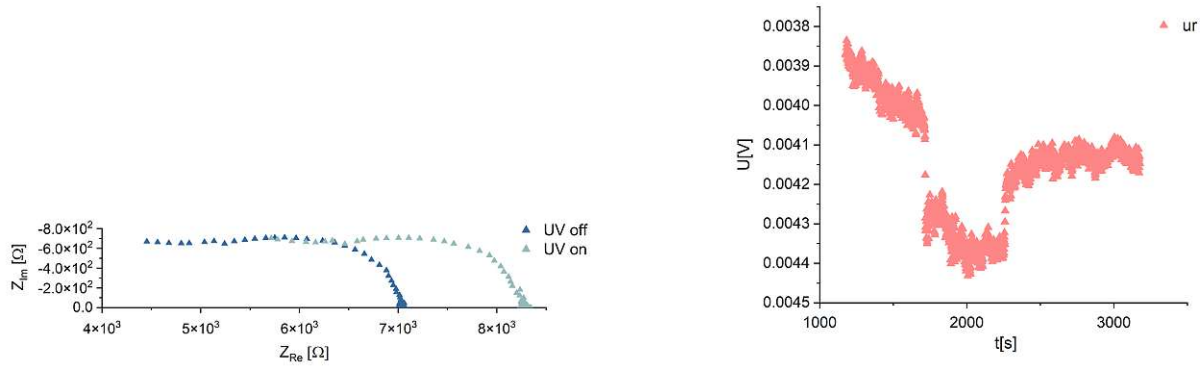

Figure 4.33: Exemplary impedance and voltage measurements of sample PK015. Left: Impedance in the dark and under UV light irradiation, contacted on the up right electrode. Right: Voltage measurement contacted at the up right electrode.

Reference sample PK012

Interestingly, reference sample PK012 showed again very high photovoltages. The only difference in preparation compared to PK004 was a changed top electrode geometry, trying a geometry with one larger rectangular and one square electrode (see also subsection 3.1). This change should not influence the behaviour of the voltage generation. It can just bring different absolute current values. The impedance measurements, shown in figure 4.34 and figure 4.35, again show the low frequency semicircle for both electrodes, which collapses under UV light irradiation. Also, the temperature dependent behaviour is the same as for PK004. Notable is the much larger low frequency semicircle observed at the up right electrode compared to the up left one.
The voltage measurements of a long measurement cycle (4.36 a)) shows a fairly constant, slightly decreasing voltage over time. At the beginning of every UV irradiated phase, the voltage reaches an almost constant value after one hour with values of up to about -680 mV. Similar behaviour was observed for the up right electrode. Initially, a slightly higher starting voltage is formed, which then drops to a constant value. The second cycle showed the same behaviour as the up left electrode. The up right electrode yielded a voltage of around -650 mV (figure 4.36 b)). The current measurements are depicted in figure 4.36 c). They both show a faster increase until a steady state is reached when first illuminated with UV light. When the up left electrode is contacted, a current value of -2.59 $\cdot 10^{-5}$ A was measured. For the up right electrode, -1.66 $\cdot 10^{-5}$ A were measured. The difference again is assumed to be due to the larger top electrode on the left. In figure 4.37, voltage and current measurements under synthetic air conditions, contacted on the up left electrode, are shown. The behaviour remained essentially the same. The voltage reached up to -690 mV, a bit higher than under ambient air conditions. The current reached -2.34 $\cdot 10^{-5}$ A, a bit lower than under ambient air conditions. The overall behaviour is thus very similar to sample PK004.

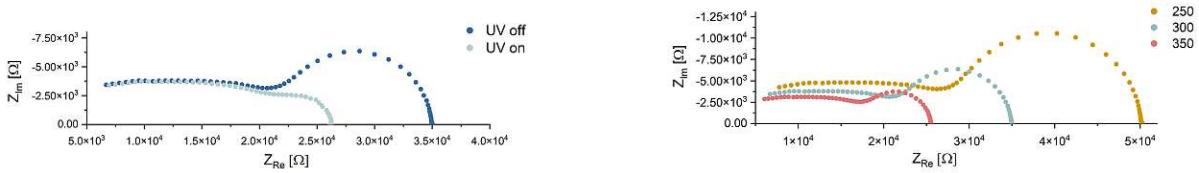

Figure 4.34: Impedance measurements contacted on the left electrode of sample PK012. Right: Temperature dependent. Left: In dark and under UV irradiation.

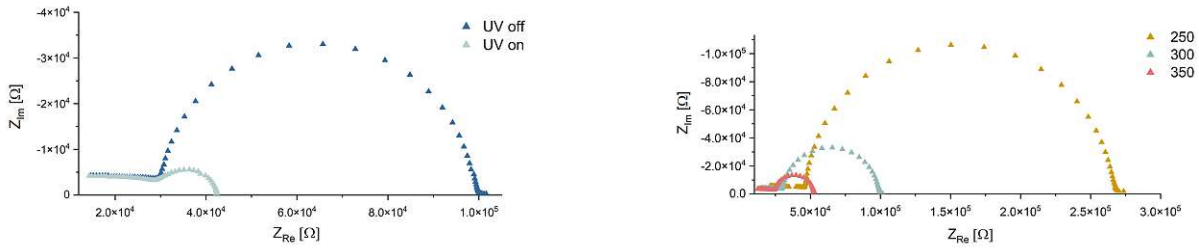

Figure 4.35: Impedance measurements contacted on the up right electrode of sample PK012. Right: Temperature dependent. Left: In dark and under UV irradiation.

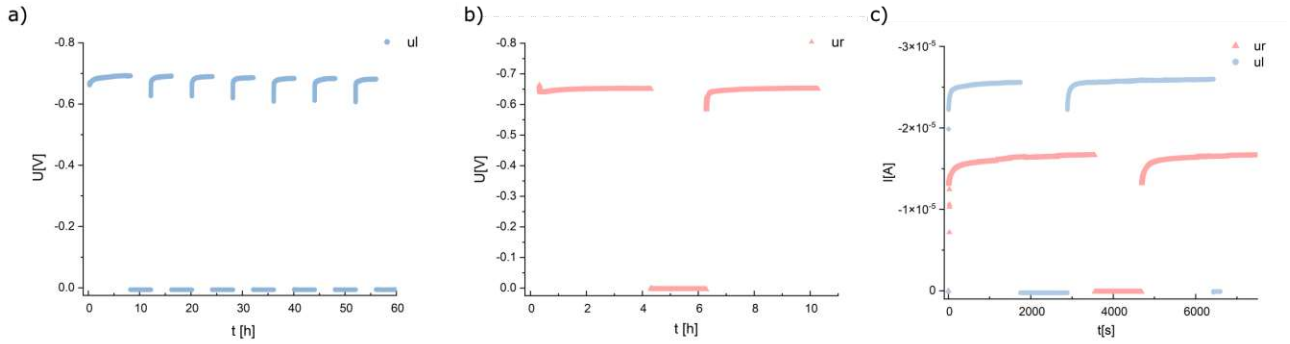

Figure 4.36: a) Voltage measurement contacted on the left electrode. b) Voltage measurement contacted on the up right electrode. c) Current measurements contacted on the left and up right electrode.

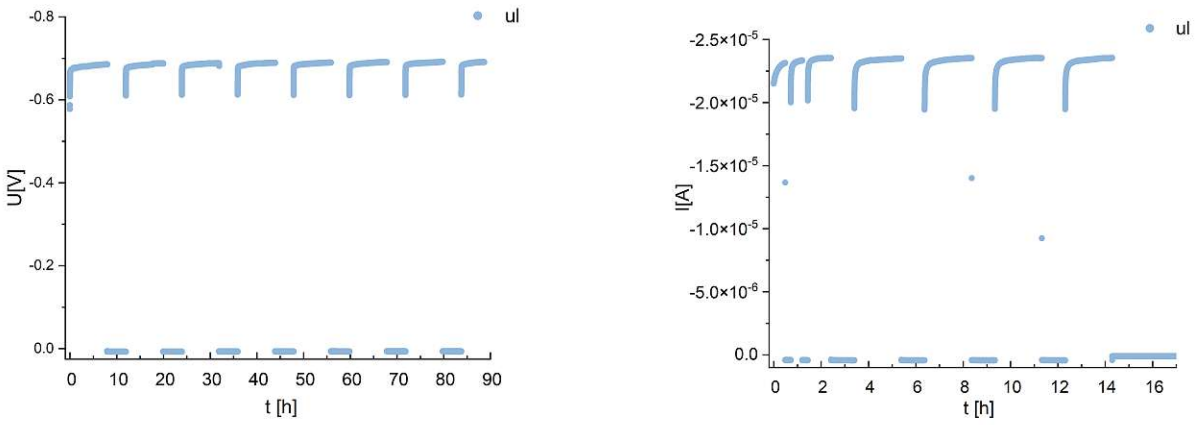

Figure 4.37: Voltage and current measurements of sample PK012 under synthetic air conditions, contacted on the up left electrode.

Reference samples PK013 & PK014

Samples PK013 and PK014 were prepared before and after a PLD laser gas exchange. The reason was the previous results, suggesting a trend in samples with high photovoltaic voltages which were prepared after a laser gas exchange. PK013 and PK014 unfortunately again showed no photovoltaic activity. Only a negligible voltage can be observed in both voltage measurements, depicted in figure 4.38 and figure 4.39 on the right. Sample PK013 showed a positive polarised photo response, assumed to come from a ionic process. The impedance spectra shown in figure 4.38 and figure 4.39 on the left look similar, showing just a rounded low frequency ending. Both impedance spectra show a small reduction during irradiation with UV light.

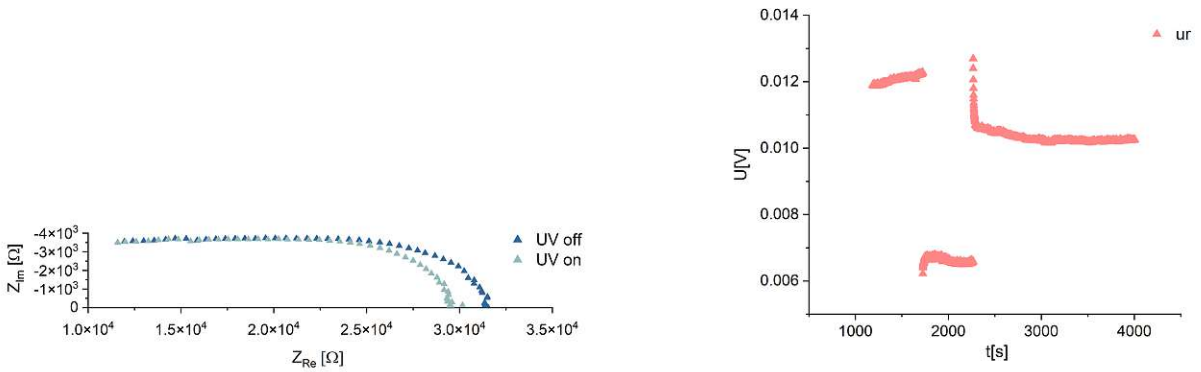

Figure 4.38: Exemplary impedance and voltage measurements of sample PK013. Left: Impedance in the dark and under UV light irradiation, contacted on the up right electrode. Right: Voltage measurement contacted at the up right electrode.

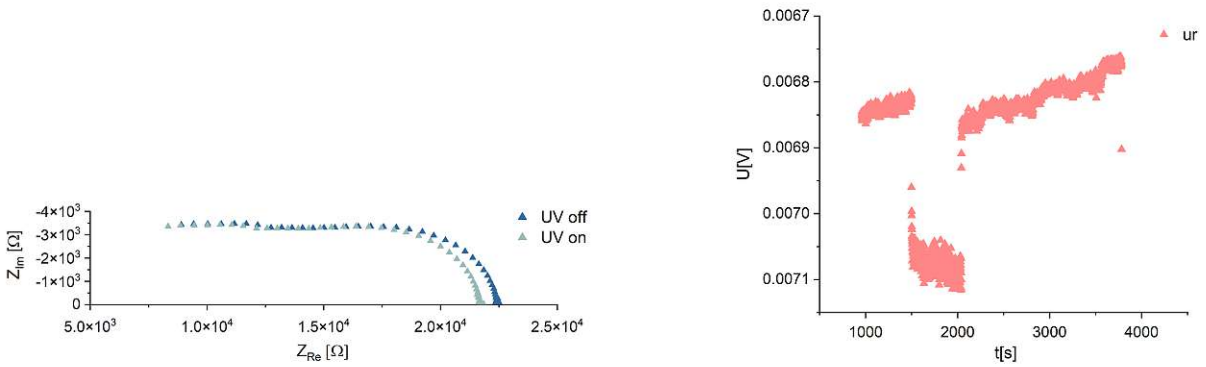

Figure 4.39: Exemplary impedance and voltage measurements of sample PK014. Left: Impedance in the dark and under UV light irradiation, contacted on the up right electrode. Right: Voltage measurement contacted at the up right electrode.

4.6 Change of deposition temperature

For sample PK017 the heating power was increased from 65% to 80%. The fluence was 1.1 J/cm^2, a bit higher than the standard fluence. The higher fluence also results in a higher deposition rate, for STO 7% in this case to 0.0207 nm/puls (see table 4). The impedance measurement showed a low frequency feature at the up left electrode. Under UV light irradiation, the low frequency features shrunk. The impedance spectrum in the dark and under UV light irradiation is shown in figure 4.40 on the left.
As expected from the impedance spectra, the voltage measurements showed a photovoltaic voltage for the up left electrode, though a voltage of only about -20 mV was reached. The time dependent behaviour shows a steep voltage increase at the start of a irradiation cycle, followed by a decrease over time.
Compared with sample PK004 and PK012, the results of sample PK017 were inferior, leaving the standard sample parameters still as the most promising.

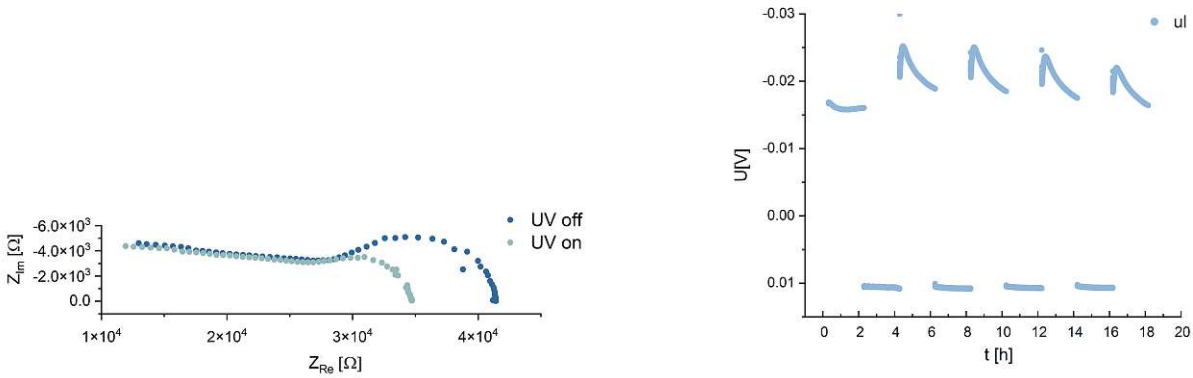

Figure 4.40: Exemplary impedance and voltage measurements of sample PK017. Left: Impedance in the dark and under UV light irradiation, contacted at the up left electrode. Right: Voltage measurement contacted at the up left electrode.

Reference samples PK016 & PK018

Sample PK016 was deposited with a larger laser energy set of 440 mJ, but a standard fluence of 1 J/cm^2. The sample showed a comparatively small low frequency arc, which changed under UV light irradiation. The down left and up left electrodes showed similar impedance spectra, the one for the up left electrode is shown in figure 4.41 on the left. The impedance spectra in the dark and under UV light irradiation of the up right electrode is shown on the right. Substantial voltages in the -200 mV range were measured for two electrodes and are shown in figure 4.42 on the left. An interesting jump of the voltage could be observed for the down left electrode in the middle of a irradiation cycle, which can't be explained.
Also current measurements were done, reaching a maximum current of around $-8.66 \cdot 10^{-6}$ A for the down left electrode. This corresponds to a current density of $-7.95 \cdot 10^{-2}$ mA/cm^2. Furthermore, sample PK016 was annealed after the measurements at 1000°C for five hours to see if any improvements can be achieved. After the annealing process meaningful measurements were no longer possible. This was most likely due to delaminations of the different layers because of different thermal expansion coefficients.

Reference sample PK018 showed very consistent results and substantial photovoltaic responses for all electrodes. The deposition rate measurements indicated similar values as for sample PK001 and PK016. The impedance spectra look similar for all three electrodes. Exemplary spectra contacted on the down left electrode are shown in figure 4.43. On the left, spectra in the dark and under UV light irradiation are shown. The answer of the low frequency semicircle under UV light irradiation indicates that photovoltaic voltages can be expected. On the right, temperature dependent spectra are shown, with a behaviour as for PK004 and PK012. In accor-

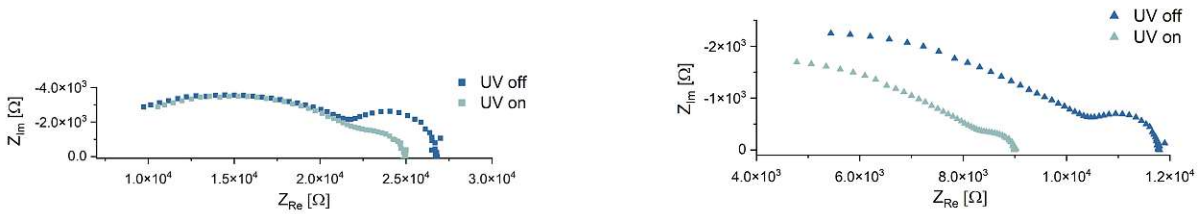

Figure 4.41: Impedance measurements of sample PK016 in the dark and under UV irradiation. Left: Contacted on the down left electrode. Right: Contacted on the up right electrode.

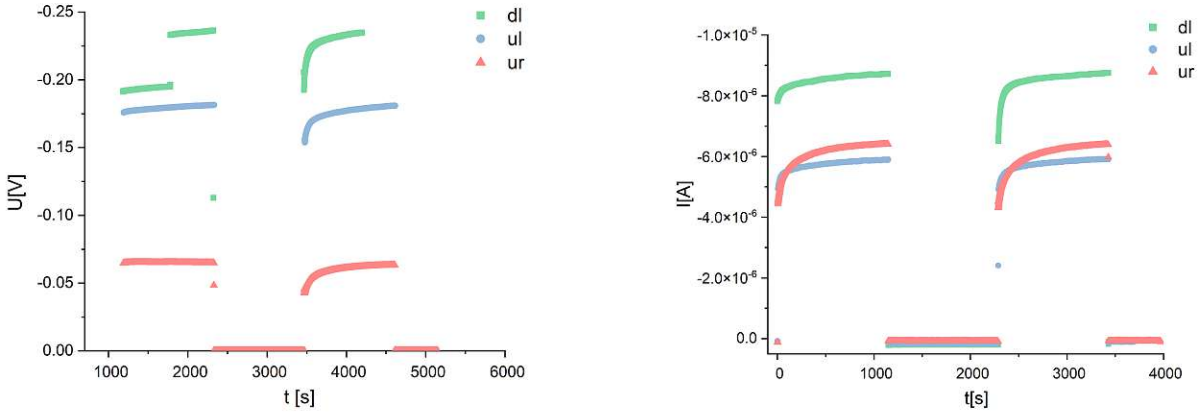

Figure 4.42: Left: Voltage measurements of PK016. Right: Current measurements of PK016.

dance with the similar impedance spectra, also similar photovoltaic voltage values resulted. The maximum voltage measured was -530 mV on the down left electrode. The maximum current measured was -1.13 $\cdot 10^{-5}$ A on the up left electrode. This results in a current density of -1.03 $\cdot 10^{-1}$ mA/cm^2. Figure 4.45 shows the voltage and power density measured against the current density. This data was collected by applying a bias voltage up to the reached photovoltage and measuring the resulting current. A peak power density of 16.05 μW/cm^2 was reached at an applied voltage of -176 mV and a corresponding current density of -91.57 μA/cm^2.

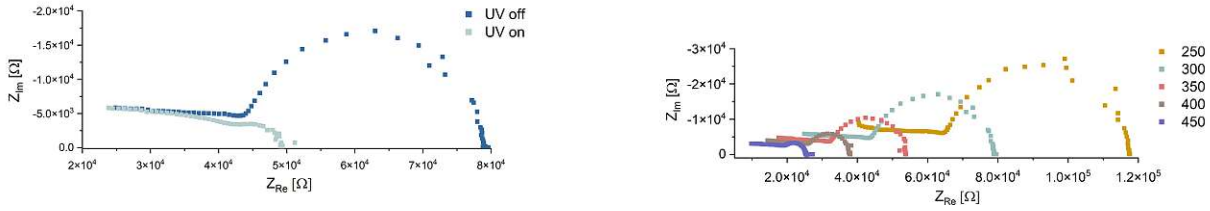

Figure 4.43: Impedance measurements of sample PK018 contacted on the down left electrode. Left: In the dark and under UV irradiation. Right: Temperature dependent.

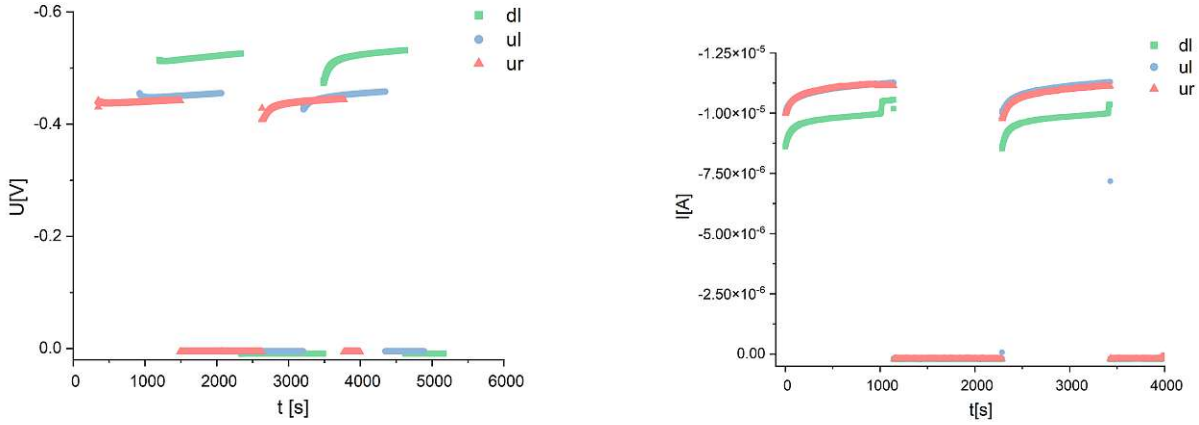

Figure 4.44: Left: Voltage measurements of PK018. Right: Current measurements of PK018.

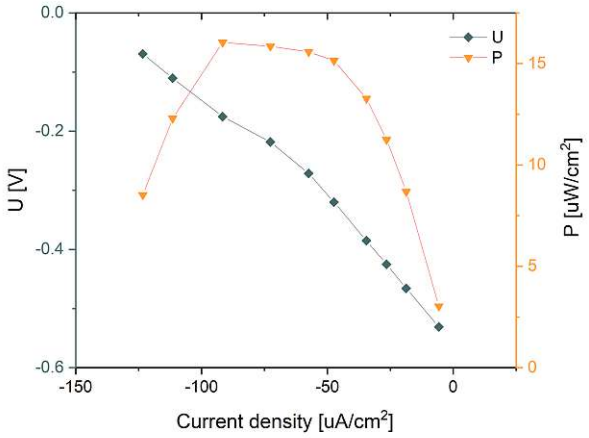

Figure 4.45: Voltage and power density against current density measured with applied bias voltage for PK018.

Reference samples PK021 and PK023

During the preparation of sample PK021, not just the displayed heating temperature changed, also a sudden jump in laser energy was observed after the preparation. This lead to a higher fluence (about 1.13 J/cm^2) and thus a higher deposition rate (0.026 nm/pulse) used for this sample. As shown in figure 4.46, a small answer to UV light irradiation can be observed at 300°C when contacted at the up right electrode. In figure 4.47 measurements at 100°C were performed. The characteristic low frequency feature was observed, also changing with UV light irradiation. A voltage of about -100 mV was measured.
Reference sample PK023 showed an untypical behaviour, exemplary shown in figure 4.48. The voltage measurement on the right showed a negligible answer to UV light irradiation.

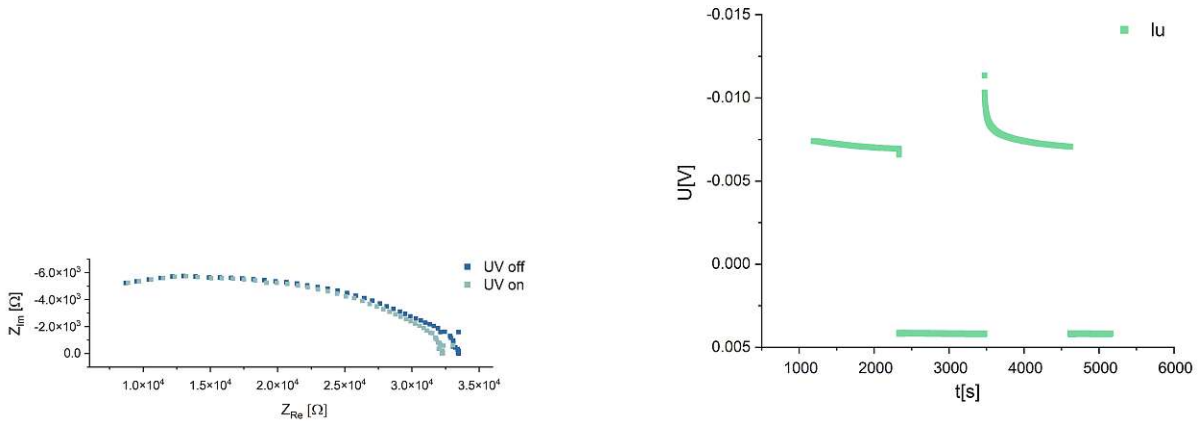

Figure 4.46: Impedance and voltage measurements of sample PK021 at 300°C contacted on the down left electrode.

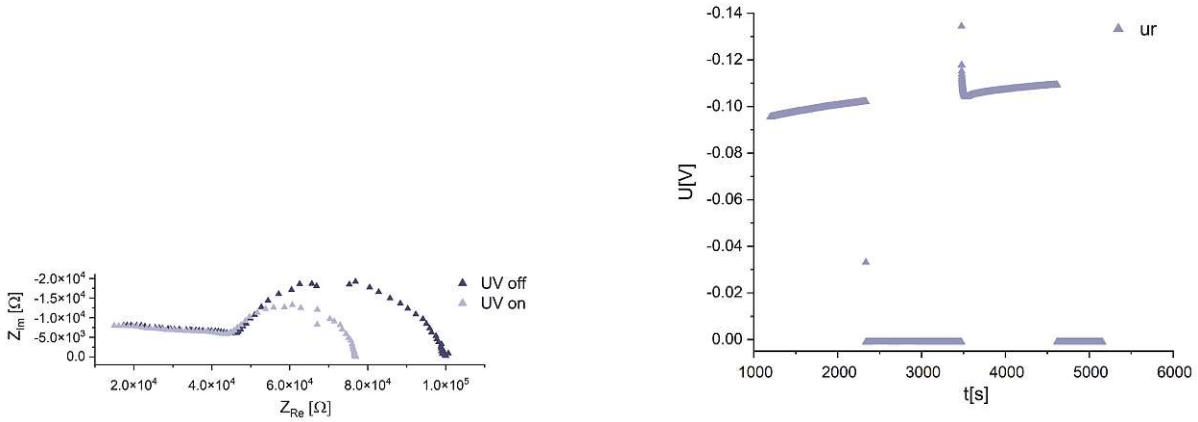

Figure 4.47: Impedance and voltage measurements of sample PK021 contacted on the down left electrode at 100°C.

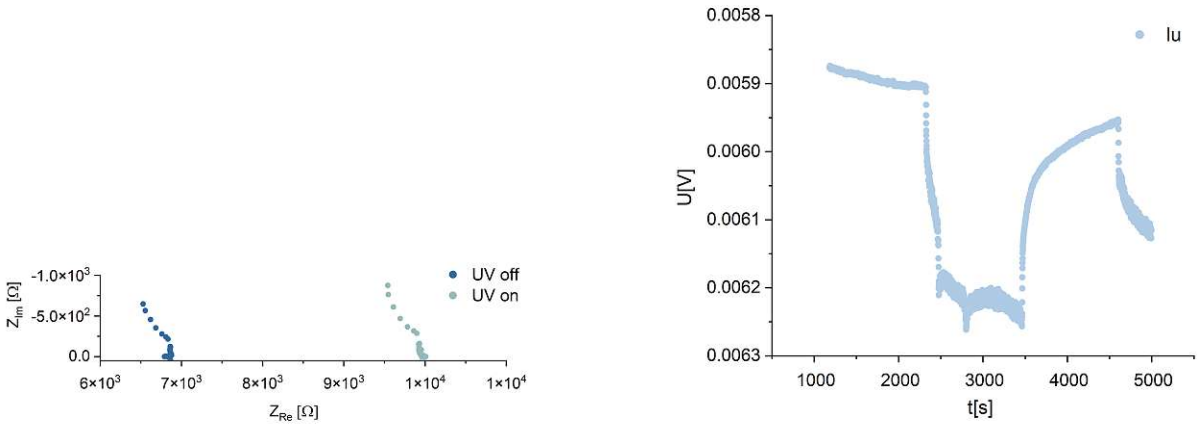

Figure 4.48: Impedance and voltage measurements of sample PK023 contacted on the up left electrode

4.7 15% Sr excess

For a further measurement series, the Sr excess in the target was further increased. This was done because of the varying results of the reference samples. We assumed a limited stoichiometry window, where the Fermi level is not pinned, and a frequent fall back into the pinning state if the stoichiometry is just slightly off, resulting in no voltage. We thus tried to better meet this window with more Sr in the target, what should lead to more Sr in the deposited thin film. The target was prepared as described in subsection 3.2. The first target prepared was brittle. It broke after the first deposition of sample PK022. The remained parts were morsed, pressed and sintered again, resulting in a more dense and stable target structure. Before this batch of samples was prepared, an observation regarding the PLD process was made. The displayed heater temperature showed significantly lower temperatures. As some rebuilds were done before, the assumed reason of that behaviour is an accidental displacement of the thermocouple. The PLD process was continued with the same heating power percentages set as before (see table 1).
Sample PK022 was prepared with the first produced 15% Sr excess target, before it broke. No notable results were achieved. Exemplary impedance and voltage measurements are shown in figure 4.49. A very small answer to UV light irradiation can be observed.

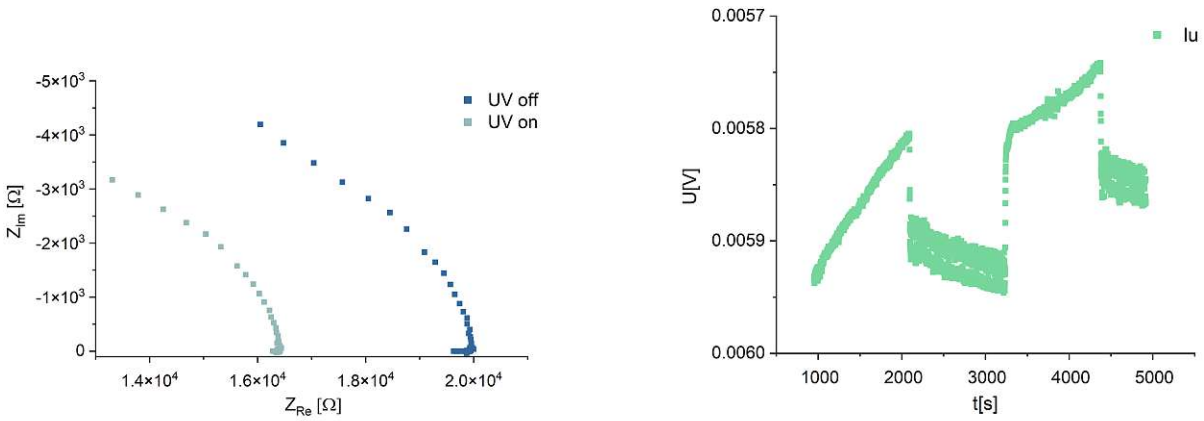

Figure 4.49: Impedance and voltage measurements of sample PK022 contacted on the down left electrode.

Samples PK026-PK028 and PK031 were prepared with the reproduced target. For samples PK026-PK028, Mateck STO single crystals were used as substrates, except from PK031, where (as for earlier sample series) a Crystal STO substrate is used. No sample yielded notable photovoltages. Sample PK026 and PK027 showed an increasing impedance when irradiated with UV light, with a semicircle like shape for high frequencies, and no recognisable voltage answer while irradiated with UV light. Exemplary impedance and voltage measurements are shown in figure 4.50 for PK026 and figure 4.51 for PK027.
Sample PK028 showed a decreasing impedance while irradiated with UV light (figure 4.52 on the left). The voltage measurement shown in figure 4.52 on the right shows a very small but observable change of voltage during irradiation.
Sample PK031, deposited on a both side polished Crystal STO substrate, showed noticeable results, if compared to the other samples prepared with the 15% excess target. The impedance measurements depicted in figure 4.53 show a mid to low frequency feature, which seems to be an overlap of a smaller and a larger semicircle. It looks similar to the one observed on sample PK004 at the up left electrode (see figure 4.9 b)). However, compared to PK004, very different effects of UV light irradiation can be observed. The presumed space charge low frequency feature changes much less for PK031 than for PK004, where it almost fully collapses. The temperature

dependent impedance measurements show a decrease in impedance when increasing the temperature.
The voltage values measured reached a maximum of around 23 mV and are shown in figure 4.54. The positive polarity, however, indicates different mechanisms. Also, the voltage decreases over time and UV light cycles.
The LASIL measurements done for 7% and 15% targets revealed a Sr deficiency for both thin film. The thin film deposited with the 15% Sr excess target (PK029) even shows a higher Sr deficiency than the 7% target. This result may explain the outcome of the 15% Sr excess targets, as the STO thin films seem to have a pinned Fermi level, not building a space charge zone at the junction to the LSCr top electrode.

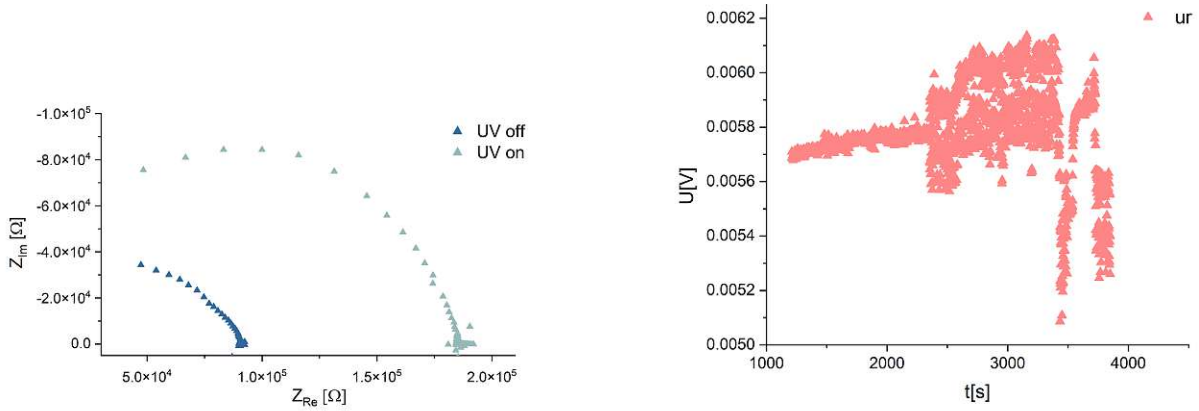

Figure 4.50: Impedance and voltage measurements of sample PK026 contacted on the up right electrode.

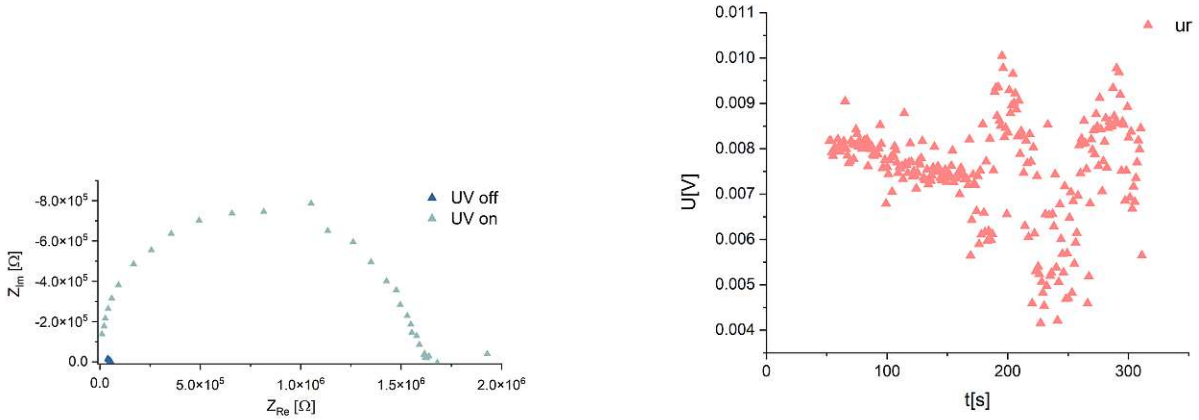

Figure 4.51: Impedance and voltage measurements of sample PK027 contacted on the up right electrode.

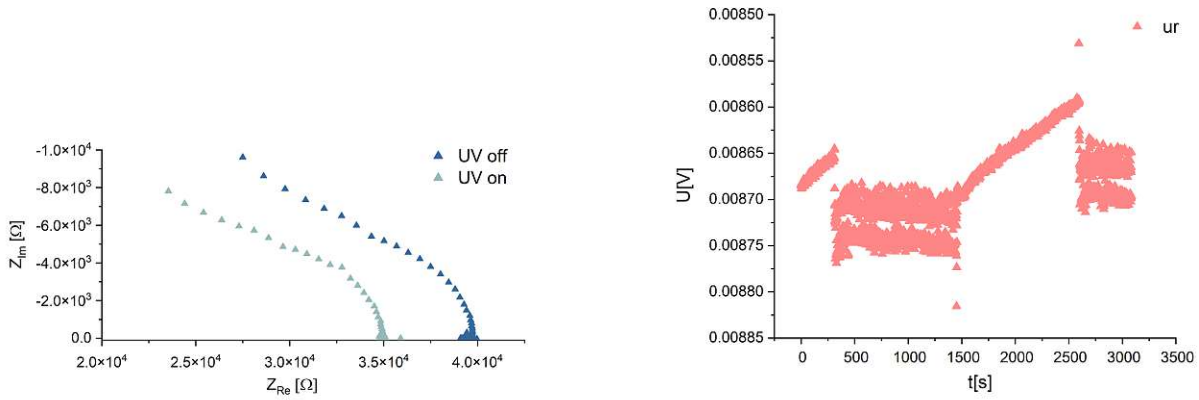

Figure 4.52: Impedance and voltage measurements of sample PK028 contacted on the up right electrode.

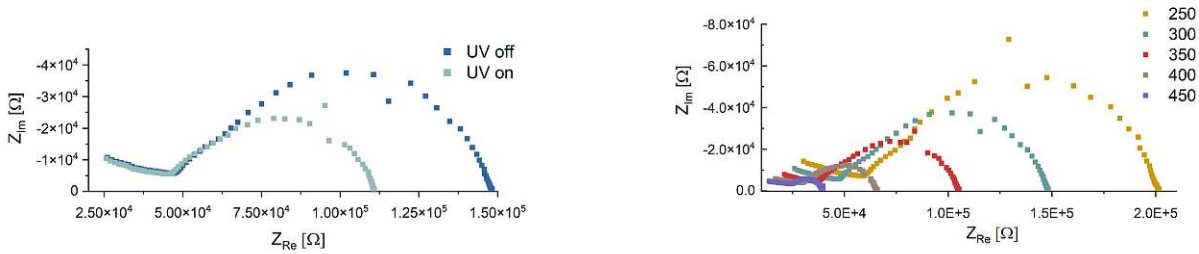

Figure 4.53: Impedance measurements of sample PK031 contacted on the down left electrode. Left: In the dark and under UV light irradiation. Right: Temperature dependent.

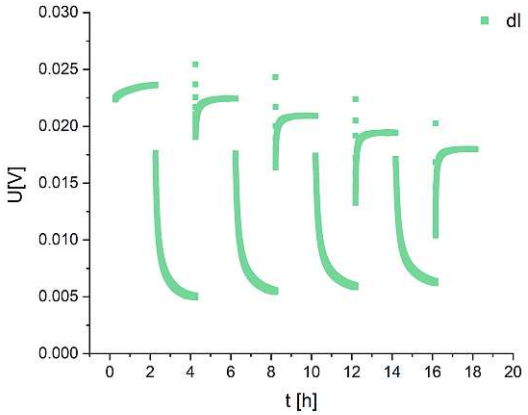

Figure 4.54: Voltage measurements of sample PK031 contacted on the down left electrode.

Observations regarding substrate supplier change

Although we assumed similar behaviour for different substrate suppliers, there seem to be differences. Sample PK021 was prepared with an CrysTec STO substrate, PK023 with an Mateck STO substrate. Already from a purely optical view, the Mateck single crystals, also used for following samples PK024-PK028, yielded films with low quality. Almost every sample showed cracks after the PLD processes. This could be due to a slightly deviating substrate size, leading to a bad fit in the substrate/sample holder inside the PLD. Tensions can then occur while heating and cooling processes, leading to cracks. Those cracks could influence the elechtrochemical properties as well as the measuring process of them.
Furthermore, surface changes could be observed for samples PK023, PK026, PK028, showing darker and brighter areas, depicted and marked in figure 4.55 on the right. A closeup of PK023 is shown on the left. This is also assumed to be due to the different substrate and the corresponding deviation in substrate size. If the substrate is lying in the substrate holder with a small angle, the layer growth changes over position and time, resulting in different thicknesses and surfaces. This is far from ideal for the samples, as the results reflect. This deviations are hard to observe optically during the preparation process. The data yielded from sample PK031 confirm the assumption, that the Mateck substrate is most likely the reason for the unsatisfying sample outcomes.

Figure 4.55: Optical observation of the samples. Left: Close up of sample PK023. Right: Overview of the prepared samples with marked darker surfaces of PK023, PK026 and Pk028.

4.8 Interpretation of impedance spectroscopy and time dependent voltage and current measurements

Taking a closer look at the impedance spectra, it is hard to correctly attribute all the observed features to their origin. The low frequency feature observed in every sample with reasonable photo-voltages under illumination is assumed to originate from a space charge region, which emerges at the LSCr top electrode/STO thin film junction. The photo-active heterojunction between STO single crystals and LSCr is known [10] and seems to appear also for STO thin film/LSCr thin film heterojunctions. The fact, that the low frequency feature collapses under UV light irradiation supports this assumption of a space charge region. Such a behaviour was already observed by Brunauer et al. [10] and Morgenbesser et al. [33].

To further analyse this assumption, the low frequency feature of sample PK004 (dl electrode) was fitted with an R-CPE element (depicted in figure 4.56), resulting in the corresponding resistance, capacitance and thickness of the assumed space charge region. To calculate the thickness of the space charge region, equation 4.1 was employed. For ε_r, the value of STO at the corresponding temperature of 300°C was used, which is around 170 [51]. We assumed that the current flows through the sample the shortest way, thus the LSCr electrodes area is assumed to be the relevant area ($A = 9 \cdot 10^{-6}\,\mathrm{m}^2$). The used value for the vacuum permeativity ε_0 was $8.85 \cdot 10^{-12}$ F/m. A space charge thickness of ∼373 nm was calculated. With a fitted resistance of ∼125 kΩ and the thickness of 373 nm the area-specific resistance of the space charge region ρ_{SC} results in ∼3 MΩm.

$$C_x = \varepsilon_0 \cdot \varepsilon_{r,x} \cdot \frac{A}{d_x} \tag{4.1}$$

$$\sigma_x = \frac{1}{R_x} \cdot \frac{d_x}{A} \tag{4.2}$$

$$\rho_x = R_x \cdot \frac{A}{d_x}, \qquad \rho_x = 1/\sigma_x \tag{4.3}$$

Using the measured voltage of around 688 mV ($\Delta\varphi$) from the dl electrode of sample PK004, the area-specific resistivity of the STO thin film ρ_{STO} can be calculated from equation 4.4 and results in 7.4 kΩcm.

$$\frac{\rho_{SC}}{\rho_{STO}} = \frac{exp(\frac{e\Delta\varphi}{kT})}{\frac{2e\Delta\varphi}{kT}} \tag{4.4}$$

With equation 4.3, the conductivity of the STO thin film would result to $\sigma_{STO} = 1.34 \cdot 10^{-4}$ S/cm. Comparing that result with a conductivity value of a undoped STO single crystal at around 250°C-300°C, which was extrapolated to around $3 \cdot 10^{-4}$ from [18], it fits well. If calculating the other way around, with the extrapolated conductivity of bulk STO, a space charge potential of around 730 mV results. If those results are assumed to be right, the STO thin film has indeed a bulk like conductivity.
Additionally, the space charge potential $\Delta\varphi$ was calculated for an estimated intrinsic conductivity of the thin film ($\sigma_{\mathrm{STO,int}} = \sim 10^{-10}$ S/cm) and with an estimated conductivity value measured for Fe doped STO thin films ($\sigma_{\mathrm{Fe:STO}} = \sim 10^{-6}$ S/cm), both calculated Morgenbesser et al. [19]. The area specific resistance can be calculated from the conductivity as in equation 4.3 and the corresponding space charge potential $\Delta\varphi$ results from equation 4.4 [52]. T is the temperature of 300°C, thus 573.15 K, e is the elemental charge $1.602 \cdot 10^{-19}$ C and k the Boltzmann constant $1.38 \cdot 10^{-23}$ J/K. For the intrinsic specific resistance, the ρ_{SC}/ρ_{STO} ratio gets close to zero, thus leading to a meaningless result, or no space charge potential, respectively. The estimation with the Fe doped STO thin film conductivity results in a space charge potential of around 422 mV. The results of all these approximations support the assumption that the observed low frequency feature originates from a space charge region.

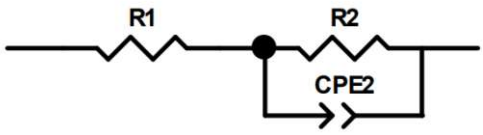

Figure 4.56: Equivalent circuit used for the fit of the low frequency feature. The resistance R1 sets an offset for the R-CPE feature and has no physical background.

As we also don't know the real stoichiometry or doping of the deposited STO thin film, the dopant concentration N can also be calculated from equation 4.5, when assuming the space charge thickness d_{sc} follows the behaviour of an electronic Schottky barrier [51, 53]. The thickness of the space charge zone was calculated above to d_{sc}=373 nm, $\Delta\varphi$ is 688 mV. The acceptor concentration thus results in $N = 9.29 \cdot 10^{-17}$ cm^{-3}, which is again a possible value for an undoped bulk like film.

$$d_{sc} = \sqrt{\frac{2\varepsilon_0\varepsilon_r|\Delta\varphi|}{e \cdot N}} \tag{4.5}$$

The time dependence seen in most of the voltage measurements, especially when first irradiated, can be explained by an additional battery potential built due to a time dependent oxygen vacancy enrichment inside the STO thin film, described in subsection 2.2.2. Until an equilibrium of chemical potentials is reached, the measured voltage can change. Additionally, due to the LSCr electrodes absorbing some of the UV light, the process can happen faster or slower inside the STO thin film, leading also to changed chemical potentials inside the STO thin film. In comparison to the STO single crystal based samples, the voltage drops immediately to zero after switching off the UV light, which might be due to the fact, that the whole thin film is activated through the UV light. Thus after a certain amount of time, no inner chemical potential differences, which can cause a battery voltage, are present. Similar oxygen stoichiometry polarisation effects most likely also cause the time dependence of the current measurements.

4.9 TEM & SEM

TEM images were taken for sample H014, which was prepared before starting this thesis. The sample was prepared in a similar way as the described standard sample, thus giving interesting insights of the thin film growth. In figure 4.57 a) a overview cross section of the sample is depicted, in b) a closer look on the LSCr/STO thin film junction, in c) the STO thin film/LSC junction and in d) the STO thin film.
It can be observed that the layer growth seems to be very good. No degradation can be seen.

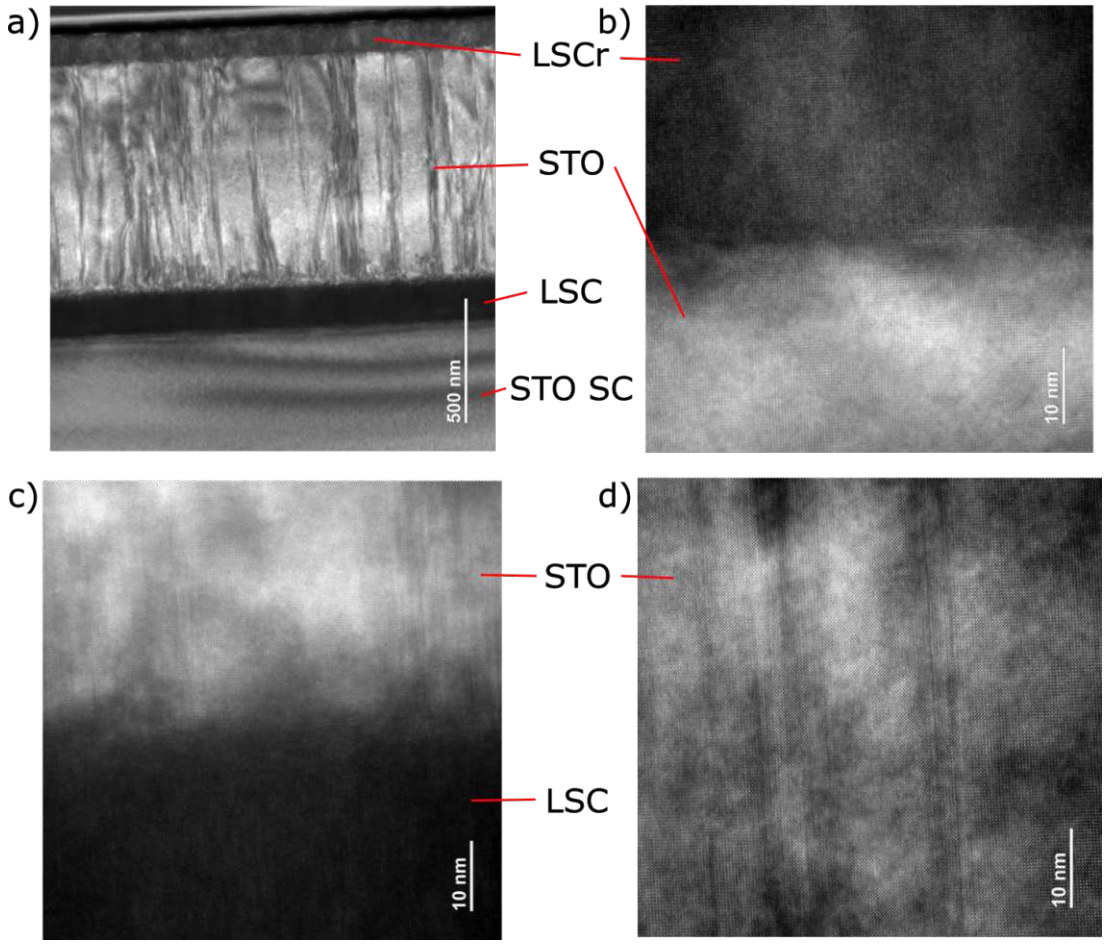

Figure 4.57: TEM images of sample H014, prepared before this thesis in a similar way. a) cross section overview of the layer system. b) LSCr/STO thin film junction. c) STO thin film/LSC junction. d) STO thin film.

SEM images were also made for sample PK004 and sample PK013. It was investigated whether there are any surface differences between well working samples like PK004 and not working samples like PK013. Figure 4.58 displays the surface of sample PK004 and figure 4.59 shows the surface of sample PK013. A very interesting and clear difference can be observed. Sample PK004 shows a rather homogeneous surface, with just some "square" features. PK013, on the other hand, exhibits a high density of "triangular" features and a more textured underlying surface ("squares") compared to PK004.
Bright field TEM cross section, selected area diffraction as well as an overview EDS of sample PK013 revealed that the triangle and square features are both $SrTiO_3$, but with different orientations. The STO thin film layer seems to grow epitaxial for the first 200-300 nm, then starts building islands. The square features turned out to be large grains with the same orientation as the rest of the thin film, whereas the triangular features are oriented

differently. Pictures of the cross section are shown in figure 4.60. The results of the selected area diffraction are given in figure 4.61.
Furthermore, the EDS map revealed no significant chemical inhomogeneities in the films. The three different thin films can be clearly seen in figure 4.62. Additionally, when looking at the overview picture in figure 4.62 on the left, a porosity between the colonial grown parts and the square and triangular features can be observed. Moreover, all three thin film thicknesses seem to end up thinner than expected from the QCM measurements.
If we assume that the cross section of sample PK004 grew epitaxial and looks similar than the one of sample H014 (figure 4.57), the growth is another indication why samples are hard to reproduce.
The island features could come from the interaction between the laser and the target. Due to the long deposition time of the STO thin film, the target gets an uneven surface with a circular ablation channel. This could lead to a changed deposition behaviour, leading to island features with a different growth orientation. The triangular features could lead to problems between the STO thin film and the LSCr electrode and also probably interfere with the growth of the LSCr thin film on top. The surface roughness from the different grown features could also interfere with the emergence of a space charge region between the LSCr thin film and the STO thin film. Due to the large grains, it is possible that space charge regions, which originate at those grain boundaries, start to overlap, changing the electrical conduction properties [54, 55]. These two possibilities would thus interfere with a potential photovoltage generation at that heterojunction. The Sr deficiency might also plays a role, leading to a non-epitaxial growth.
The deposition process probably makes the biggest difference, whether a sample shows a photovoltaic response or not. If the STO thin film has a dense micro-structure, it seems more likely to get photovoltages, as a space charge region can emerge. The stoichiometry of the film seems to be an additional factor that comes to play.

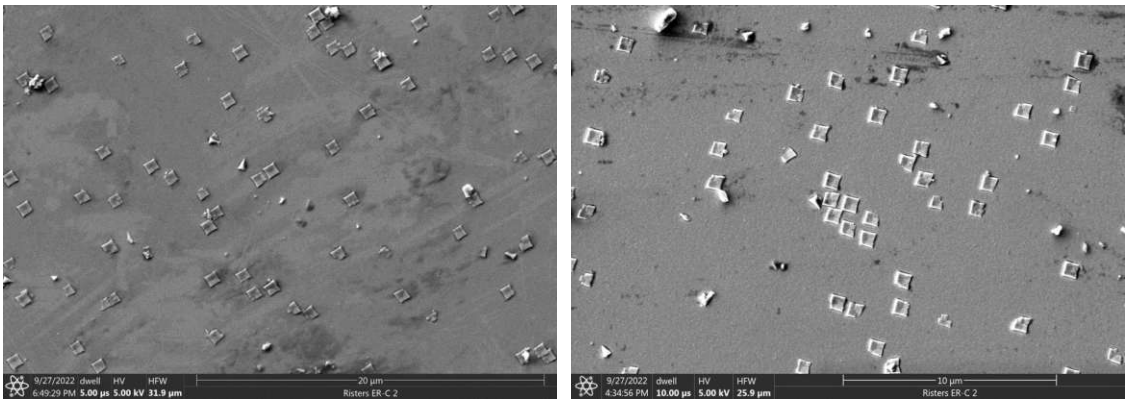

Figure 4.58: SEM images of the surface of sample PK004.

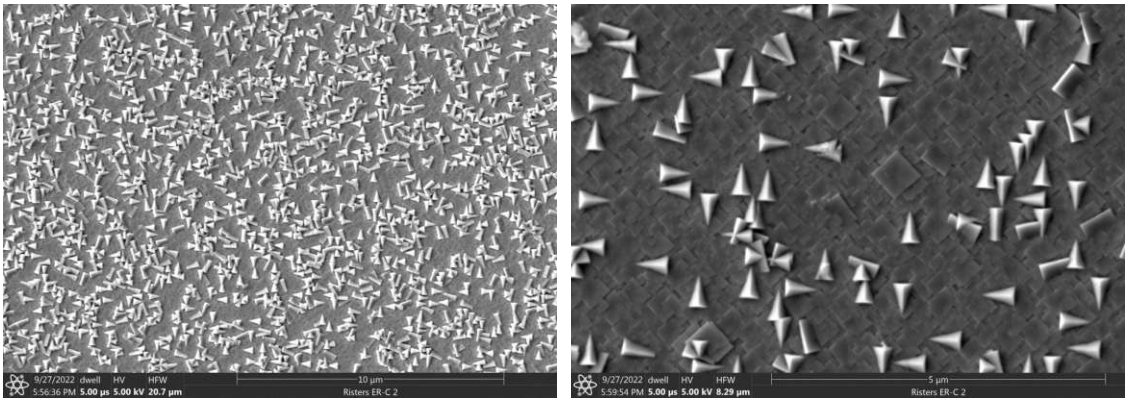

Figure 4.59: SEM images of the surface of sample PK013

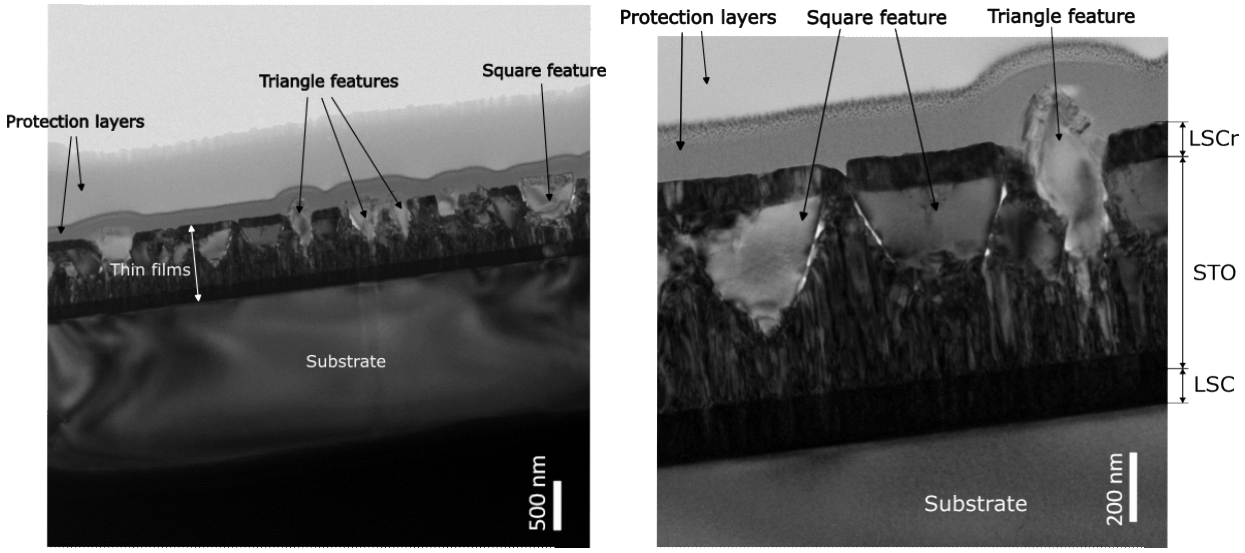

Figure 4.60: Bright field TEM cross section of sample PK013.

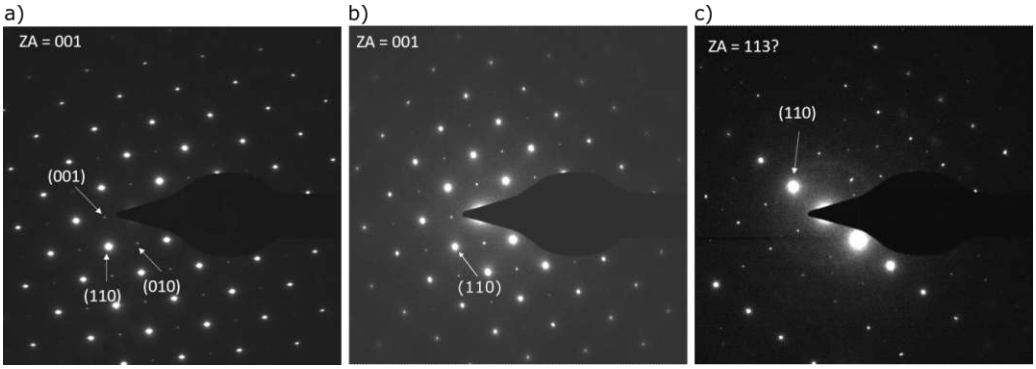

Figure 4.61: Selected area diffraction of different parts of sample PK013. a) thin film, b) square particle, c) triangular particle.

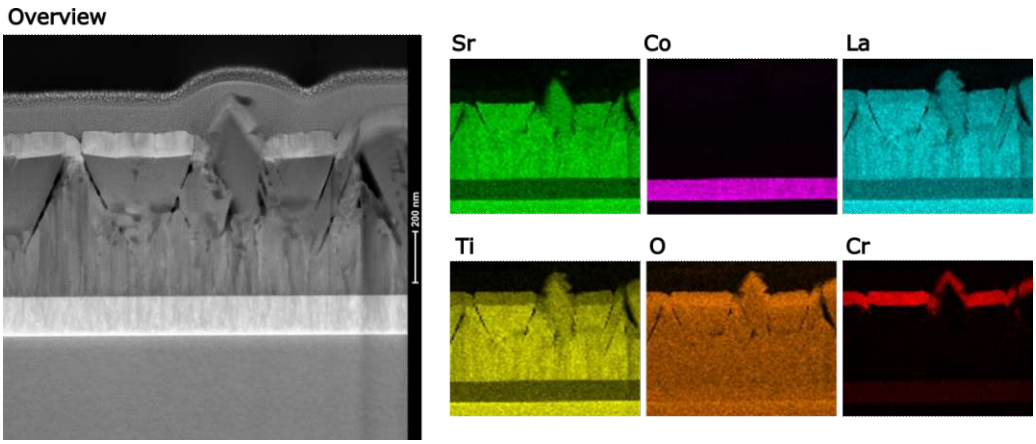

Figure 4.62: HAADF STEM EDS mapping results. The maps of La and Ti share EDS peak locations, thus they look the same. La should be in the LSC and in the LSCr layer.

4.10 LASIL-ICP-MS stoichiometry analysis and LA-ICP-MS depth profiles

Depth profiles of different samples were taken with LA-ICP-MS during this work, trying to get a better insight into the composition of the samples. In figure 4.63 the Ti/Sr ratio of the measured samples are summarised. As there is Sr in every layer, it is hard to evaluate the stoichiometry of the STO thin film. Also, the shown data is raw, representing just the quantitative counts measured. By looking at the plot, three areas can be observed. The first is attributed to the STO thin film, the second to the LSC counter electrode and the third to the STO bulk. Similar Sr/Ti ratios of the thin film and the substrate are found for almost every sample, except sample PK009. PK009 is the sample which was prepared with the undoped STO target (STO 0%). One can assume, that the thin films deposited with 7% and 10% Sr excess in the target have a similar stoichiometry than the bulk STO. However, the following LASIL measurements showed different results, but were also performed a few months later.

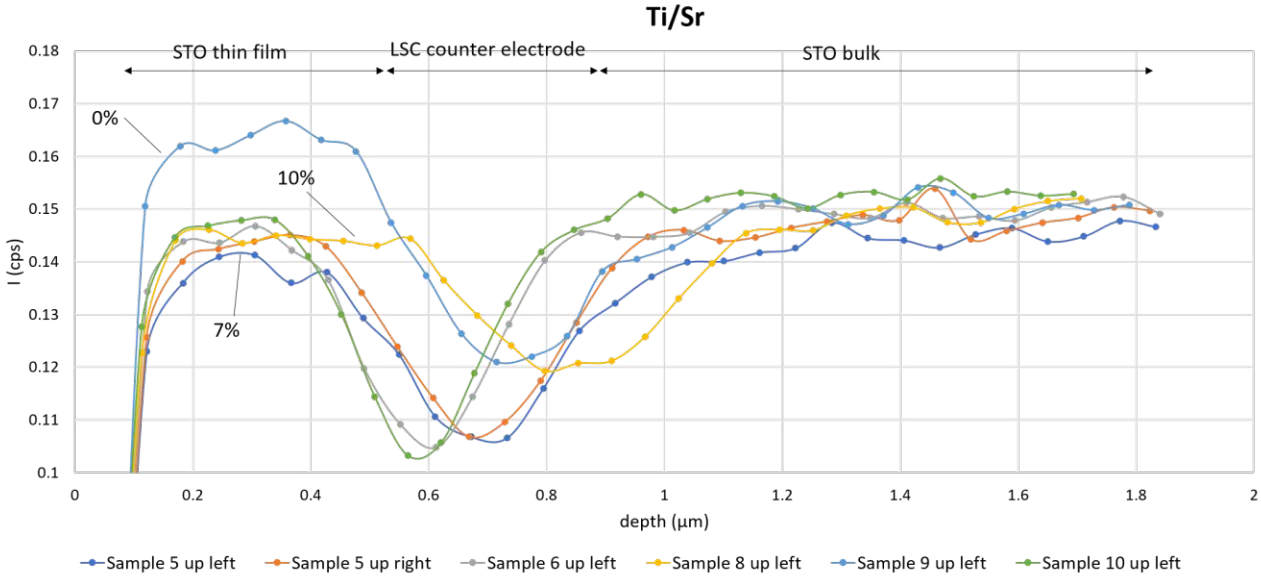

Figure 4.63: ICP-MS depth profile measurements of different samples.

LASIL-ICP-MS measurements of sample PK029 and PK030 were done to check the stoichiometry of the thin films. Both samples were deposited on a sapphire substrate to not distort the Sr/Ti ratio. PK029 was prepared with a 15% Sr overcompensated target, PK030 with a 7% Sr overcompensated target (assumed to lead to stoichiometric films). The measurements shown in figure 4.64 revealed that both films have a Sr deficiency. These results are preliminary results and should be treated with caution. They were done at the end of the work, thus over time changes while preparation have to be kept in mind. The fact that a few samples show a good amount of voltage indicate a stoichiometric STO thin film without a pseudo-intrinsic conductivity.
Nevertheless, the results show, that the ICP-OES measurements done by Morgenbesser et al. in [19] for Fe doped STO targets, revealing a stoichiometric thin film when using a 7% Sr overcompensated target, can not directly be transferred to 7% Sr excess undoped STO targets. Further investigations regarding the stoichiometry of STO thin films are recommended.

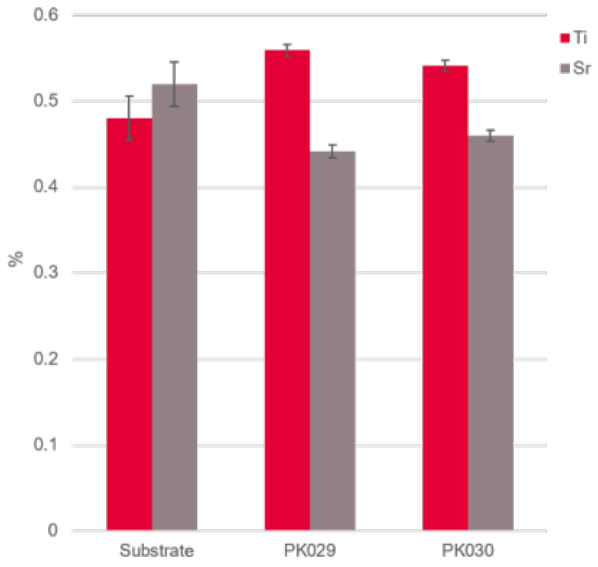

Figure 4.64: LASIL Measurements, the substrate corresponds to a undoped STO single crystal, PK029 to a STO thin film prepared with a 15% Sr excess target and PK030 to a STO thin film with a 7% Sr excess target.

4.11 General observations and discussion

Observations regarding the preparation and measuring processes are summarised in this subsection. Figure 4.65 summarises photovoltaic voltages and short circuit current densities of all samples measured. For each sample the best electrode is shown. It is obvious that a pronounced variability of properties is found. The best results were obtained with a STO 7% target, a fluence of $\sim$1 J/cm^2 and a film thickness of around 840 nm. Four out of ten identically prepared samples using these parameters showed voltages above 200 mV. However, the reproducibility of STO thin film solar cells is still rather limited due to different factors. The key factor for obtaining well-performing photovoltaic cells seems to be a combination of the PLD process and the thin film stoichiometry. If the thin film has a Sr deficiency, an ultra low pseudo-intrinsic conductivity results, as described in subsection 2.1.2 [20]. When this happens, the Fermi level of the LSCr top electrode and the STO thin film seem to be at a similar level, thus no voltage is generated under UV light. The 7% Sr excess target should balance that Sr deficiency, but as shown in subsection 4.10, also the 7% target can exhibit a Sr deficiency. We suppose that the "working" samples have a stoichiometric thin film (like bulk STO), leading to substantial photovoltages as the Fermi levels are different, like shown in figure 2.7 with a single crystal. This means, that the window between a stoichiometric thin film, a Sr deficiency and too much Sr in the STO thin film seems to be very small, resulting in such a variation in sample results. Additionally, the PLD process is prone to unintended variations, making it even more difficult. There are many different parameters, making it hard to fully reproduce a sample. Besides the set parameters, a few other things can't be controlled completely. The fluence, for example, is calculated by the laser energy in the vacuum chamber and the spot size on a target. The laser energy, however, seems to vary in a certain range, making it hard to control, especially for longer deposition times like the one of the STO thin film (up to 90 min). Additionally, the spot size is measured just under a microscope, where also mistakes can happen due to an often not clearly visible borderline of the area. The fluence thus is a parameter, which can change pretty likely over time.
Also the deposition rate has to be treated with caution, as the QCM can change in height unrecognisably, leading to wrong results. It is though helpful to measure both of the mentioned parameters, as the comparison can give a good estimation of the current fluence/deposition rate. If the deposition rate shows much higher values than normal, the fluence might be wrong. The results obtained by TEM and SEM revealed a different micro-structure for bad and well performing samples (section 4.9). The bad performance could come from the island growth, hindering the formation of a space charge region. The island growth could be caused by interaction between the laser and the target. Due to the long deposition time of the STO thin film, the target gets an uneven surface with a circular ablation channel. This changed surface could lead to a changed deposition behaviour, leading to different growth orientations and island growth. Furthermore, the target position can vary, which could also lead to deposition changes over time. The targets are often hard to fully fix in the target holder. The mentioned substrate supplier change also seems to be a clear indicator of problems. A close look at the fit of the substrate in the substrate holder is recommended to avoid low performing thin films. These results highlight the fact that the preparation poses most of the problems.
Furthermore, the resistances per area of the low frequency features in the dark were compared for all samples exhibiting a reasonable photovoltage. Additionally, the resistance ratio between the low frequency feature in the dark (R_{Dark}) and the collapsed low frequency feature under UV light (R_{UV}) are compared. Both results are depicted in figure 4.66. The comparison was done for sample PK001, PK004, PK006, PK008, PK009, PK012, PK016, PK018. Samples PK008 and PK009 were prepared with different Sr excess targets, see table 4. No clear correlation between the resistance per area and the measured voltage can be found. Also, the ratio R_{Dark}/R_{UV} doesn't reveal a clear trend whether the magnitude of the collapse of the low frequency feature indicates more voltage. Certainly, though, is that if a low frequency feature is present, which can be assigned to the space charge region and collapses under UV light, photovoltage is generated.

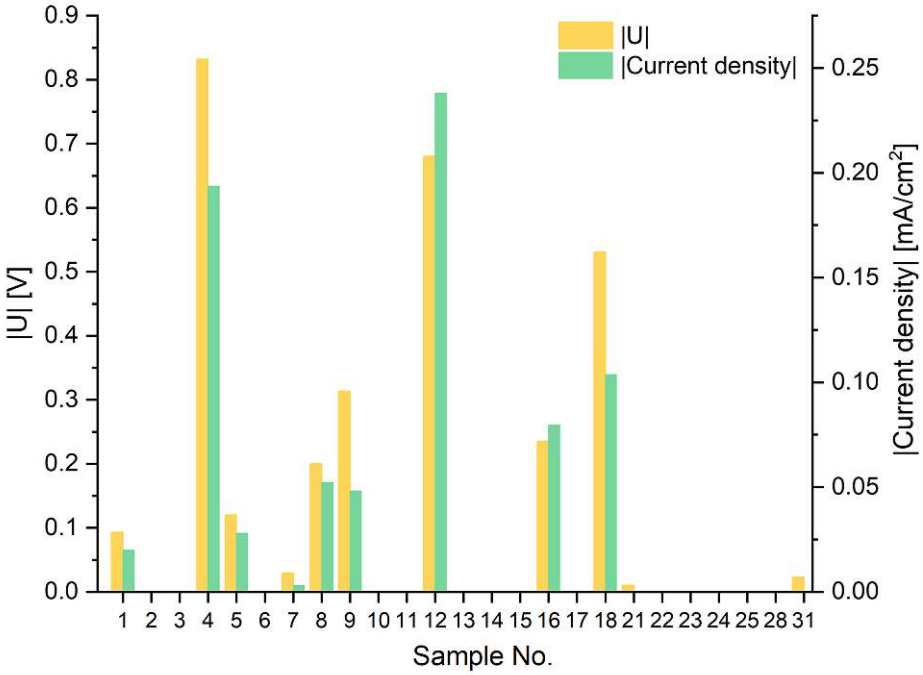

Figure 4.65: Comparison of the photovoltaic voltage and short circuit current densities for all samples measured at 300°C set. For each sample, the highest values are shown. One can see the scatter in gained voltage and current values between the different samples. The samples with Numbers 1, 4, 5, 10, 12, 13, 14, 16, 18, 23 were prepared the same. For the other samples, different parameters like fluence, thickness, deposition temperature or target composition were changed.

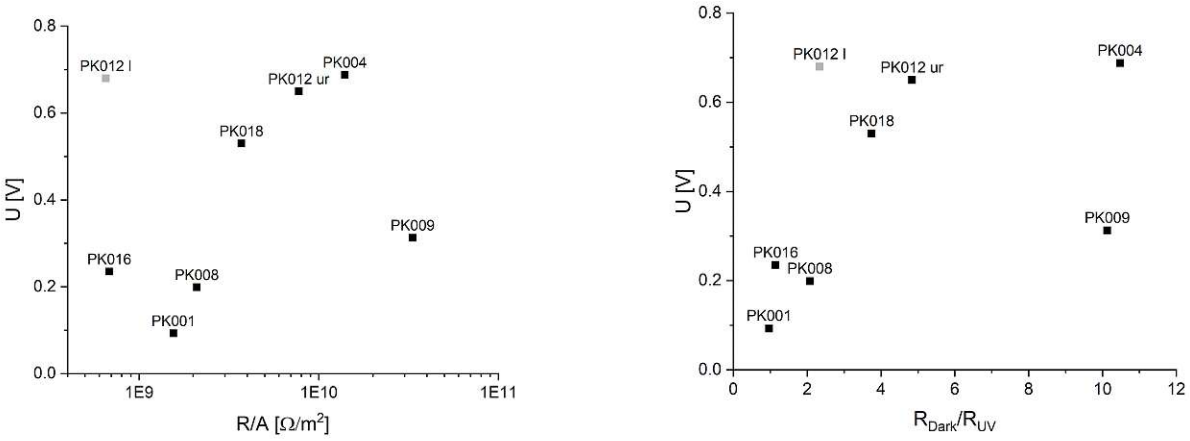

Figure 4.66: Left: Comparison of the low frequency feature resistance per area to the measured voltage. Right: Comparison of the resistance ratio of the low frequency feature in the dark and upon UV light. The grey point marks PK012 contacted on the left electrode, which has a bigger area than the other ones, as described in subsection 3.1. The shown data was measured at 300°C set.

5 Results and Discussion of STO single crystal based solar cells

The STO single crystal based solar cell samples were prepared in order to reproduce and compare results with experiments done by Morgenbesser et al. [19, 20, 22] and L. Enzlberger [14]. Those experiments considered Fe doped and undoped STO thin films on STO single crystals with respect to voltage generation as well as the impact of the used Sr overcompensated targets on the thin film and the photovoltage. The results are discussed in the context of results found in the past (e.g. Fermi level pinning theory [19]). Also, more details regarding the thin film stoichiometry and preparation is aimed at. The topic of thin films deposited on STO single crystals was already discussed in section 2.1. In sum, four samples were prepared as described in subsection 3.1, all with 110-150 nm LSCr on top.

PK019 and PK020 were prepared on undoped $SrTiO_3$ substrates using a stoichiometric STO target for the thin film. For PK019, the thin film is about 300 nm thick, inspired by M. Morgenbesser. PK020 has a thin film thickness of around 840 nm, thus the nominal value of our standard STO thin film used for the thin film based solar cell samples. The impedance data of PK019 revealed a high frequency feature, which is attributed to the STO substrate bulk and a second strongly varying low frequency feature, what could be the space charge as already described in [33] for a STO single crystal/LSCr junction. To confirm the origin of the high frequency feature, it was fitted in a similar way as describes in subsection 4.8. The relative permeability was calculated with the fitted capacitance. A value of $\sim$270 was found, which is a bit higher as the expected value of $\sim$170 found in literature [33, 51] for a temperature of 450°C. The calculated conductivity value results in the range of 10^{-3} S/cm, which is in agreement with data found in [18] for the corresponding temperature. The results thus also suggest that the high frequency feature is the STO bulk, confirming the assignment of [33]. The differences could be due to the not perfect fit of the data. The STO thin film is assumed to be invisible in the impedance spectrum because of its small resistance compared to the bulk. Impedance spectra of the sample contacted on the down left electrode are shown in figure 5.1 for 300°C (a), c)) and for 450°C (b), d)). a) and b) were measured in the dark, c) and d) under UV light irradiation. A clear answer of the low frequency feature to UV light irradiation can be observed. This could again be the mentioned collapse of the space charge, indicating photovoltage.
Voltage measurements on PK019 show high photovoltages for every contacted electrode at 300°C and 450°C depicted in figure 5.2 and figure 5.3. At 450°C the voltage needs a few minutes to reach the maximum when irradiated, then stays almost constant over time and drops to zero with a delay of around 10 minutes when the UV light is turned off. Voltages of over -1 V were reached. The origin of the photovoltage is presumed to come from the Fermi level difference between the STO thin film and the STO single crystal [22]. If compared with the LSCr/STO single crystal junction, where similar amounts of voltage were observed in [10] and [33], the LSCr Fermi level seems to be similar as the one of the STO thin film (pinned), thus leading to a Fermi level difference between the thin film and the STO single crystal (see figure 2.4).
At 300°C, even higher voltages of up to -1.3 V were reached. Interestingly, a voltage remained after turning off the UV irradiation at 300°C. The voltage drops slowly, finding a constant value at about -320 mV, as depicted in figure 5.3 on the left and in figure 5.4. This remaining photovoltage seems to be some sort of battery voltage due to oxygen stoichiometry changes inside the STO, as described in [33] and subsection 2.2.2. Apparently this battery-like voltage does not relax at 300°C. The measurement under synthetic air conditions showed very similar results reaching values of up to -1.4 V at 300°C set, as shown in figure 5.4. Short circuit current measurements were done at 300°C and 450°C and are shown in figure 5.5. At 300°C a current of up to -$4.45 \cdot 10^{-6}$A was reached, the current seems to keep growing until the end of the irradiation. Such a continuous current increase corresponds to the self enhancement effect described by Morgenbesser et al. in [33]. They attributed the time dependent current increase to oxygen stoichiometry changes in STO, which increase over time. This phenomenon is explained in subsection 2.2.2. At 450°C, a current of -$1.8 \cdot 10^{-5}$A was measured. Here, the current seems to be constant over time, with a peak at the beginning. That peak could come from defect chemical and stoichiometric changes, which need to find a equilibrium after the UV light is turned on.

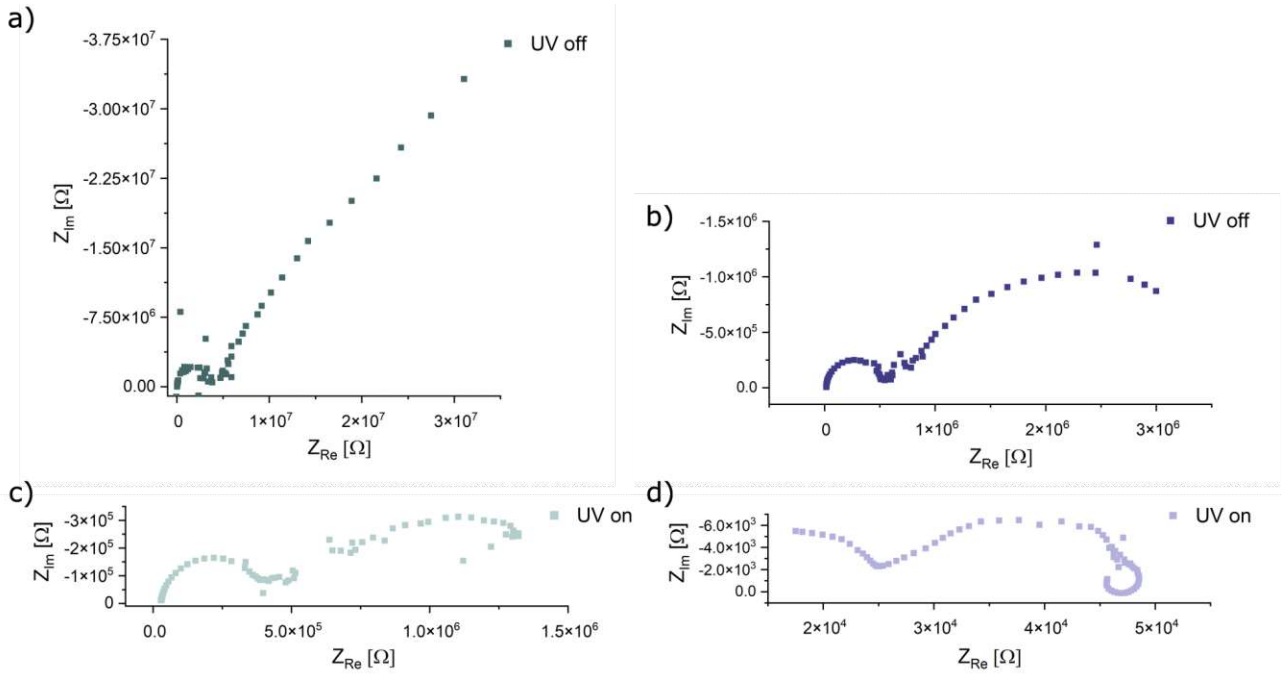

Figure 5.1: Impedance measurements of sample PK019. a) Contacted on the down left electrode at 300°C and in the dark. c) Under UV irradiation. a) Contacted on the down left electrode at 450°C and in the dark. c) Under UV irradiation.

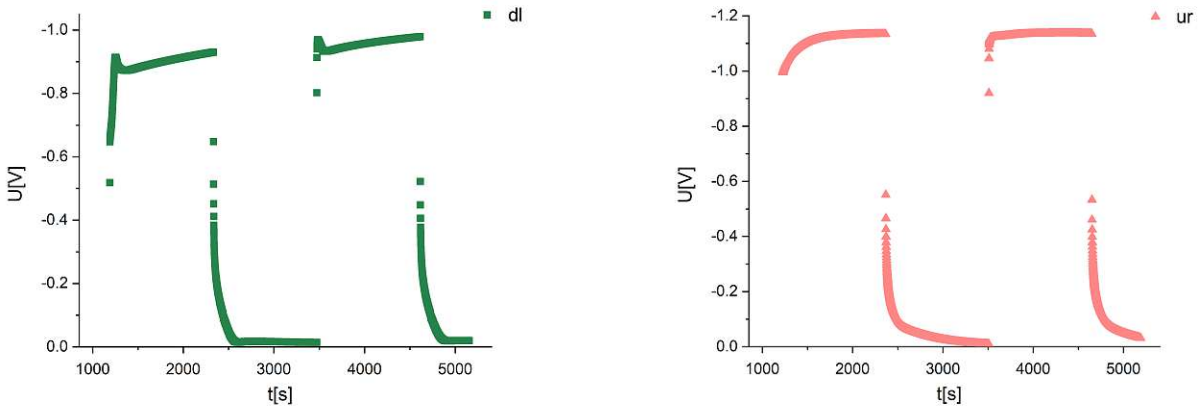

Figure 5.2: Voltage measurements of PK019 at 450°C. Left: Contacted on the down left electrode. Right: Contacted on the up right electrode.

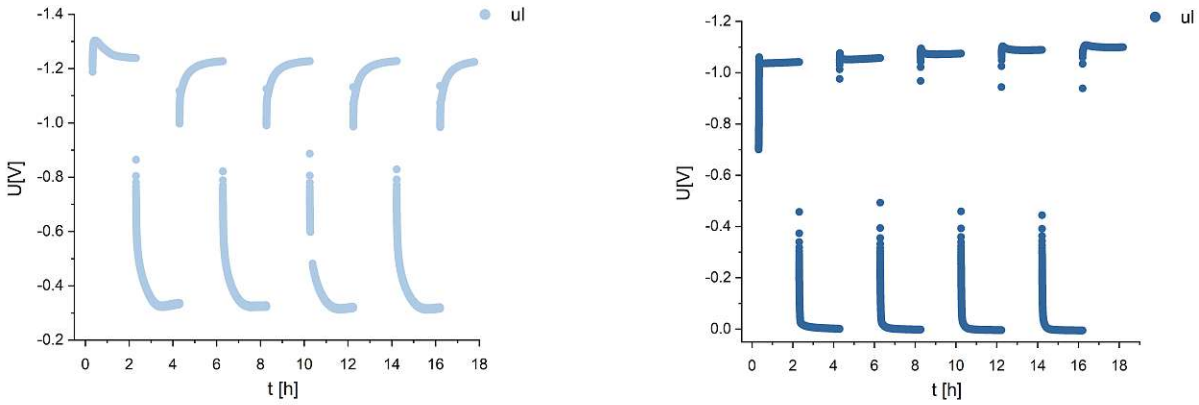

Figure 5.3: Temperature dependent voltage measurements of PK019 contacted on the up left electrode. Left: At 300°C. Right: At 450°C.

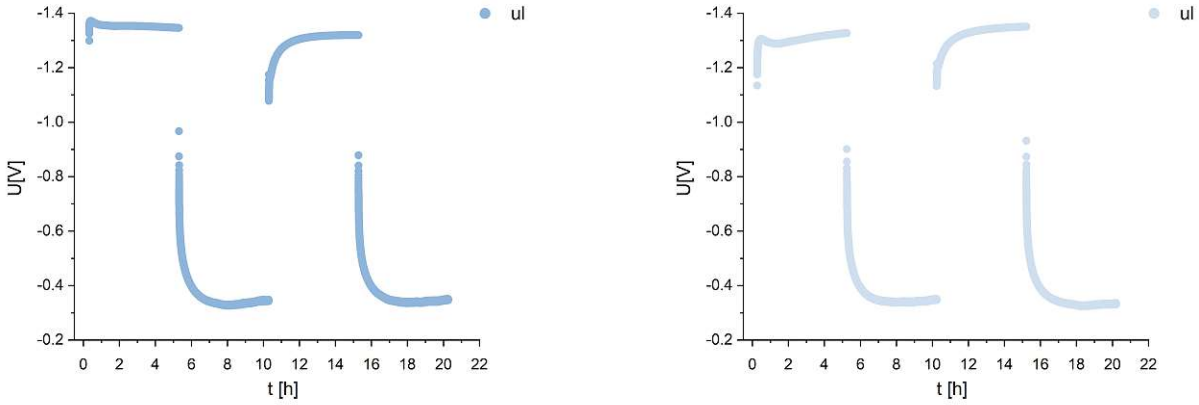

Figure 5.4: Voltage measurements of PK019 contacted on the up left electrode at 300°C. Left: Under ambient air conditions. Right: Under synthetic air conditions.

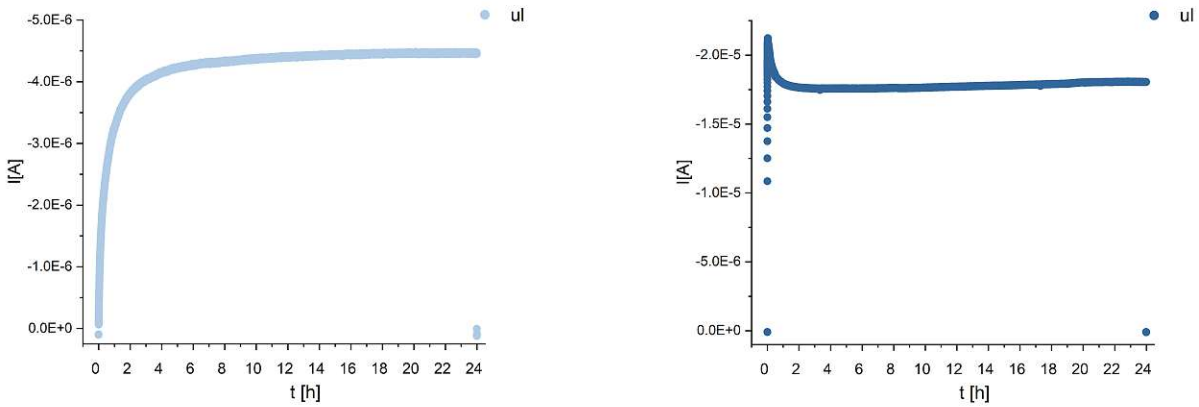

Figure 5.5: Temperature dependent current measurements of PK019 contacted on the up left electrode. Left: At 300°C. Right: At 450°C.

PK020, with a thicker STO thin film, showed similar impedance spectra as PK019, depicted in figure 5.6 for 300°C (left) and 450°C (right). Again, smaller impedance values are observed for higher temperatures as well as the collapsing mid to low frequency features. Also, the STO bulk high frequency feature is observed again. Additionally, impedance spectra measured under synthetic air conditions are compared to ambient air measurements in the dark and under UV light irradiation. Those are depicted in figure 5.7. For 300°C set, no differences can be observed between the two atmospheres, at 450°C, a reduction of the impedance is observed. The measured voltage values show a clear reduction compared to the voltage values measured with the thinner STO thin film sample PK019. Voltages were in the range of about -500 mV or even lower. The change could be a hint to a changing thin film composition and growth, when deposited for a longer time. The voltages measured in ambient and synthetic atmospheres, interestingly, show a reduction of the photovoltage at 450°C set from around -540 mV at ambient to around -200 mV at synthetic air conditions. At 300°C, slightly higher voltages of around -470 mV were measured under synthetic air conditions compared to around -420 mV under ambient air conditions. Here, the measurements at 300°C and under synthetic air conditions seem to show almost no battery voltage and go back to zero in the dark, whereas under ambient air, the voltage almost stays the same. This behaviour may be caused by a highly complex defect chemistry, chemical potential differences or a not known behaviour between the LSCr electrode/STO thin film/STO single crystal structure. It is not further investigated in this work. For this sample, no current measurements were made.

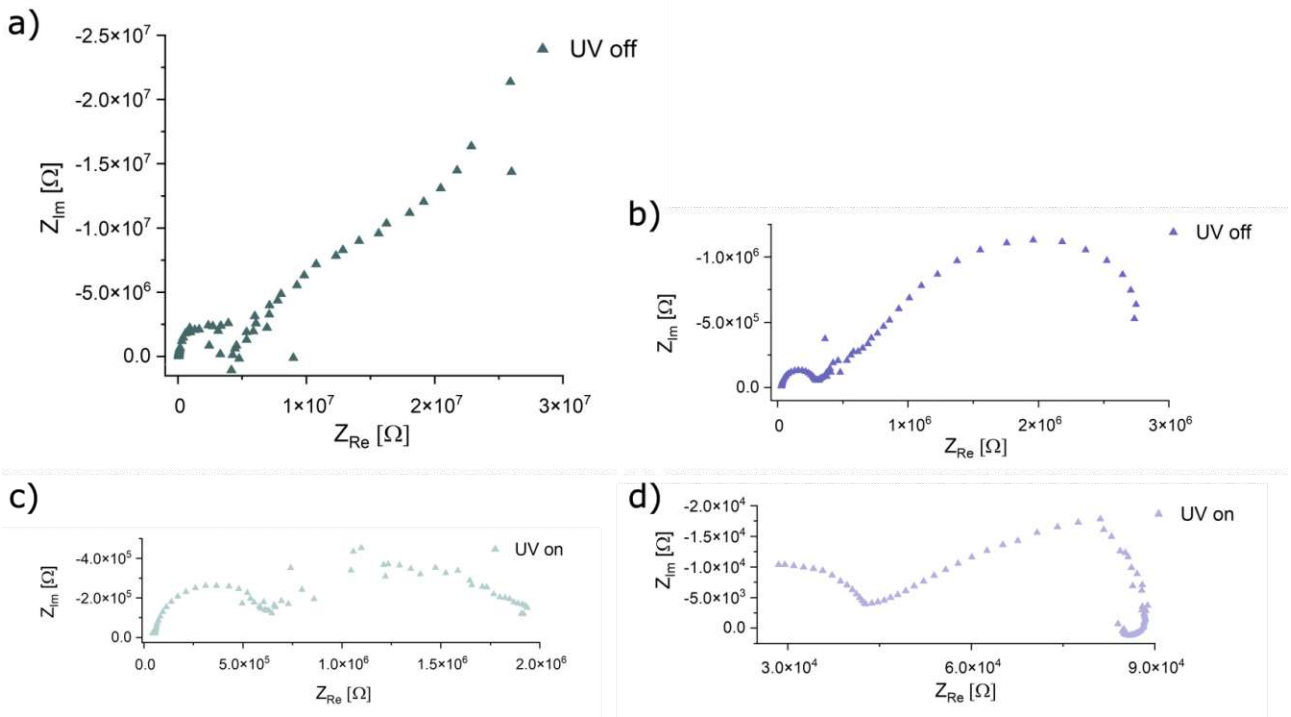

Figure 5.6: Impedance measurements of sample PK020. a) Contacted on the down left electrode at 300°C and in the dark. c) Under UV irradiation. a) Contacted on the down left electrode at 450°C and in the dark. c) Under UV irradiation.

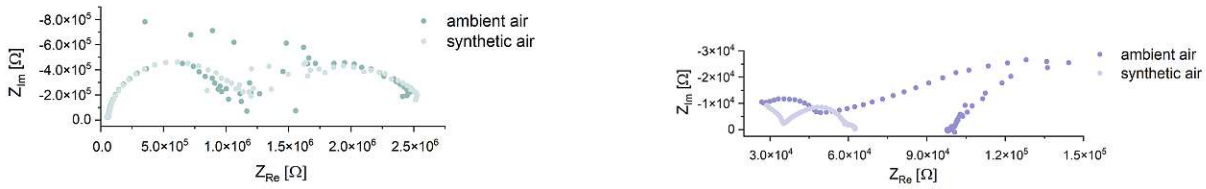

Figure 5.7: Temperature dependent impedance measurements of sample PK020 measured under ambient air conditions and synthetic air conditions. Left: At 300°C. Right: At 450°C.

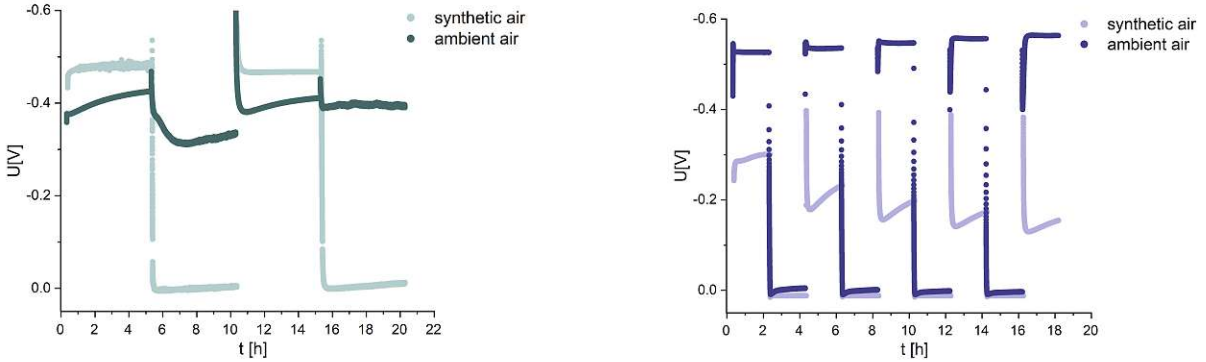

Figure 5.8: Temperature dependent voltage measurements of PK020 contacted on the up left electrode measured under ambient air and under synthetic air conditions. Left: At 300°C. Right: At 450°C.

Samples PK024 and PK025 were prepared with a STO 7% and a 15% target, and a thin film thickness of around 350 nm. The thickness was chosen in order to compare it with sample PK019, the behaviour of which was already described [22]. Due to the described Fermi levels (figure 2.7) of Sr deficient thin films (STO 0%, PK019 and PK020), the voltage measurements should show different results for the two samples prepared with overcompensated targets, as the Fermi level should shift towards the single crystal one. It is expected that the voltage build between the thin film and the single crystal would decline, as the Fermi level would be similar to the one of the single crystal. M. Morgenbesser [22] observed a similar behaviour for a Fe doped 7% Sr overcompensated target.

PK024 exhibits similar impedance spectra as the two thin film samples before, see figure 5.9. The high frequency feature, assigned to the STO bulk can be observed again as well as mid and low frequency features, which collapse under UV light irradiation. The mid and low frequency features are thus assigned to space charges.

The voltage measurements of PK024 depicted in figure 5.10 show similar results as sample PK019, reaching over -1.1 V. Again, a time dependent voltage can be observed. At 300°C the battery-like voltage doesn't reach zero after two hours, but is steadily decreasing. The peak voltage also seems to drop a bit over time. At 450°C, the battery voltage reaches zero.

Also the current measurements look almost the same as for sample PK019. At 300°C the current seems to self enhance itself again, reaching $-5.28 \cdot 10^{-6}$ A after 24 hours. At 450°C the current stays constant, reaching about $-8.98 \cdot 10^{-5}$ A after 24 hours. The measurement doesn't show the peak at the beginning of the measurement as PK019. The expected drop of photovoltage could not be observed. When looking at the LASIL measurements shown in figure 4.64, the reason can be found. Thin films deposited with the 7% overcompensated target also have a clear Sr deficiency, resulting in a presumed similar behaviour as the uncompensated target used for sample PK019. The difference to the measured sample of M. Morgenbesser, where 7% Sr excess lead to stoichiometric thin films, could be the Fe doping in the target, leading to a different deposition behaviour.

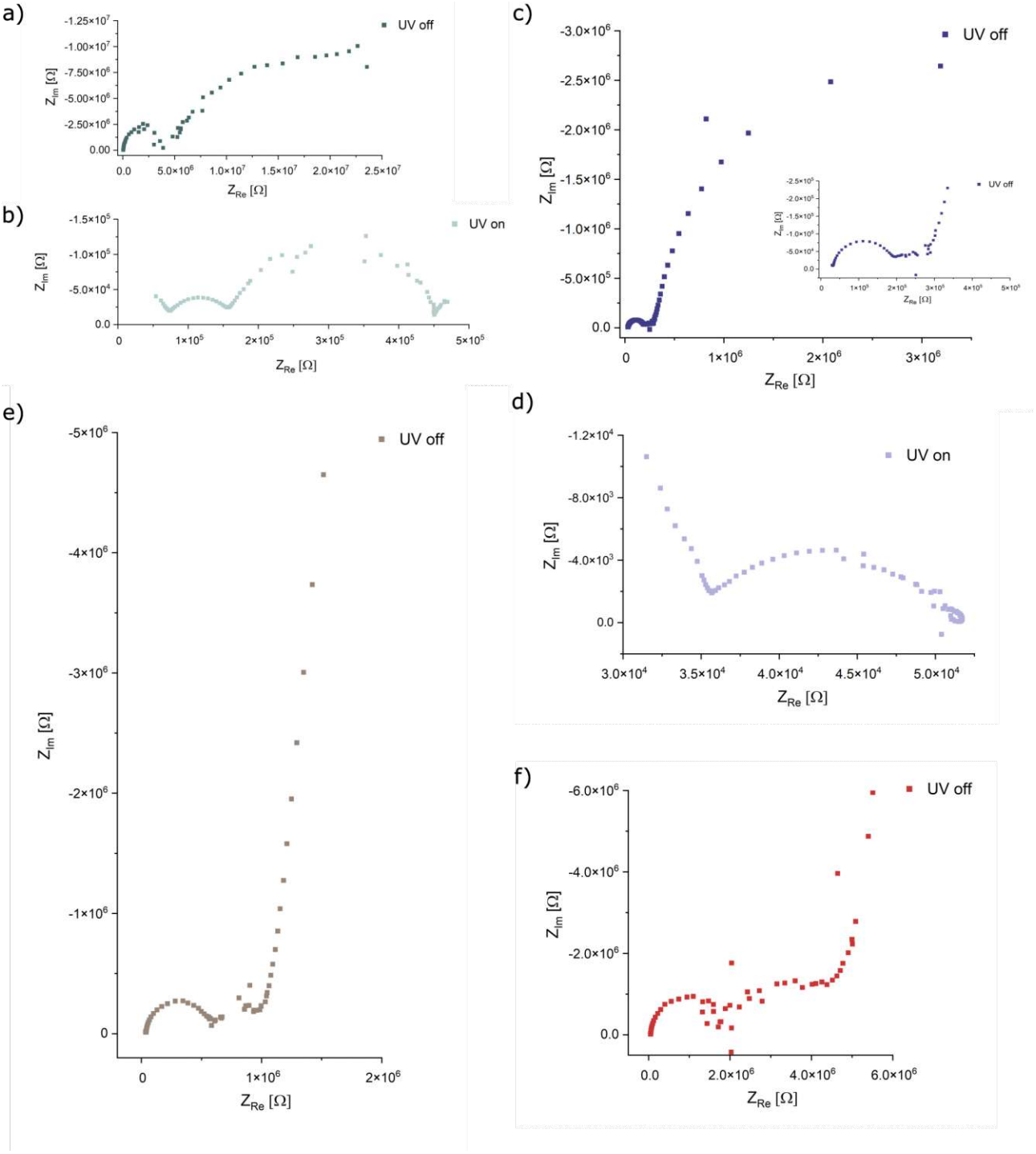

Figure 5.9: Impedance measurements of sample PK024 contacted on the left electrode. a) At 450°C in the dark and b) under UV irradiation. c) At 300°C in the dark and d) under UV irradiation. e) At 400°C. f) At 350°C.

PK025 also showed comparable impedance spectra, where a high and a mid to low frequency feature can be observed, depicted in figure 5.12. The high frequency feature is again assigned to the STO bulk. The mid to low frequency features, assigned to a space charge, have a smaller order of magnitude at 450°C (figure 5.12 b)), when compared to the other single crystal samples. When irradiated with UV light, no differences can be observed. The supposed space charge collapses. Interestingly, the voltage measurements yielded much smaller values as sample PK024. At 300°C, voltages of a bit over -300 mV were observed. At 450°C the voltage

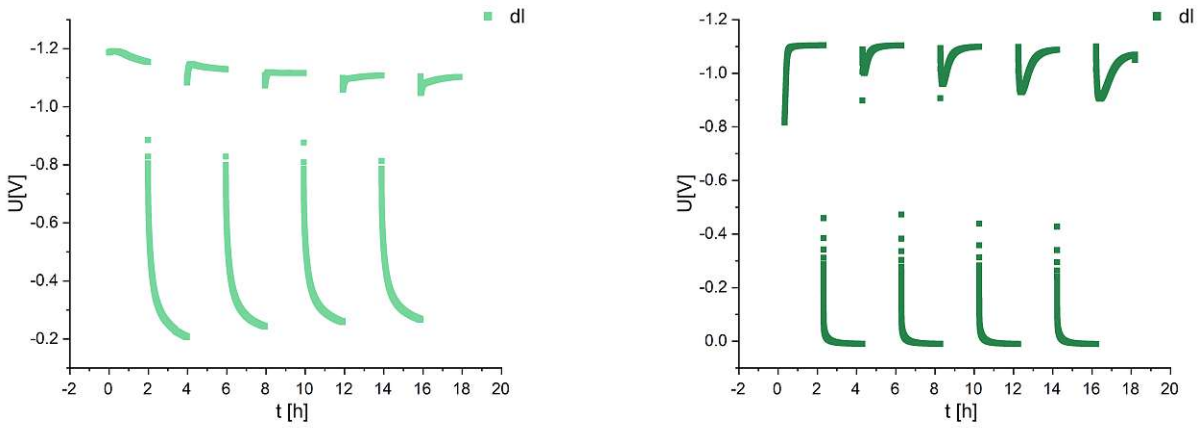

Figure 5.10: Temperature dependent voltage measurements of PK024 contacted on the left electrode. Left: At 300°C. Right: At 450°C.

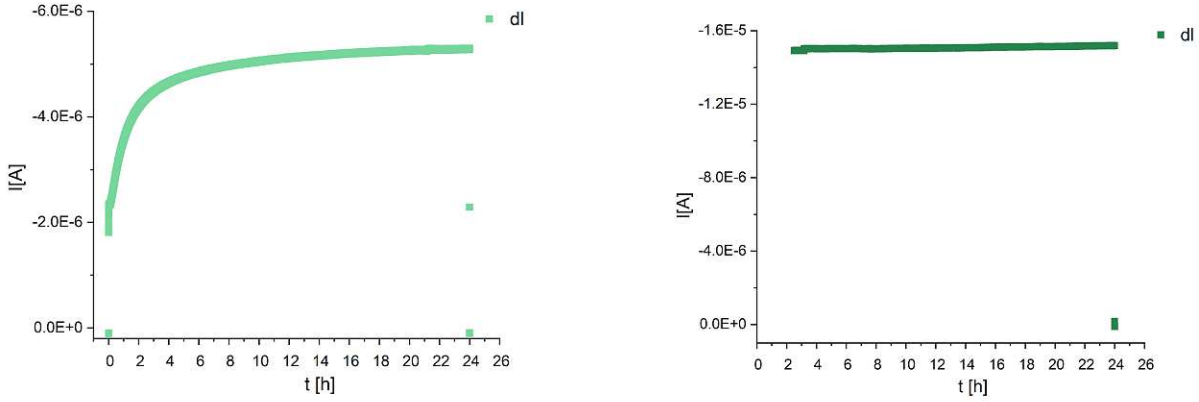

Figure 5.11: Temperature dependent current measurements of PK024 contacted on the left electrode. Left: At 300°C. Right: At 450°C.

dropped to around -150mV. The measurements are depicted in figure 5.13. This lowered voltage is rather surprising, as the LASIL measurements showed even less Sr in the 15% Sr excess target. Similar voltages as for PK024 would have been expected. Keeping the LASIL results apart, an explanation could be the movement of the Fermi level towards the Fermi level of the STO single crystal, due to enough Sr in the thin film, counteracting the Fermi level pinning. This would mean, that there are no more Ti atoms on the A-site leading to donor doping. When looking at figure 2.4 on the right, the resulting voltage would be smaller, if the STO thin Film fermi level would move between the one of LSCr and STO single crystal.
Notable is the observed voltage peak, occurring after the first and then following dark phases, when UV light is turned on again. This is hard to explain as no kind of battery voltage or alike can be observed. It may possibly come from stoichiometric or defect chemical changes in the STO bulk needing time to reach a equilibrium state when irradiated. When the UV light is turned off, the voltage drops to zero. The current measurement at 450°C looks almost the same as for sample PK019 but yields lower values. After 24 hours of UV light irradiation, $-2.88 \cdot 10^{-6}$ A were reached. The current seems to constantly decrease after a short peak at the beginning of the measurement.

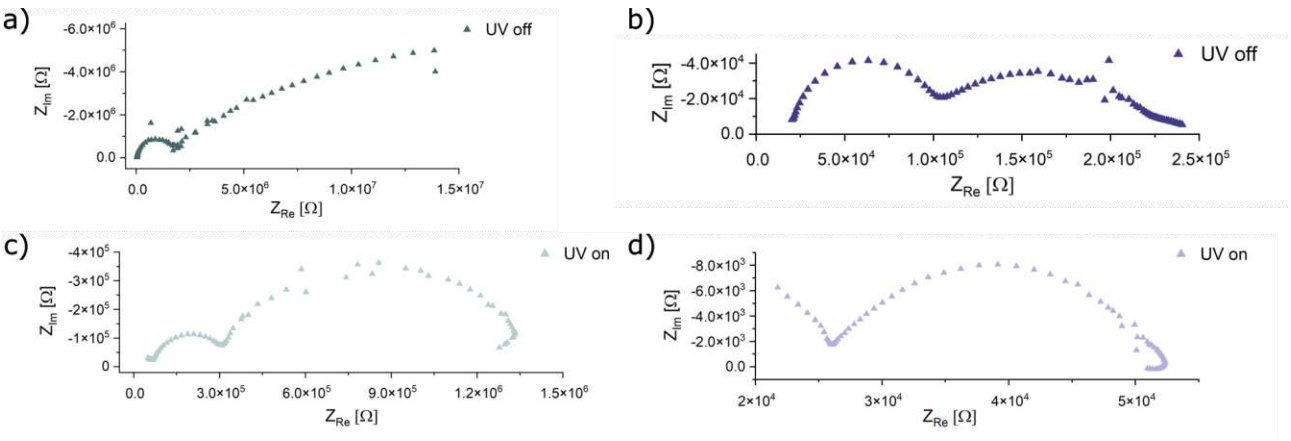

Figure 5.12: Impedance measurements of sample PK025. a) Contacted on the up right electrode at 300°C and in the dark. c) Under UV irradiation. a) Contacted on the up right electrode at 450°C and in the dark. c) Under UV irradiation.

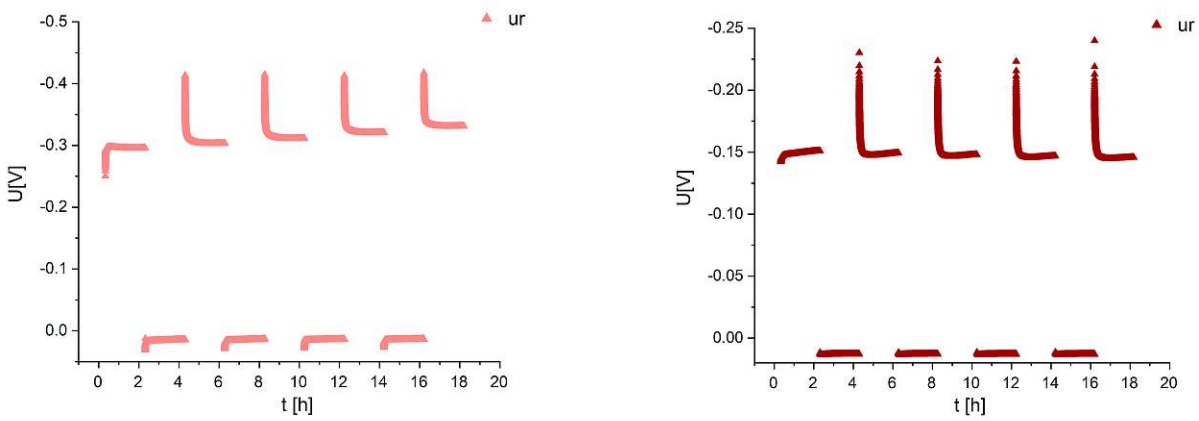

Figure 5.13: Temperature dependent voltage measurements of PK025 contacted on the up left electrode. Left: At 300°C. Right: At 450°C.

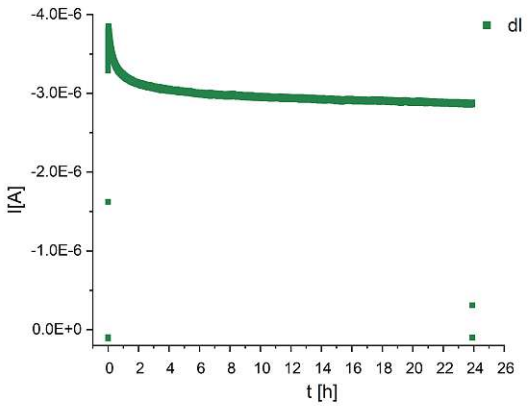

Figure 5.14: Current measurements of PK025 contacted on the up right electrode at 450°C.

6 Conclusion

Numerous samples with STO thin films as UV absorber were prepared using pulsed laser deposition and investigated with respect to the performance under UV illumination (photovoltaic mode). Several samples with high photovoltages could be prepared and tested. A number of sample and deposition parameters were varied in order to find optimised conditions. The results indicate that the reproducibility of samples is far from trivial and still an issue. The main outcomes of these studies are the following:

- STO thin film based high temperature solid oxide solar cells are feasible. Photovoltages up to -830 mV and short circuit photocurrents up to 0.19 mA/cm^2 were reached in ambient air at 300°C set temperature. Measurements under synthetic air showed similar results, reaching 870 mV and 0.25 mA/cm^2 at a set temperature of 300°C.
- The best results were reached with a STO thin film thickness of around 800 nm, deposited with a 7% Sr excess target and a fluence of 1 J/cm^2. Three out of ten samples prepared this way showed voltages over -500 mV, another three showed voltages over -100 mV. Furthermore, two samples prepared with different STO targets (10% Sr excess, stoichiometric) showed voltages over -200 mV.
- Impedance spectra sometimes showed a pronounced and clear low frequency feature. Almost always this feature decreased under UV light, indicating that this feature originates from a space charge region.
- The existence of the UV dependent low frequency arc corresponds with a substantial voltage generation.
- For samples with significant UV response, the photovoltage and current under UV light illumination shows constant behaviour for UV-on-off cycles. Some time-dependent behaviour at the start of UV irradiation is most probably because of equilibration processes inside the STO thin film due to oxygen incorporation during illumination.
- It is hypothesised that the STO thin film stoichiometry is one key factor, whether a sample yields a photovoltaic effect or not. When a STO thin film is Sr deficient, its conductivity gets pseudo-intrinsic. The consequence might be the absence of the space charge region and thus no possible voltage generation upon UV illumination. The parameter window in which thin films become stoichiometric seems to be very small.
- Many processes during the PLD process are still not fully controlled. The laser energy, for example, seems to vary over time, resulting in a varying fluence. This is especially detrimental for the fairly long deposition time needed for the STO thin film (∼70-90 min). Besides the appropriate laser fluence, the target composition seems to be an important factor of whether the thin film achieves the desired stoichiometry.
- SEM measurements revealed different surfaces of photovoltaically-active and photovoltaically-inactive samples. These results underline the differences during preparation. The observed triangular features are differently orientated STO crystals. TEM cross-sections further revealed different micro-structures for the STO thin films. The thin film growth seems to vary between a homogeneous dense growth and a differently orientated island growth (triangular and square features). When such island growth appears, probably no space charge zone is formed or space charges of the grains interfere with each other. In such thin films, the LSCr/STO thin film junction does not result in a measurable voltage.
- The LASIL measurements revealed Sr deficient thin films even from Sr overcompensated STO targets. This has to be further investigated, as the deposition process most likely changed over the course of the work.

Accordingly, STO thin film based solar cell samples can be prepared but the reproducibility of the preparation process has still to be improved. The micro-structure of the thin films seems to be a key factor of whether samples show a photo-response or not. However, even if a dense micro-structure is achieved, the stoichiometry has to fit.

Finally, single crystal based solar cells were successfully prepared. Results from Morgenbesser et al. [33] were reproduced for a sample with a STO single crystal as substrate, a 300 nm STO thin film deposited with a stoichiometric target and a LSCr top electrode. Voltages of over -1 V were observed. The voltage is assumed to originate between the STO thin film/STO bulk junction due to the Sr deficient STO thin film and the resulting pinned Fermi level. The high-frequency feature of the impedance spectra was assigned to the STO bulk and the low frequency features are caused by space charges, as they collapse under UV light irradiation. Furthermore, a battery voltage was observed, which is due to oxygen vacancy stoichiometry changes in the STO bulk.

Danksagung

Nach dem doch ein oder anderen Jahr neigt sich die Studienzeit nun langsam aber sicher dem Ende zu. Rückblickend ist sehr viel passiert, und auch wenn sicherlich nicht alles hängen geblieben ist, lernt man während des Studiums meiner Meinung nach viel mehr als nur sein Fach. Viele Menschen haben diesen Abschnitt erst so lässig gemacht wie er war, da kann man guten Gewissens auch mal Danke sagen.

Vorn weg danke an das gesamte Institut. Eine Anhäufung von so vielen hilfsbereiten und freundlichen Menschen findet man heutzutage nicht mehr oft. Insbesondere möchte ich Prof. Fleig bzw. Jürgen danken, der mir diese Arbeit ermöglicht und mit seiner Freude an der Wissenschaft immer für einen Motivationsschub gesorgt hat. Auch bei Steffi will ich mich bedanken, die mich durch diese Arbeit begleitet und mich auch in jeder Hinsicht unterstützt hat. Außerdem möchte ich mich noch bei Martin, Christin, Alex und Claudia bedanken, von denen ich ohne ein Wimpernzucken quasi immer Hilfe bekommen habe, sei es mit der geliebten PLD oder mit anderen tollen Themen. Auch danke an alle am Institut für die lustigen Gespräche, die den Forschungsalltag angenehmer und lockerer gemacht haben. Ein bisserl ein Spaß muss schon immer sein.

Die Liste an Freunden, die mir den Alltag über die Jahre außerdem versüßt haben, ist lang. Um das ganze zusammenzufassen, danke ich der erweiterten Physik-Runde, Kletter-Runde, Kärntner-Runde und allen anderen beteiligten Personen für extrem lustige Reisen, Abende und andere Aktivitäten. Insbesondere möchte ich mich bei Felix, Felix und Joschi bedanken, mit denen ich wohl mit unter am meisten Zeit verbracht habe und mit denen ich über alles reden konnte. Auch dir, Franzi, möchte ich danken, dass du für mich immer da warst, mich in jeder Lage unterstützt und es immer schaffst mir ein Lächeln aufs Gesicht zu drücken.
Thx an alle für den geilen Support und Spaß über die Jahre :*.

Zu guter Letzt möchte ich meiner Familie danken, insbesondere meinen Eltern Michael und Gigi! Danke, dass ihr mich bei allem unterstützt, vertraut und mir ein sorgloses Studentenleben ermöglicht habt. Ich weiß, das ist nicht selbstverständlich und es bedeutet mir unglaublich viel! Auch dir Paul möchte ich danken, dass du mich immer eingebunden und unterstützt hast und einfach der beste Bruder bist.

List of Figures

List of Tables

References

[1] Ehsanul Kabir, Pawan Kumar, Sandeep Kumar, Adedeji A. Adelodun, and Ki-Hyun Kim. "Solar energy: Potential and future prospects". In: *Renewable and Sustainable Energy Reviews* 82 (2018), pp. 894–900. DOI: https://doi.org/10.1016/j.rser.2017.09.094.

[2] Thomas Blaschke, Markus Biberacher, Sabine Gadocha, and Ingrid Schardinger. "Energy landscapes: Meeting energy demands and human aspirations". In: *Biomass and Bioenergy* 55 (2013), pp. 3–16. DOI: https://doi.org/10.1016/j.biombioe.2012.11.022.

[3] "World Energy Outlook 2022". In: *International Energy Agency* (2022). Accessed: 2023-01-30. URL: https://www.iea.org/reports/world-energy-outlook-2022.

[4] "Global Energy Perspetive 2022". In: *McKinsey Energy Insights Global Energy Perspective 2022* (). Accessed: 2023-01-30. URL: www.mckinsey.com.

[5] Karen Rose, Scott Eldridge, and Lyman Chapin. "The internet of things: An overview". In: *The internet society (ISOC)* 80 (2015), pp. 1–50.

[6] Joseph J. Wysocki and Paul Rappaport. "Effect of Temperature on Photovoltaic Solar Energy Conversion". In: *Journal of Applied Physics* 31.3 (1960), pp. 571–578. DOI: 10.1063/1.1735630.

[7] Sven Rühle, Assaf Y. Anderson, Hannah-Noa Barad, Benjamin Kupfer, Yaniv Bouhadana, Eli Rosh-Hodesh, and Arie Zaban. "All-Oxide Photovoltaics". In: *The Journal of Physical Chemistry Letters* 3.24 (2012), pp. 3755–3764. DOI: 10.1021/jz3017039.

[8] "Energy HarveStorers for Powering the Internet of Things". In: *Horizon 2020* (2018). DOI: 10.3030/824072. URL: https://cordis.europa.eu/project/id/824072.

[9] Alexander Schmid, Martin Krammer, and Jürgen Fleig. "Rechargeable Oxide Ion Batteries Based on Mixed Conducting Oxide Electrodes". In: *Advanced Energy Materials* (2023), p. 2203789. DOI: https://doi.org/10.1002/aenm.202203789.

[10] Georg Christoph Brunauer, Bernhard Rotter, Gregor Walch, Esmaeil Esmaeili, Alexander Karl Opitz, Karl Ponweiser, Johann Summhammer, and Juergen Fleig. "UV-Light-Driven Oxygen Pumping in a High-Temperature Solid Oxide Photoelectrochemical Cell". In: *Advanced functional materials* 26.1 (2016), pp. 120–128.

[11] Roger A. De Souza, Jürgen Fleig, Rotraut Merkle, and Joachim Maier. "SrTiO3: a model electroceramic". In: *International journal of materials research* 94.3 (2022), pp. 218–225.

[12] R. A. Cowley. "The Phase Transition of Strontium Titanate". In: *Philosophical Transactions: Mathematical, Physical and Engineering Sciences* 354.1720 (1996), pp. 2799–2814.

[13] Matthäus Siebenhofer, Alexander Viernstein, Maximilian Morgenbesser, Jürgen Fleig, and Markus Kubicek. "Photoinduced electronic and ionic effects in strontium titanate". In: *Mater. Adv.* 2 (2021), pp. 7583–7619. DOI: 10.1039/D1MA00906K.

[14] L. Enzlberger. "Photovoltaic properties of SrTiO3-δ in single crystalline and thin film cells". In: (2022).

[15] "Intrinsic Point Defects in Stoichiometric Compounds". In: *Defects in Solids*. John Wiley & Sons, Ltd, 2008. Chap. 2, pp. 45–82. DOI: https://doi.org/10.1002/9780470380758.ch2.

[16] Zainab Raheem. *Kittel, Charles - Introduction To Solid State Physics 8Th Ed.* Mar. 2019.

[17] Jürgen Fleig. "Microelectrodes in Solid State Ionics". In: *Advances in Electrochemical Science and Engineering*. John Wiley & Sons, Ltd, 2002. Chap. 1, pp. 1–87. DOI: https://doi.org/10.1002/3527600787.ch1.

[18] Matthäus Siebenhofer, Federico Baiutti, Juan de Dios Sirvent, Tobias M. Huber, Alexander Viernstein, Stefan Smetaczek, Christopher Herzig, Maciej Oskar Liedke, Maik Butterling, Andreas Wagner, Eric Hirschmann, Andreas Limbeck, Albert Tarancon, Jürgen Fleig, and Markus Kubicek. "Exploring point defects and trap states in undoped SrTiO3 single crystals". In: *Journal of the European Ceramic Society* 42.4 (2022), pp. 1510–1521. DOI: https://doi.org/10.1016/j.jeurceramsoc.2021.10.010.

[19] Maximilian Morgenbesser, Stefanie Taibl, Markus Kubicek, Alexander Schmid, Alexander Viernstein, Niklas Bodenmüller, Christopher Herzig, Federico Baiutti, Juan de Dios Sirvent, Maciej Oskar Liedke, Maik Butterling, Andreas Wagner, Werner Artner, Andreas Limbeck, Albert Tarancon, and Jürgen Fleig. "Cation non-stoichiometry in Fe:SrTiO3 thin films and its effect on the electrical conductivity". In: *Nanoscale Adv.* 3 (2021), pp. 6114–6127. DOI: 10.1039/D1NA00358E.

[20] Maximilian Morgenbesser, Alexander Viernstein, Alexander Schmid, Christopher Herzig, Markus Kubicek, Stefanie Taibl, Gesara Bimashofer, Jochen Stahn, Carlos Antonio Fernandes Vaz, Max Döbeli, Federico Biautti, Juan de Dios Sirvent, Maciej Oskar Liedke, Maik Butterling, Michał Kamiński, Martin Tolkiehn, Vedran Vonk, Andreas Stierle, Andreas Wagner, Albert Tarancon, Andreas Limbeck, and Jürgen Fleig. "Unravelling the Origin of Ultra-Low Conductivity in SrTiO3 Thin Films: Sr Vacancies and Ti on A-Sites Cause Fermi Level Pinning". In: *Advanced functional materials* 32.38 (2022), n/a.

[21] U. N. Gries, M. Kessel, F. V. E. Hensling, R. Dittmann, M. Martin, and R. A. De Souza. "Behavior of cation vacancies in single-crystal and in thin-film $SrTiO_3$: The importance of strontium vacancies and their defect associates". In: *Phys. Rev. Mater.* 4 (Dec. 2020), p. 123404. DOI: 10.1103/PhysRevMaterials.4.123404.

[22] Maximilian Morgenbesser. *Nonstoichiometry in SrTiO3 and its relevance for tunable conductivity and photovoltage*. 2021.

[23] Christian Ohly, Susanne Hoffmann, Krzysztof Szot, and Rainer Waser. "High temperature conductivity behavior of doped SrTiO3 thin films". In: *Integrated Ferroelectrics* 33.1-4 (2001), pp. 363–372. DOI: 10.1080/10584580108222318.

[24] Christian Ohly, Susanne Hoffmann-Eifert, Xin Guo, Jürgen Schubert, and Rainer Waser. "Electrical Conductivity of Epitaxial SrTiO3 Thin Films as a Function of Oxygen Partial Pressure and Temperature". In: *Journal of the American Ceramic Society* 89.9 (2006), pp. 2845–2852. DOI: https://doi.org/10.1111/j.1551-2916.2006.01178.x.

[25] Minseok Choi, Fumiyasu Oba, and Isao Tanaka. "Role of Ti antisitelike defects in SrTiO3". In: *Physical review letters* 103.18 (2009), pp. 185502–185502.

[26] Antti Karjalainen, Vera Prozheeva, Ilja Makkonen, Christo Guguschev, Toni Markurt, Matthias Bickermann, and Filip Tuomisto. "TiSr antisite: An abundant point defect in SrTiO3". In: *Journal of applied physics* 127.24 (2020).

[27] Bin Liu, Valentino R. Cooper, Haixuan Xu, Haiyan Xiao, Yanwen Zhang, and William J. Weber. "Composition dependent intrinsic defect structures in SrTiO3". In: *Physical chemistry chemical physics : PCCP* 16.29 (2014), pp. 15590–15596.

[28] Konstantin Klyukin and Vitaly Alexandrov. "Effect of intrinsic point defects on ferroelectric polarization behavior of SrTiO 3". eng. In: *Physical review. B* 95.3 (2017).

[29] Ingrid Denk, Wolfram Münch, and Joachim Maier. "Partial Conductivities in SrTiO3: Bulk Polarization Experiments, Oxygen Concentration Cell Measurements, and Defect-Chemical Modeling". In: *Journal of the American Ceramic Society* 78.12 (1995), pp. 3265–3272.

[30] K. Van Benthem, C. Elsässer, and R.H. French. "Bulk electronic structure of SrTiO3: Experiment and theory". In: *Journal of applied physics* 90.12 (2001), pp. 6156–6164.

[31] Gregor Walch, Bernhard Rotter, Georg Christoph Brunauer, Esmaeil Esmaeili, Alexander Karl Opitz, Markus Kubicek, Johann Summhammer, Karl Ponweiser, and Jürgen Fleig. "A solid oxide photoelectrochemical cell with UV light-driven oxygen storage in mixed conducting electrodes". In: *Journal of materials chemistry. A, Materials for energy and sustainability* 5.4 (2017), pp. 1637–1649.

[32] Rotraut Merkle, Roger A. De Souza, and Joachim Maier. "Optically Tuning the Rate of Stoichiometry Changes: Surface-Controlled Oxygen Incorporation into Oxides under UV Irradiation". In: *Angewandte Chemie (International ed.)* 40.11 (2001), pp. 2126–2129.

[33] Maximilian Morgenbesser, Alexander Schmid, Alexander Viernstein, Juan de Dios Sirvent, Francesco Chiabrera, Niklas Bodenmüller, Stefanie Taibl, Markus Kubicek, Federico Baiutti, Albert Tarancon, and Jürgen Fleig. "SrTiO3 based high temperature solid oxide solar cells: Photovoltages, photocurrents and mechanistic insight". In: *Solid state ionics* 368 (2021), p. 115700.

[34] Alexander Viernstein, Markus Kubicek, Maximilian Morgenbesser, Tobias M. Huber, Emil Ellmeyer, Matthäus Siebenhofer, Carlos A.F. Vaz, and Jürgen Fleig. "Mechanism of photo-ionic stoichiometry changes in SrTiO3". In: *Solid State Ionics* 383 (2022), p. 115992. DOI: https://doi.org/10.1016/j.ssi.2022.115992.

[35] Stephan Rodewald, Natsuko Sakai, Katsuhiko Yamaji, H. Yokokawa, Juergen Fleig, and Joachim Maier. "The Effect of the Oxygen Exchange at Electrodes on the High-Voltage Electrocoloration of Fe-Doped SrTiO3 Single Crystals: A Combined SIMS and Microelectrode Impedance Study". In: *Journal of Electroceramics* 7 (2001), pp. 95–105.

[36] Rainer Waser, Tudor Baiatu, and Karl-Heinz Härdtl. "dc Electrical Degradation of Perovskite-Type Titanates: I, Ceramics". In: *Journal of the American Ceramic Society* 73.6 (1990), pp. 1645–1653. DOI: https://doi.org/10.1111/j.1151-2916.1990.tb09809.x.

[37] T. Ohnishi, H. Koinuma, and M. Lippmaa. "Pulsed laser deposition of oxide thin films". In: *Applied Surface Science* 252.7 (2006). Proceedings of the Third Japan-US Workshop on Combinatorial Material Science and Technology, pp. 2466–2471. DOI: https://doi.org/10.1016/j.apsusc.2005.04.057.

[38] B. Dam, J. H. Rector, J. Johansson, J. Huijbregtse, and D. G. De Groot. "Mechanism of incongruent ablation of SrTiO3". In: *Journal of Applied Physics* 83.6 (1998), pp. 3386–3389. DOI: 10.1063/1.367106.

[39] B. Dam, J.H. Rector, J. Johansson, S. Kars, and R. Griessen. "Stoichiometric transfer of complex oxides by pulsed laser deposition". In: *Applied Surface Science* 96-98 (1996), pp. 679–684. DOI: https://doi.org/10.1016/0169-4332(95)00543-9.

[40] Tsuyoshi Ohnishi, Keisuke Shibuya, Takahisa Yamamoto, and Mikk Lippmaa. "Defects and transport in complex oxide thin films". In: *Journal of Applied Physics* 103.10 (2008), p. 103703. DOI: 10.1063/1.2921972.

[41] Donald M. Mattox. "Chapter 1 - Introduction". In: *Handbook of Physical Vapor Deposition (PVD) Processing (Second Edition)*. Ed. by Donald M. Mattox. Second Edition. William Andrew Publishing, 2010, pp. 1–24. DOI: https://doi.org/10.1016/B978-0-8155-2037-5.00001-0.

[42] Robert Eason. *Pulsed laser deposition of thin films : applications-led growth of functional materials*. 2007.

[43] T. Ohnishi, M. Lippmaa, T. Yamamoto, S. Meguro, and H. Koinuma. "Improved stoichiometry and misfit control in perovskite thin film formation at a critical fluence by pulsed laser deposition". In: *Applied Physics Letters* 87.24 (2005), p. 241919. DOI: 10.1063/1.2146069.

[44] Stefan Gerhold, Michele Riva, Bilge Yildiz, Michael Schmid, and Ulrike Diebold. "Adjusting island density and morphology of the SrTiO3(110)-(4×1) surface: Pulsed laser deposition combined with scanning tunneling microscopy". In: *Surface Science* 651 (2016), pp. 76–83. DOI: https://doi.org/10.1016/j.susc.2016.03.010.

[45] Mark E Orazem and Bernard Tribollet. *Electrochemical impedance spectroscopy*. Electrochemical Society series. Wiley, 2008.

[46] R. Srinivasan and F. Fasmin. *An Introduction to Electrochemical Impedance Spectroscopy (1st ed.)* CRC Press, May 2021. DOI: https://doi.org/10.1201/9781003127932.

[47] Günter Sauerbrey. "Verwendung von Schwingquarzen zur Wägung dünner Schichten und zur Mikrowägung". In: *Zeitschrift für Physik* 155 (1959), pp. 206–222. DOI: https://doi.org/10.1007/BF01337937.

[48] T.M. Huber, A.K. Opitz, M. Kubicek, H. Hutter, and J. Fleig. "Temperature gradients in microelectrode measurements: Relevance and solutions for studies of SOFC electrode materials". In: *Solid State Ionics* 268 (2014), pp. 82–93. ISSN: 0167-2738. DOI: https://doi.org/10.1016/j.ssi.2014.10.002.

[49] Ernst Ruska-Centre for Microscopy and Spectroscopy with Electrons (ER-C) et al. "FEI Helios NanoLab 460F1 FIB-SEM". In: *Journal of large-scale research facilities* 2.A59 (2016). DOI: http://dx.doi.org/10.17815/jlsrf-2-105.

[50] Ernst Ruska-Centre for Microscopy and Spectroscopy with Electrons. "FEI Tecnai G2 F20". In: *Journal of large-scale research facilities* 2.A77 (2016). DOI: http://dx.doi.org/10.17815/jlsrf-2-138.

[51] Roger A. De Souza, Jürgen Fleig, Joachim Maier, Oliver Kienzle, Zaoli Zhang, Wilfried Sigle, and Manfred Rühle. "Electrical and Structural Characterization of a Low-Angle Tilt Grain Boundary in Iron-Doped Strontium Titanate". In: *Journal of the American Ceramic Society* 86.6 (2003), pp. 922–928. DOI: https://doi.org/10.1111/j.1151-2916.2003.tb03398.x.

[52] J Fleig, S Rodewald, and J Maier. "Microcontact impedance measurements of individual highly resistive grain boundaries: general aspects and application to acceptor-doped SrTiO 3". In: *Journal of Applied Physics* 87.5 (2000), pp. 2372–2381.

[53] Matthäus Siebenhofer, Tobias Huber, Werner Artner, Jürgen Fleig, and Markus Kubicek. "Substrate stoichiometry changes during pulsed laser deposition: a case study on SrTiO3". In: *Acta Materialia* 203 (2021), p. 116461. DOI: https://doi.org/10.1016/j.actamat.2020.10.077.

[54] J. Fleig. "The grain boundary impedance of random microstructures: numerical simulations and implications for the analysis of experimental data". In: *Solid State Ionics* 150.1 (2002), pp. 181–193. DOI: https://doi.org/10.1016/S0167-2738(02)00274-6.

[55] Giuliano Gregori, Piero Lupetin, and Joachim Maier. "Huge Electrical Conductivity Changes in SrTiO3 upon Reduction of the Grain Size to the Nanoscale". In: *Ecs Transactions* 45.1 (2012), p. 19.